

Novel bifunctional double-layer catalysts for application in microreactors for direct DME synthesis

Zur Erlangung des akademischen Grades eines
Doktors der Ingenieurwissenschaften
(Dr.-Ing.)

der Fakultät für Chemieingenieurwesen und Verfahrenstechnik des
Karlsruher Instituts für Technologie (KIT)

genehmigte
DISSERTATION

von

M.Sc. Seungcheol Lee

aus Südkorea

Referent: Prof. Dr.-Ing. Roland Dittmeyer
Korreferent: Prof. Dr.-Ing. Jörg Sauer
Tag der mündlichen Prüfung: 25. 01. 2016



This document is licensed under the Creative Commons Attribution – Share Alike 3.0 DE License (CC BY-SA 3.0 DE): <http://creativecommons.org/licenses/by-sa/3.0/de/>

The LORD thy God in the midst of thee is mighty; he will save, he will rejoice over thee with joy; he will rest in his love, he will joy over thee with singing.

Zephaniah 3:17

Abstract

This thesis describes experimental research toward the selective and efficient DME production from syngas in microstructured reactors using bifunctional catalysts. Two catalysts, Cu/ZnO/Al₂O₃ and ZSM-5, catalyze syngas conversion to methanol and methanol conversion to DME, respectively. In direct DME synthesis, two reactions are taking place in one reactor with a bifunctional catalyst, a proper combination of methanol synthesis and methanol dehydration catalysts. This process is highly exothermic so that microstructured reactors having high heat and mass transport rates can be suggested. Therefore, preparation of bifunctional catalysts and their introduction into microstructured reactors were investigated.

Flame spray pyrolysis (FSP) for Cu/ZnO/Al₂O₃ catalyst synthesis was developed. It can reduce the synthesis time of the catalyst as it is a relatively simple method. Beyond using common organometallic precursors, was proven the effectiveness of metal nitrate precursors in Cu/ZnO/Al₂O₃ synthesis. The catalytic properties of the produced catalysts were investigated for direct DME synthesis. The reaction results showed higher activity with the Cu/ZnO/Al₂O₃ synthesized from metal nitrate precursors than with the Cu/ZnO/Al₂O₃ synthesized from organometallic precursors.

In order to introduce catalysts efficiently in microstructured reactors, inkjet printing technology was proposed. Catalyst particles were controlled in size, and catalyst inks were formulated by adjusting rheological parameters with the aid of various additives. The parameters for a drop-on-demand inkjet printer were thoroughly investigated for catalyst-containing inks. The optimized inkjet printing was applied for formation of a bifunctional double-layer catalyst coating in a microchannel reactor. For this, Cu/ZnO/Al₂O₃ (bottom layer) and ZSM-5 (top layer) were printed sequentially into the microchannels. The idea is that syngas diffuses to the bottom layer from above the top layer, and then the produced methanol diffuses out through the top layer. During this out-diffusion

the methanol is converted to DME. Under the conditions of the direct DME synthesis reaction over the double-layer catalyst, a lot of hydrocarbon side products were observed instead of DME. Several experimental efforts have been done to understand the reactions taking place in the double-layer catalyst in the microchannel reactor. Correlations of hydrocarbon formation with circumstances at the catalyst surface have been worked out. Therefore, this research provides understanding of reaction processes in the double-layer catalyst as well as the possibility for further application of it in other sequential reactions.

Kurzfassung

In dieser Dissertation werden wissenschaftliche Experimente zur selektiven und effizienten DME Direktsynthese aus Synthesegas an bi-funktionellen Katalysatoren in mikrostrukturierten Reaktoren beschrieben. Zwei Katalysatorsysteme, Cu/ZnO/Al₂O₃ und ZSM-5, setzen Synthesegas katalytisch in Methanol, beziehungsweise Methanol wiederum in DME um. Bei der DME-Direktsynthese finden die Reaktionsschritte der Methanolsynthese und Methanol-Dehydratisierung an einem bi-funktionellen Katalysator in einem Reaktor statt. Diese Reaktion ist hochgradig exotherm, sodass mikrostrukturierte Reaktoren mit hohen Wärme- und Stofftransportraten für den Einsatz in Frage kommen. Aus diesem Grund wurden in dieser Arbeit die Herstellung von bi-funktionellen Katalysatoren und deren Verwendung in mikrostrukturierten Reaktoren untersucht.

Für die Herstellung des Cu/ZnO/Al₂O₃ Katalysators wurde eine Methode der Flammensprühpyrolyse entwickelt. Mit dieser relativ einfachen Methode kann die Präparationszeit der Katalysatoren deutlich verringert werden. Zusätzlich zu herkömmlichen metallorganischen Verbindungen für die Herstellung der Cu/ZnO/Al₂O₃ Komponente wurde der mögliche Einsatz von Metallnitrat-Präkursoren untersucht. Die katalytischen Eigenschaften der neuartigen Katalysatoren bezüglich DME-Direktsynthese wurden experimentell untersucht. Die Cu/ZnO/Al₂O₃ Katalysatoren hergestellt aus Metallnitrat-Präkursoren wiesen eine höhere Aktivität auf als mittels metallorganischen Verbindungen hergestellte Cu/ZnO/Al₂O₃ Katalysatoren.

Im Zuge der Applizierung der Katalysatoren in mikrostrukturierte Reaktoren wurde ein Tintenstrahldruckverfahren entwickelt, welches den Katalysator gezielt und effektiv in die Mikrokanäle einbringt. Dafür wurde die Partikelgröße der Katalysatoren eingestellt und über die Einstellung von rheologischen Parametern durch Zugabe verschiedener Additive wurde eine druckbare Katalysatortinte formuliert. Die Betriebseinstellungen für einen

Drop-on-Demand Drucker wurden sorgfältig für diese Katalysator-tinten ermittelt. Dieses Tintenstrahl-druckverfahren wurde anschließend für die Herstellung von bi-funktionellen Katalysatorschichten, sogenannten Doppelschichten, verwendet. In die Mikrokanäle wurde zuerst als untere Schicht der Katalysator für die Methanolsynthese (Cu/ZnO/Al₂O₃) gedruckt. Anschließend wurde auf die untere Schicht die Dehydatisierungskomponente (ZSM-5) als obere Schicht gedruckt. Die prinzipielle Idee für dieses System ist, dass Synthesegas zunächst durch die obere Katalysatorschicht diffundiert und an der unteren Schicht zu Methanol umgesetzt wird. Das erzeugte Methanol diffundiert anschließend durch die obere Schicht und wird zu DME umgesetzt.

Bei der experimentellen Durchführung der DME-Direktsynthese mit den Doppelschichten wurde eine große Menge an Nebenprodukten auf Kohlenwasserstoffbasis beobachtet. Eine Vielzahl an Experimenten wurde durchgeführt, um die kinetischen Mechanismen für diese Nebenproduktbildung an den Doppelschichten im Mikrostrukturreaktor zu verstehen. Korrelationen zwischen der Nebenproduktbildung und den verschiedenen Reaktionsbedingungen an der Katalysatoroberfläche wurden aufgestellt. Daher liefert diese Arbeit Ansätze zum Verständnis von Reaktionsvorgängen in katalytisch aktiven Doppelschichten sowie die Möglichkeit des Einsatzes solcher Reaktionssysteme für weitere industriell relevante Folgereaktionen.

Contents

| | |
|--|------------|
| Abstract | i |
| Kurzfassung | iii |
| 1. Introduction | 1 |
| 1.1. Motivation | 1 |
| 1.2. Benefits and application of DME | 4 |
| 1.3. Production of DME | 6 |
| 1.3.1. Production of syngas | 6 |
| 1.3.2. Two-stage process for DME production | 10 |
| 1.3.3. One-stage process (direct DME synthesis) | 12 |
| 1.4. Reactions and catalysts for DME synthesis | 14 |
| 1.4.1. Methanol synthesis reaction and catalysts | 14 |
| 1.4.2. Methanol dehydration reaction and catalysts | 17 |
| 1.4.3. Bifunctional catalysts for the one-stage process | 19 |
| 1.5. Microstructured reactors | 22 |
| 1.5.1. Advantages of microstructured reactors | 22 |
| 1.5.2. Introduction of catalysts in microstructured reactors | 23 |
| 1.5.3. Application to DME synthesis | 26 |
| 1.6. Contribution of the thesis | 28 |
| 1.7. Outline of the thesis | 28 |
| 2. Materials and methods | 31 |
| 2.1. Catalyst preparation | 31 |
| 2.1.1. CZA synthesis via FSP | 31 |
| 2.1.2. ZSM-5 preparation | 33 |
| 2.2. Characterization | 34 |
| 2.3. Reactors | 35 |
| 2.3.1. Tubular reactor | 35 |
| 2.3.2. Bery-type reactor | 36 |

| | | |
|-----------|--|-----------|
| 2.3.3. | Microchannel reactor | 37 |
| 2.4. | Catalyst coating in microchannels | 40 |
| 2.4.1. | Inkjet printing | 40 |
| 2.4.2. | Catalyst coating with micropipette | 42 |
| 2.4.3. | Double-layer catalyst coating for direct DME synthesis . . . | 42 |
| 2.5. | Reaction experiments and analysis | 43 |
| 2.5.1. | Test rig design | 43 |
| 2.5.2. | Gas analysis by gas chromatography (GC) | 45 |
| 2.5.3. | Catalyst activation | 46 |
| 2.5.4. | Reaction performance | 47 |
| 3. | Investigation of Cu/ZnO/Al₂O₃ (CZA) via flame spray pyrolysis (FSP) | 49 |
| 3.1. | Flame technique for catalyst production | 49 |
| 3.2. | FSP synthesis of Cu/ZnO/Al ₂ O ₃ | 52 |
| 3.2.1. | State-of-the-art of FSP-CZA | 52 |
| 3.2.2. | Characterization of FSP-CZA | 53 |
| 3.2.3. | Catalytic activity of FSP-CZA for direct DME synthesis . . . | 59 |
| 4. | Inkjet printing for catalyst coating into microchannels | 67 |
| 4.1. | Introduction of inkjet printing | 67 |
| 4.1.1. | Principle and application of inkjet printing technology . . . | 67 |
| 4.1.2. | Particle printing | 71 |
| 4.1.3. | Heterogeneous catalyst ink | 73 |
| 4.1.4. | Inkjet printing in microstructured plates | 74 |
| 4.2. | Investigation of the printer operating parameters | 75 |
| 4.2.1. | Drop generation and printing parameter investigation . . . | 77 |
| 4.2.2. | Drying and coffee ring formation | 80 |
| 4.3. | Investigation of printing in microchannels | 82 |
| 4.3.1. | Printing of catalyst inks into etched semicircular microchannels | 82 |
| 4.3.2. | Deposition of catalyst support layers into milled rectangular microchannels | 84 |
| 4.3.3. | Zeolite printing in microchannels | 89 |
| 5. | Direct DME synthesis over double-layer catalysts in microchannel reactors | 93 |
| 5.1. | Bifunctional double-layer catalyst coating | 93 |
| 5.1.1. | Ink formulation | 93 |

| | |
|---|------------|
| 5.1.2. Double-layer printing | 106 |
| 5.2. Direct DME synthesis in microchannel reactors | 110 |
| 5.2.1. Activity of the double-layer catalyst | 110 |
| 5.2.2. Investigation of hydrocarbon formation in the double-layer catalyst | 112 |
| 6. Conclusion and outlook | 123 |
| References | 127 |
| List of acronyms | 149 |
| List of symbols | 150 |
| List of subscripts | 151 |
| | |
| Appendix | 155 |
| A. Appendix | 157 |
| A.1. Methane steam reforming experiments | 157 |
| A.2. Inkjet printing of a ZSM-5 precursor ink. | 157 |
| A.3. Supplementary figures and tables | 158 |

Some passages have been quoted and figures and tables reused from the following published sources.

- S. Lee, K. Schneider, J. Schumann, A. K. Mogalicherla, P. Pfeifer, R. Dittmeyer, Effect of metal precursor on Cu/ZnO/Al₂O₃ synthesized by flame spray pyrolysis for direct DME production, *Chemical Engineering Science*, 138:194 - 202, 2015.
- A. K. Mogalicherla, P. Pfeifer, S. Lee, R. Dittmeyer, Drop-on-demand inkjet printing of alumina nanoparticles in rectangular microchannels, *Microfluidics and Nanofluidics*, 16:655 - 666, 2013.
- S. Lee, T. Boeltken, A. K. Mogalicherla, U. Gerhards, P. Pfeifer, R. Dittmeyer, Inkjet printing of porous nanoparticle-based catalyst layers in microchannel reactors, *Applied Catalysis A: General*, 467:69 - 75, 2013.

1. Introduction

1.1. Motivation

Current primary energy carriers like petroleum, coal, natural gas and uranium in the long term need to be substituted by renewable energy carriers due to depletion of fossil resources, environmental pollution and high risk.

The world population is continuously growing, and then the usage of energy is not decreasing. Oil is a major energy source currently. The consumption of oil is increasing (Figure 1.1). Especially Asia where rapidly developing countries are located is consuming more and more energy. Recently, shale oil (gas) extraction was developed and extended the depletion of fossil fuels. However, consumption is predicted to remain high. This drives the current research on synthetic oil or gas from renewable sources or waste [1–6].

One of drawbacks in using fossil fuels is pollution. Especially, air pollution by emissions fossil fuel combustion are critical. Air pollution is the most serious in Asian and South & Central American countries (Figure 1.2). The usage of filters or catalytic converters can help to reduce it, however transition to low emission fuels is a principle solution. The developed countries having relatively low pollution levels are also seeking clean energy materials which can replace fossil fuels. For example, the emission regulations have become stricter and stricter [7]. Emission control systems according to this regulation are developing and at the same time the efforts for using low emission fuels are increased. In this manner electric cars are being promoted these days, but there are several challenges, which prevent a complete substitution of fossil fuel cars, such as a low capacity of batteries, low power, etc. Therefore, renewable energy carriers with a high energy density having low environmental effect are also required.

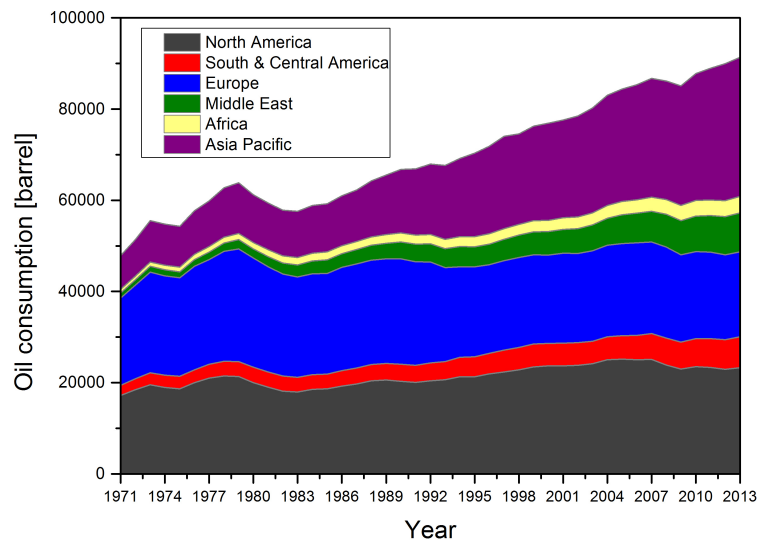


Figure 1.1.: Annual oil consumption statistics for the world [8].

In this respect, dimethyl ether (DME) is gaining great interest. It has a wide application as an energy material, propellant and chemical feedstock. It has low effects on the environment and health. It produces less pollutants when combusted. DME can be used for compression-ignition engines. DME can be produced by dehydration of methanol. The methanol is usually synthesized from syngas. Hence, the starting material of DME is syngas, which can be obtained from biomass (renewable source). Stranded natural gas or coal which is more abundant than crude oil can also be a source for DME production.

The DME production process, especially the one-stage process, is exothermic due to the methanol synthesis. The reaction heat can be a direct cause of catalyst deactivation. Therefore, effective heat removal from the catalyst is required. Microstructured reactor technology is very efficient for exothermic reactions. With high surface to volume ratio and high heat and mass transport coefficients, microstructured reactors demonstrated successful intensification of chemical reaction processes [10]. Also the direct DME synthesis could be carried out without hot spots in microstructured reactors [11].

The two-stage DME synthesis process from syngas is commercially established. The one-step process, direct synthesis, in which both methanol synthesis and dehydration take place in one reactor is currently under

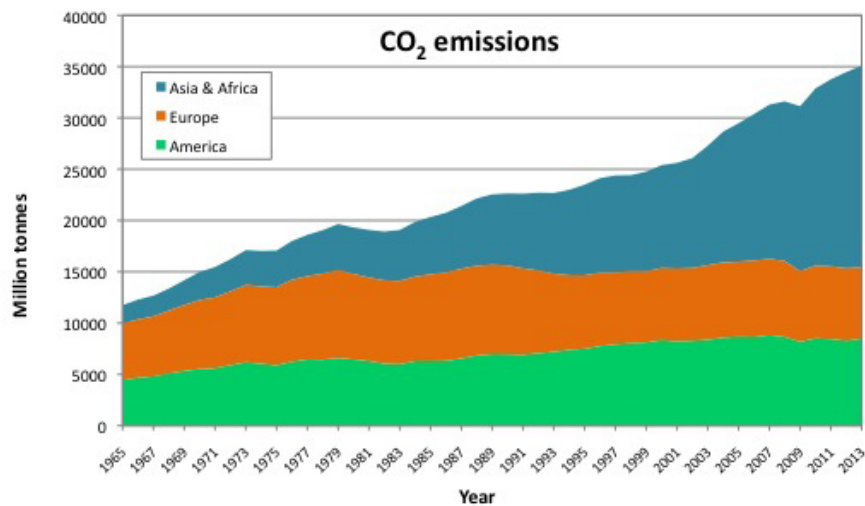


Figure 1.2.: Exposure to particulate matter with an aerodynamic diameter of $10 \mu\text{m}$ or less (PM10) in urban areas in each region 2008-2013 [9].

consideration as it can achieve higher syngas conversion by changing the thermodynamic equilibrium. Therefore, direct DME synthesis in a microstructured reactor can be a successful combination. In order to exploit the advantages of the microstructured reactor, the preparation of bifunctional catalysts, i.e a combination of a methanol synthesis catalyst and a methanol dehydration catalyst, is important. A well arranged bifunctional catalyst can enhance the selectivity toward DME [12–15]. In addition, the introduction of the bifunctional catalyst in a microstructured reactor should be considered to exploit its superior heat and mass transport properties. If the catalyst is to be coated on the microchannel surface, precise coating, good coating adhesion and control of thickness are needed. In this thesis, a double-layer configuration was chosen as a bifunctional catalyst. In the microchannels, two catalysts were deposited sequentially; a methanol synthesis catalyst as the bottom layer and a dehydration catalyst on top. The idea is that methanol is formed in the bottom layer adjacent to the channel wall, and the dehydration occurs in the top layer while methanol is diffusing back into the flow region in the microchannel. Inkjet printing technology was applied to facilitate precise deposition and thickness control of the catalyst layers in microchannels. Homogeneous and defect-free coating is required to avoid non-equal flow distribution and broadening of the residence time distribution in multi-channel arrangements [16]. In addition, in order to synthesize nanoparticles of

the Cu/ZnO/Al₂O₃ catalyst (CZA), flame spray pyrolysis (FSP) was investigated. This method can expedite nanoparticle production due to a relatively simple operation scheme.

1.2. Benefits and application of DME

DME as the simplest ether is colorless and non-toxic, and exists in the gas phase at ambient conditions. By animal toxicity studies, it was proved that DME is not carcinogenic and has a low reactivity in biological systems [17]. It is flammable, more than propane, but gets decomposed photochemically in the atmosphere. Its global warming potential is lower than methane and nitrous oxide. Hence, it has been used as an aerosol propellant instead of chlorofluorocarbons or hydrofluorocarbons, which have negative effects on the earth ozone layer and environment.

DME is also considered as an alternative fuel. Due to the similarity, it can be blended with liquefied petroleum gas (LPG). Existing infrastructures for LPG can be used for it with minor modifications. DME/LPG blended fuel showed good combustion with less soot formation [18]. This fuel is used as a household fuel in China [19].

DME is also applied in gas turbines generating electricity. The Tokyo Electric Power Company, Hitachi, General Electric and Korea Electric Power Corporation have developed power generation with DME [20]. It kept or even enhanced the performance of conventional gas turbines.

In addition, with simple modification it can be used for diesel engines. Table 1.1 shows the comparison of the properties of DME and diesel fuel. The oxygen content in DME is high while diesel does not contain any oxygen, and no C-C bond exists in DME. Therefore, it produces less particulate matter than diesel fuel. With a low boiling point, DME can evaporate quickly in the engine cylinder.

The cetane number of DME is higher than that of diesel so that DME combustion is faster and the ignition delay is shorter. The unburned fuel by the ignition delay will be less and the running of the engine smoother. Storage of DME is simple because it can be liquefied under moderate pressure (>0.5 MPa). However, due to the low viscosity, leakage has to

Table 1.1.: Properties of DME and diesel fuel [21].

| Properties | Unit | DME | Diesel |
|------------------------------------|-------------------|----------|----------|
| Molar mass | g/mol | 46 | 170 |
| Carbon content | mass% | 52.2 | 86 |
| Hydrogen content | mass% | 13 | 14 |
| Oxygen content | mass% | 34.8 | 0 |
| Carbon-to-hydrogen ratio | - | 0.337 | 0.516 |
| Critical temperature | K | 400 | 708 |
| Critical pressure | Mpa | 5.37 | 3 |
| Critical density | kg/m ³ | 259 | - |
| Liquid density | kg/m ³ | 667 | 831 |
| Relative gas density (air=1) | - | 1.59 | - |
| Cetane number | - | >55 | 40-50 |
| Auto-ignition temperature | K | 508 | 523 |
| Stoichiometric air/fuel mass ratio | - | 9 | 14.6 |
| Boiling point at 1 atm | K | 248.1 | 450-643 |
| Enthalpy of vaporisation | kJ/kg | 467.13 | 300 |
| Lower heating value | MJ/kg | 27.6 | 42.5 |
| Gaseous specific heat capacity | kJ/kg K | 2.99 | 1.7 |
| Ignition limits | vol% in air | 3.4/18.6 | 0.6/6.5 |
| Modulus of elasticity | N/m ² | 6.37E+08 | 1.49E+08 |
| Kinematic viscosity of liquid | cSt | <0.1 | 3 |
| Surface tension (at 298 K) | N/m | 0.012 | 0.027 |
| Vapour pressure (at 298 K) | kPa | 530 | 10 |

be taken into consideration in the fuel supply system. Moreover, the low lubricity of DME requires the addition of lubricants [22]. The DME injection volume should be higher since the combustion enthalpy is lower than for diesel fuel.

Overall, DME has lots of benefits compared to current liquid or gaseous chemical energy carriers, especially regarding environmental aspects. It is apparently a promising fuel. However, the supply system and infrastructure have not yet been sufficiently established. Moreover, thorough investigations of DME production and application should be carried out. For the production, renewable resources and efficient processes are required from an economical point of view.

1.3. Production of DME

DME production can be classified in one-stage and two-stage processes (figure 1.3). Both processes start from syngas. The two-stage process needs two separate reactors for the two essential reactions, methanol synthesis and methanol dehydration, whereas both reactions take place in one reactor in the one-stage process. In the following subsections, two-stage and one-stage processes will be described.

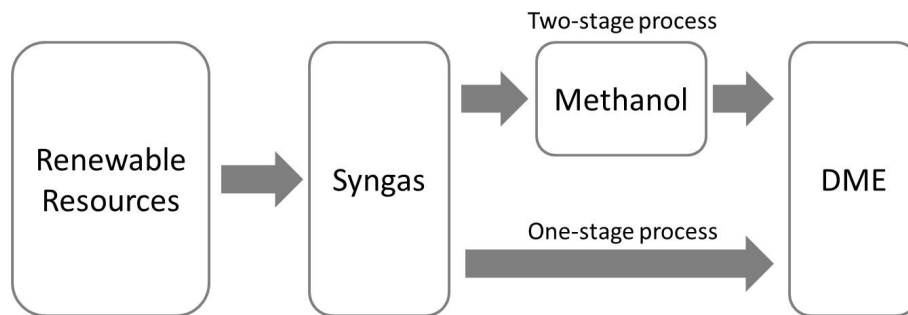


Figure 1.3.: Scheme of DME synthesis process from syngas.

1.3.1. Production of syngas

Syngas is a gas mixture of carbon monoxide, hydrogen and carbon dioxide occasionally. Syngas can be produced by various technologies. The source for syngas is also diverse. Figure 1.4 shows various routes to produce syngas. In most cases the main resources are fossil fuels. In case of hydrogen production, 96 % is produced from natural gas, liquid hydrocarbons and coal [23].

Syngas production from natural gas

Steam methane reforming (SMR)

SMR as a highly endothermic reaction uses a nickel based catalyst in industry [25]. The reaction is carried out at a temperature of 800-1000 °C and

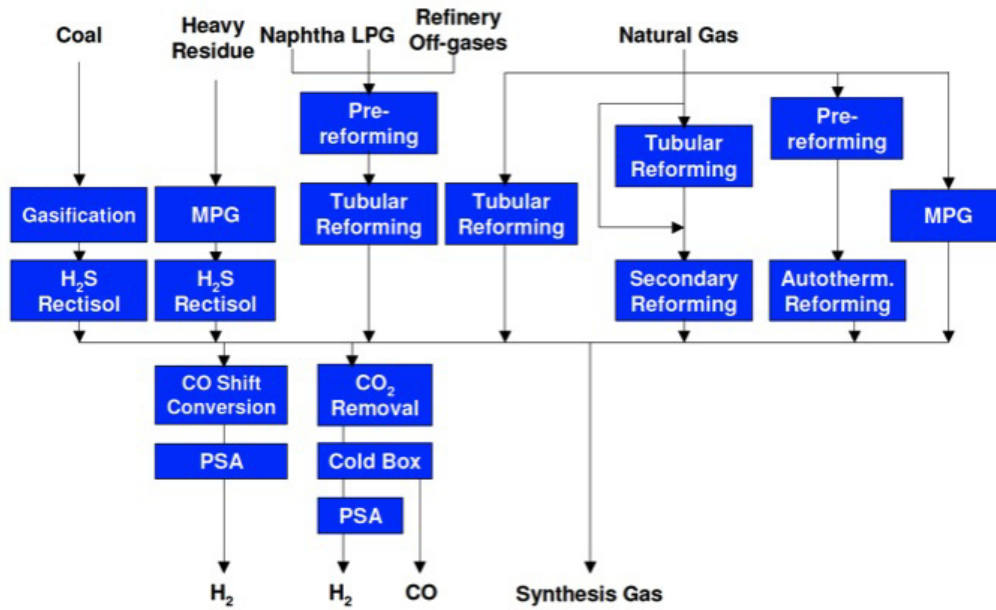
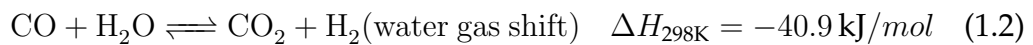


Figure 1.4.: Routes of syngas generation [24]. MPG:Multi purpose gasification, PSA:Pressure swing adsorption.

under 20-30 atm pressure [26].

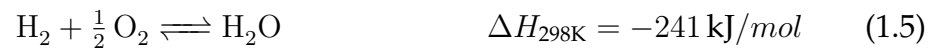


One methane molecule produces three molecules of hydrogen. Since the water gas shift reaction takes place also, more hydrogen is generated. Hence, the steam to carbon ratio can affect the ratio of the syngas components. Efficient heat supplies are well designed in SMR reactors. Fired heaters provide heat to the reactor tubes from burning of fuels [27, 28]. A heat exchanger-integrated reformer can be designed [29, 30]. This concept can reduce cost and energy losses. However, due to the lower heat flux with convective heat exchange in big equipments, a conjunct operation with another reformer is recommended [28].

Partial oxidation of methane (POX)

Partial oxidation of methane as an exothermic reaction is carried out at high temperature (800 - 1000 °C) and provides a H₂/CO ratio of 2 [26]. POX can produce syngas at high space time yields, but further oxidation of CO and

H₂ can occur [31].



Dry reforming

Methane can react with CO₂ to produce syngas. This is possible without steam addition and produces a syngas of H₂/CO ratio of 1. This syngas ratio is lower than that of SMR. It is unfavorable for methanol synthesis, but suitable for other processes, such as iron ore reduction and hydrocarbon synthesis [26].

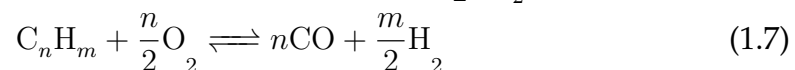
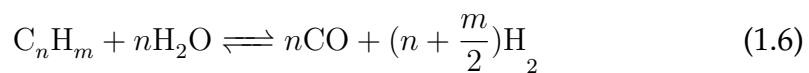
Autothermal reforming (ATR)

ATR is a combination of exothermic oxidation and endothermic steam reforming or dry reforming. All reactions takes place in one reactor, and the reaction heat from the oxidation is used for the endothermic reaction. According to the process design, a H₂/CO ratio between 1.7 and 4.7 can be obtained [28].

Syngas production from petroleum oil or coal

Petroleum oil (high hydrocarbons)

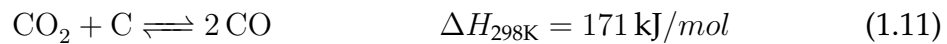
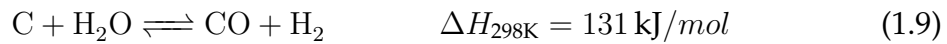
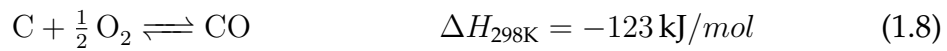
Syngas can be made also from higher hydrocarbons, e.g., liquefied petroleum gas, crude oil, heavy oil, etc. Steam reforming and partial oxidation can be applied.



However, these resources contain usually impurities such as sulfur, so that purification is often required. In case of high content of aromatic compounds H₂-deficient syngas can be produced [26].

Coal

Coal is a preferred resource with huge reserves worldwide. Coal can be converted to syngas by gasification. Oxidation and steam reforming are applied also in this process.



Same as for higher hydrocarbons, impurities should be treated, and due to the low H/C ratio of coal, the H₂/CO ratio is rather low.

Syngas production from biomass

In order to avoid usage of fossil fuels, syngas production from biomass is gaining interest. Biomass could be converted to various forms of energy such as heat, electricity, solid fuels, liquid fuels and gaseous fuels [32]. For the production of syngas from biomass, technologies such as pyrolysis, gasification or reforming are applied. This syngas as a renewable resource can be used to synthesize further valuable products. The Institute of Catalysis Research and Technology (IKFT) at Karlsruhe Institute of Technology (KIT) together with industrial partners has developed a synthesis process of fuels from sustainable biomass, which is called 'bioliq'. The bioliq process is shown in Figure 1.5. Biomass is pyrolyzed into syncrude in a twin-screw mixing reactor with hot sand. The syncrude is converted to raw syngas by high pressure entrained flow gasification. The raw syngas is purified and then synthesis of fuels, methanol and DME as well as further conversion to fuels or chemicals, is carried out. These products can be renewable energy carriers. Therefore, this thesis considers that synthesized DME is a renewable energy carrier when syngas from renewable resources is used as a starting material.

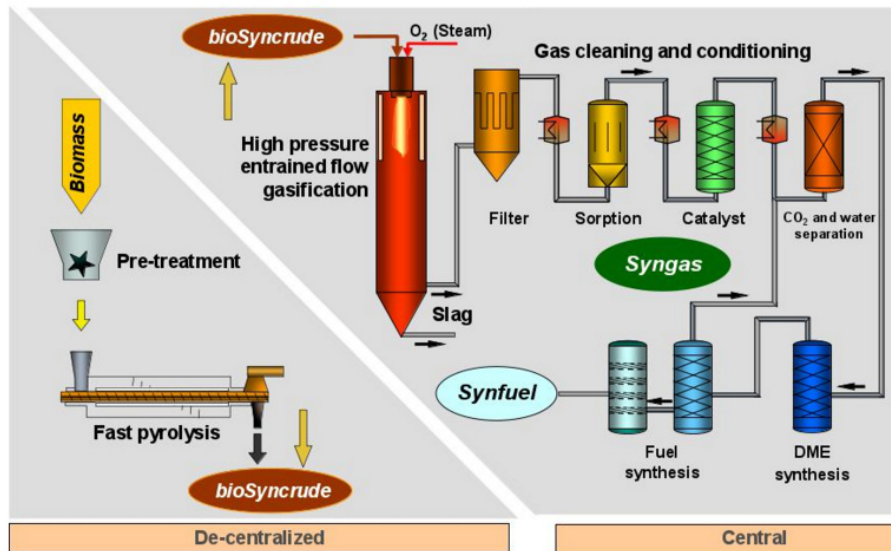
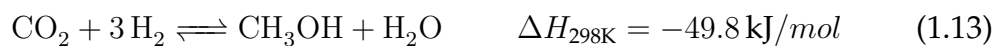


Figure 1.5.: Process flow chart of the 'bioliq' process [33].

1.3.2. Two-stage process for DME production

The conventional DME synthesis process consists of the following reactions:



CO and CO₂ are converted to methanol. As a side reaction, the water gas shift reaction exchanges CO and CO₂. This three reactions take place in the first stage of the two-stage process. In the second stage methanol is dehydrated to DME. As shown in figure 1.3, the two stages are carried out in separate units, i.e., forming a sequential process.

Methanol is one of the most important base chemicals. The world demand of methanol in 2012 was about 60 million tonnes, and it is forecasted that the demand will be 90 million tonnes in 2018 [34]. Figure 1.6 shows the value chain of methanol. About one half of the methanol production is consumed for formaldehyde, methyl tert-butyl ether (MTBE) and acetic acid [26]. It is also used for the production of olefins, methyl methacrylate and dimethyl terephthalate [35]. Methanol itself is a solvent and fuel additive. The usage

for DME is about 6 % of the total demand [36]. The demand of DME in 2012 was 4 million tonnes per year which is much lower than that of methanol [36]. Hence, the two-stage process is preferred unless the demand for DME increases. The first plants for DME production in industry were all based on the two-stage processes [37].

Toyo Engineering's two-stage process is one of the representative two-stage

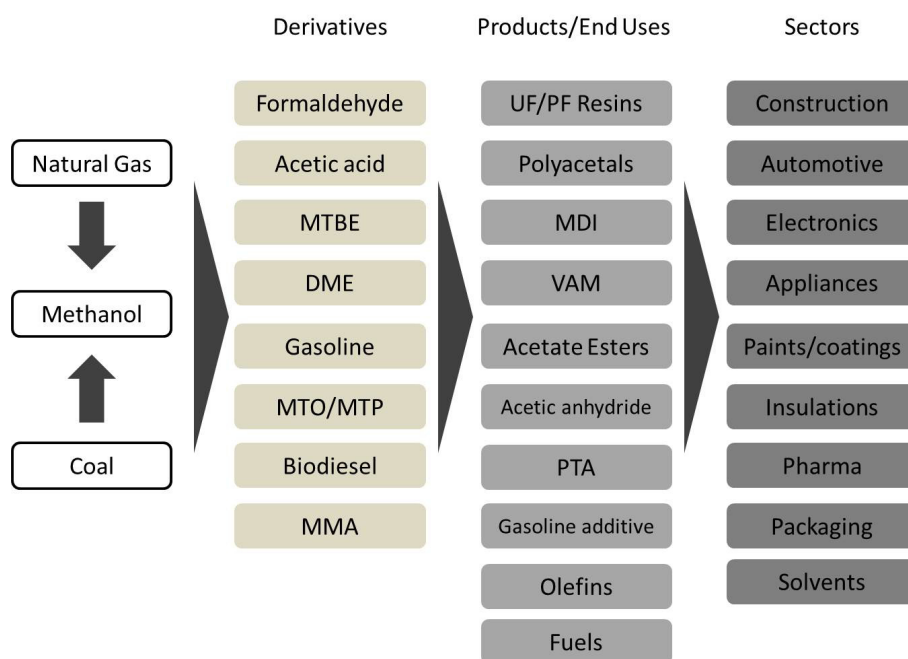


Figure 1.6.: Value chain of methanol [33].

DME processes. The DME synthesis process is attached to the methanol process [38]. Syngas is generated from natural gas by reforming. The methanol production is carried out from the produced syngas, the $(H_2 - CO_2)/(CO+CO_2)$ is approximately equal to 2 in MRF-Z[®] reactor which has been developed by Toyo Engineering [38]. The methanol production capacity is 6000 tonnes per day and the DME production capacity is maximum 3500 tonnes per day. Due to the separation of methanol synthesis and methanol dehydration in the two-stage process, each stage can use the optimum reactor and operating conditions. Another advantage is higher flexibility, since both methanol and DME can be obtained, and production strategy can be controlled according to market demand.

Figure 1.8 shows a process flow diagram of DME synthesis from methanol. DME is synthesized in a fixed-bed reactor, and in order to obtain high purity DME two distillation columns are following. Unconverted methanol

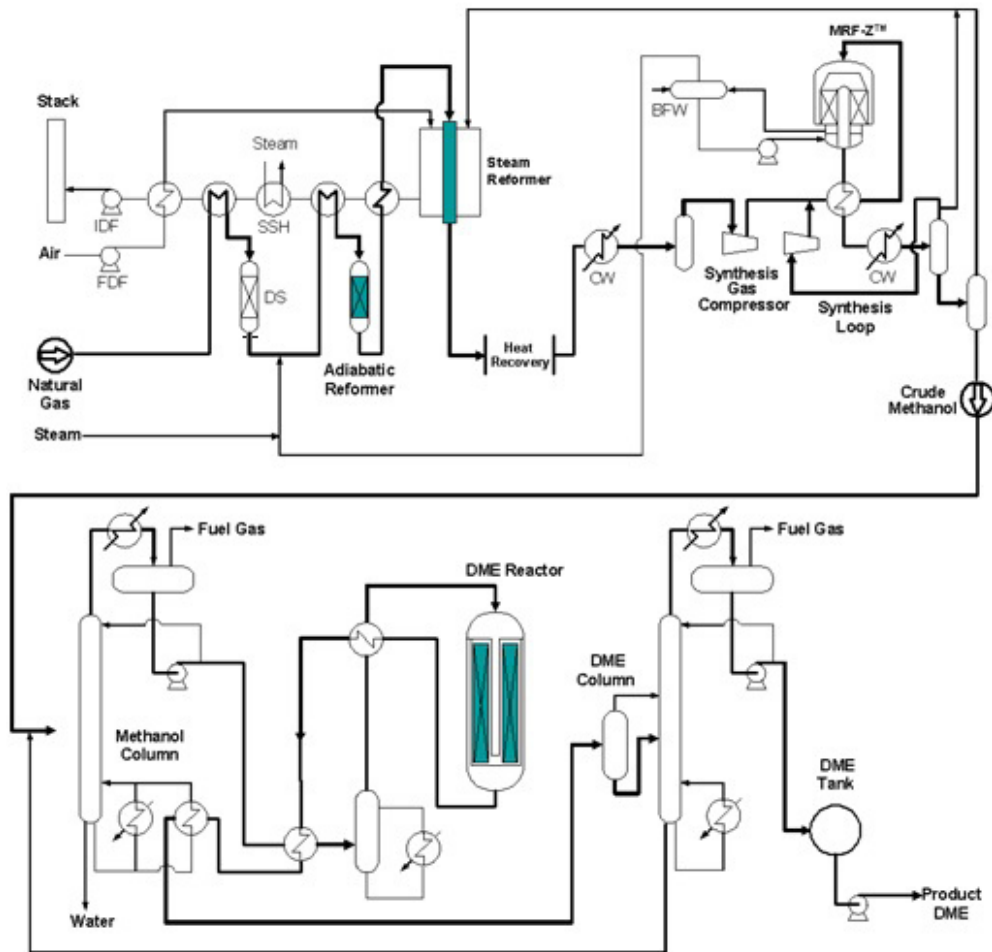


Figure 1.7.: Indirect DME production technology (Toyo Engineering) [38].

is recycled back to the reactor after the second column. This process is one of the most common processes, but requires high cost for the units, i.e. reactor, columns, heat exchangers and the associated energy [39]. Therefore, if DME production is desired without methanol production, the production cost can be reduced by simplification and intensification of the two-stage process, i.e., leading to the one-stage process.

1.3.3. One-stage process (direct DME synthesis)

The one-stage DME process is more attractive as DME is synthesized directly from syngas in one reactor. In methanol synthesis, the conversion

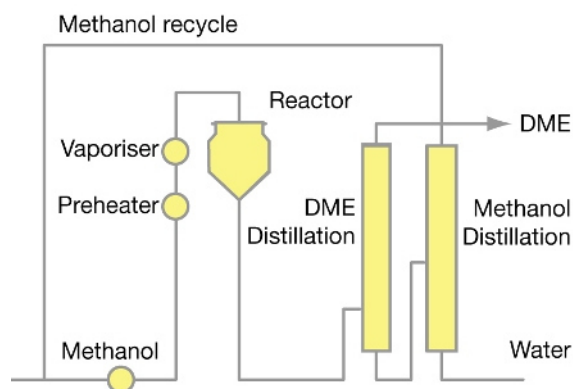


Figure 1.8.: Process diagram of DME synthesis from methanol (AkzoNobel) [40].

of syngas is restricted by the low equilibrium conversion. High pressure and a high hydrogen level are required to increase the conversion. In the one-stage DME process, the methanol synthesized from syngas is continuously consumed for DME synthesis. By the water gas shift reaction, the water is consumed, and hydrogen is generated. These effects can stimulate DME synthesis with CO-rich feed [41–43].

Figure 1.9 shows the thermodynamic equilibrium of CO conversion. The one-stage process gives higher equilibrium CO conversion at low pressure than the methanol synthesis. The feed gas composition has a significant effect on the thermodynamic equilibrium as well. Hydrogen-rich syngas favors high CO conversion. It was experimentally demonstrated that an increase of the H_2 level ($H_2/CO = 1.0 - 2$) induces higher CO conversion [44]. In the one-stage DME process, if the methanol dehydration catalyst is active enough, the methanol synthesis rate is considered to be limiting for the overall reaction rate. However, the H_2 -rich condition decreases the DME selectivity since the water gas shift reaction is suppressed by high H_2 content [44].

The one-stage process has been adopted in several countries. In Japan, JFE group established the JFE direct process project in 2001. Since 1989 JFE has been working on catalyst development for the one-stage DME synthesis with liquid phase slurry reactors [46]. A 100 tonnes per day pilot plant project was started at the same time [47]. In South Korea, KOGAS has developed a direct DME synthesis process from natural gas (Figure 1.10). DME could be synthesized from a syngas produced from natural gas with

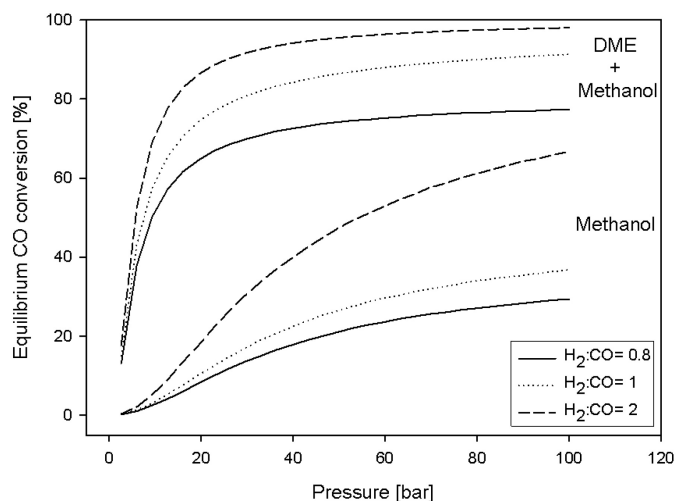


Figure 1.9.: Thermodynamic equilibrium CO conversion of the methanol synthesis and the one-stage DME process. Conditions: $T = 250\text{ }^{\circ}\text{C}$ and $\text{H}_2:\text{CO}:\text{N}_2:\text{CO}_2 = 2:1:0.35:0.13$ [45].

10 % of CO_2 [48]. In 2008, a 10 tonnes per day demonstration plant was established, and the construction of a 1000 tonnes per day commercial plant started in 2013 [49].

1.4. Reactions and catalysts for DME synthesis

1.4.1. Methanol synthesis reaction and catalysts

Syngas can be converted to methanol on heterogeneous catalysts. This reaction has been developed and commercialized since the early 20th century. Usually, Cu is the active catalyst for this reaction. Cu-based catalysts have been used in the industry since the 1950s. It has been revealed that together with promoters, metal oxides, the activity of copper is enhanced [35]. Metallic copper can produce methanol, but is not stable due to the sintering of copper particles [50]. The presence of ZnO and Al_2O_3 in addition to copper can promote the catalytic activity and prevent the sintering of copper [30]. Other promoters have been also studied to enhance the activity. For example, ZrO_2 could slow down the reverse water gas shift reaction and promote methanol synthesis [51]. Instead of Cu-based

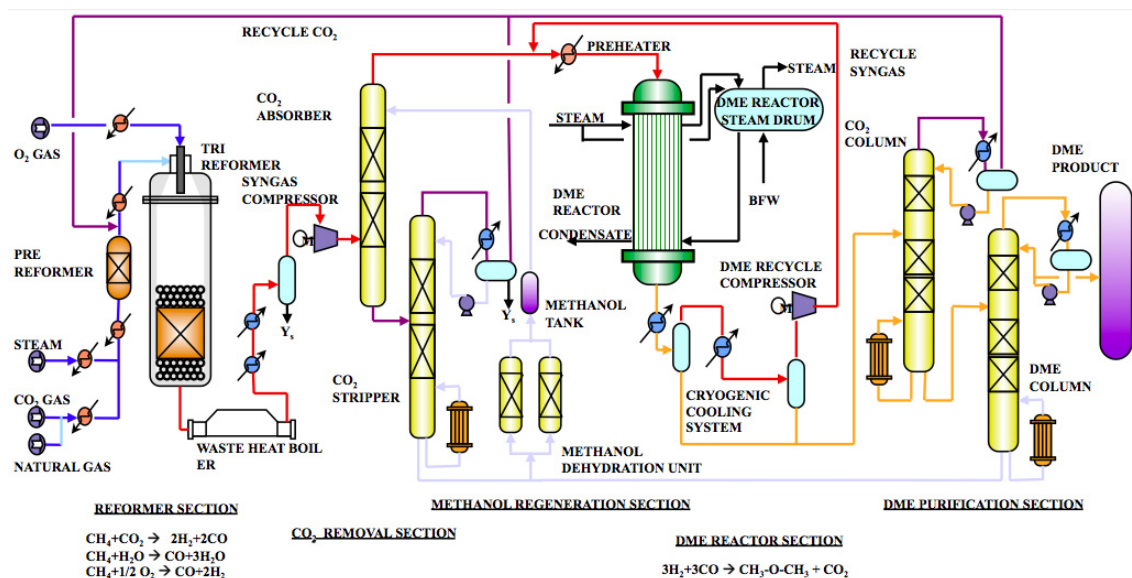


Figure 1.10.: DME synthesis process at KOGAS [49].

catalysts, precious metals such as Pd, Rh and Au can also be utilized for methanol synthesis. However, Cu-based catalysts are more practical in terms of performance per price.

Cu/ZnO/Al₂O₃ is widely employed in the industrial methanol synthesis process. One of the common synthesis methods for Cu/ZnO/Al₂O₃ is co-precipitation [32]. By this method, metal precursors form spinel zincian malachite structures with needle shape, and then the following calcination generates spherical CuO/ZnO catalyst particles. An activation of this catalyst by reduction of CuO is needed before carrying out the reaction since Cu/ZnO is the active catalyst. In addition to the role of ZnO as a protector against Cu sintering, Cu surfaces with decoration by zinc oxide show enhanced activity for methanol synthesis [52]. Consequently, the ratio between active metal and promoter, and their structure are strongly related to the catalytic activity. The synthesis parameters of Cu/ZnO/Al₂O₃ should be well controlled for high activity. For the reduction of copper catalysts, industrially pure H₂ gas with dilution gas (N₂ or natural gas) is applied at low temperature. The temperature reaches up to 490-510 K. At this condition, only CuO is reduced to metallic copper. Zinc remains in ZnO state.

The Cu/ZnO catalyst is very susceptible to deactivation and poisoning. Metallic copper particles easily sinter and get deactivated by excess heat. Hence, the industrial methanol synthesis temperature is not above

573 K [35]. It has been reported that at severe reduction conditions CuO/ZnO catalyst can be irreversibly deactivated due to the formation of brass (Cu_nZn) [53, 54]. Sulfur and chlorine deactivates the catalyst permanently. Sulfur is easily adsorbed on the catalyst surface. Chlorine is a more dangerous poison. It is adsorbed on the copper and zinc surface whereby sintering is accelerated. Fe is a strong poison which induces the Fischer-Tropsch reaction.

While methanol synthesis catalysts have been developed, the carbon source of methanol has been embroiled in controversy. Both CO and CO_2 can be hydrogenated. According to isotope exchange studies with $^{14}\text{CO}_2/^{12}\text{CO}$ feed [55], methanol synthesis from CO_2 is dominant. CO hydrogenation is slower. This work was supported by other research reports [56–58]. Ideally, waste CO_2 can be used to produce valuable methanol, as CO_2 is the preferred carbon source. For the conversion of CO_2 -rich feed to methanol, Cu/ZnO catalysts can be used, but it is more optimized for CO-rich feeds [59]. Nevertheless, Cu is considered an essential component for methanol synthesis so that promising catalysts using Cu for CO_2 activation have been reported [60, 61].

For industrial methanol synthesis reactors, many factors have to be considered in order to achieve an economic production; for example, recovery of the reaction heat, low catalyst volume, low by-product formation and high conversion. Internally cooled reactors are employed by several chemical companies (Lurgi, Topsoe, Linde and Mitsubishi Heavy Industries). The catalyst is equipped in tubes, the heat is exchanged with boiling water. The reactors are easy to control, but high cost and restricted size are disadvantages. A combination of a water-cooled reactor (WCR) and a gas-cooled reactor (GCR) was designed by Lurgi (Figure 1.11) [62]. The reaction gas enters into the WCR in which catalysts are filled in tubes surrounded by boiling water. The converted gas goes to the shell side of the GCR. The reaction heat from the GCR is used for preheating the inlet gas. This reactor system provides high syngas conversion efficiency and energy efficiency with low investment cost. [63]. Another alternative is the slurry phase reactor. Here, the catalyst is immersed in a liquid hydrocarbon. Air Products developed a liquid-phase methanol process (LPMeOHTM) with this type of reactor (Figure 1.12) [64]. The liquid phase absorbs the reaction heat so that the process shows good temperature control. The LPMeOHTM reactor can operate with CO-rich syngas (in excess of 50 %) [64].

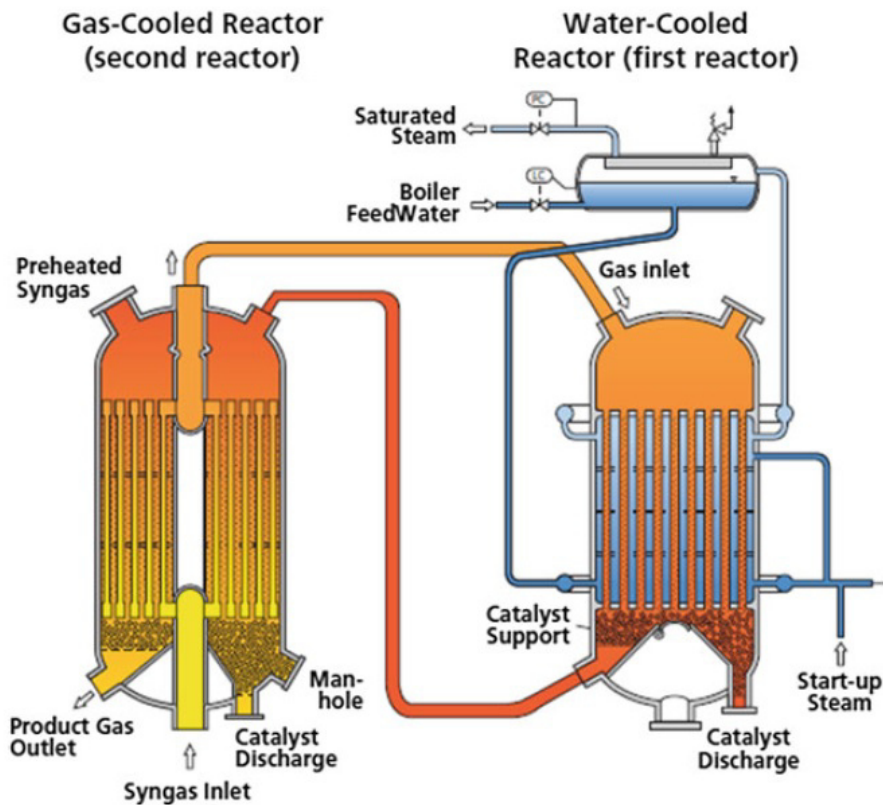


Figure 1.11.: Lurgi combined methanol synthesis reactor system [62].

1.4.2. Methanol dehydration reaction and catalysts

Dehydration of methanol takes place on acidic catalysts. Solid-acid catalysts such as γ -alumina, silica-alumina and zeolites are commonly used. As shown in the reaction equation of methanol dehydration, water is a side product. These catalysts can be deactivated by the presence of water. On the surface of alumina or aluminosilicates, water can be chemisorbed and modify the structure.

As shown in figure 1.13, in case of γ -alumina the water chemisorbed on the tetrahedrally coordinated Al sites (Lewis acidic sites; strong acidity) hydrates to octahedral coordination [65]. In turn, the surface acidity is reduced. Therefore, surface modified γ -alumina catalysts, $\text{Ti}(\text{SO}_4)_2/\text{Al}_2\text{O}_3$ or $\text{SiO}_2/\text{Al}_2\text{O}_3$ showed enhanced activity and stability [66, 67].

ZSM-5 is a commonly employed zeolite for methanol to DME conversion.

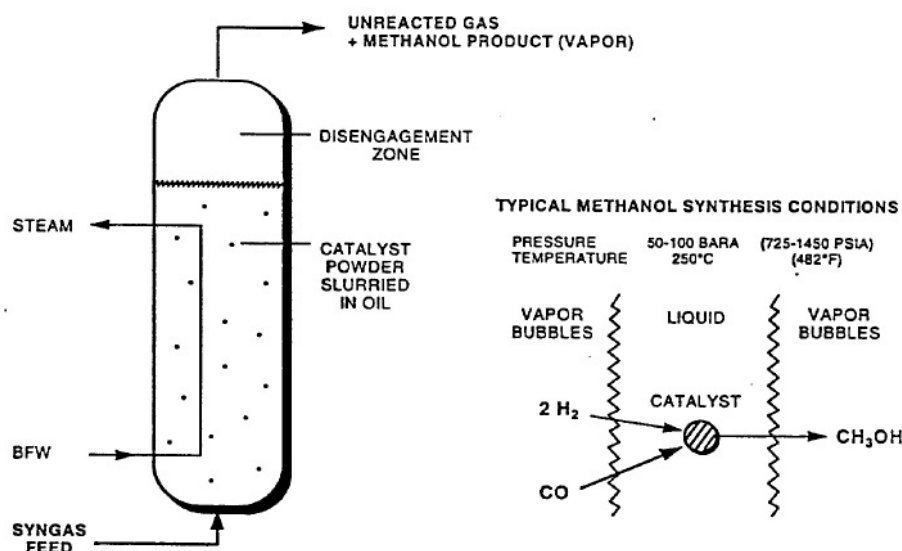


Figure 1.12.: LPMethanol™ reactor and reaction schematics [64].

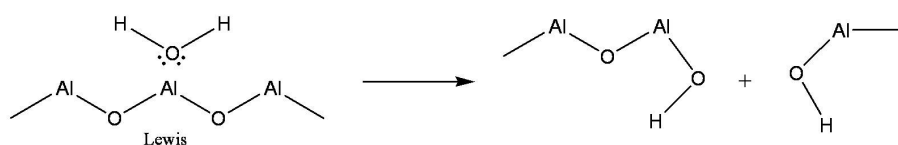


Figure 1.13.: Hydration of γ -alumina [65].

A general conclusion in methanol dehydration is that the acid property is important for the activity for DME formation, selectivity and catalyst stability [67–69]. ZSM-5 has been found to be more favorable as a dehydration catalyst than γ -alumina [70]. The deactivation effect by water is much less than on γ -alumina because of its hydrophobicity and predominance of Brønsted acidity [71–73].

Garcia-Trenco et al. [74] reported the role and effect of zeolite acidity for methanol dehydration. The effect of Brønsted and Lewis acidity was investigated. The methanol dehydration rate and the density of strong Brønsted acid sites showed a linear correlation. (Figure 1.14). However, acid-treated H-ZSM-5 (HZA) possessing dominantly Brønsted acid sites with less Lewis acid sites showed lower activity than the original ZSM-5 (HZ). Too strong Brønsted acid sites can cause undesired conversion of DME to hydrocarbons [75]. Figure 1.14 also shows the effect of Lewis acidity. Lewis acid sites from ion-exchanged Na⁺ or Co²⁺ could not enhance the activity. According to another report, dominant Lewis acidity by Al can also induce hydrocarbon formation from DME [76].

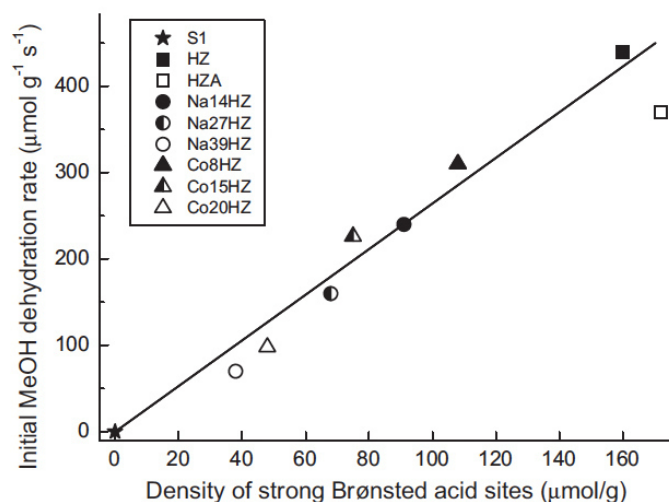


Figure 1.14.: Correlation between the initial methanol dehydration rate for the studied zeolites and the density of strong Brønsted acid sites as determined by FTIR-pyridine at a pyridine desorption temperature of 673 K. Methanol dehydration conditions: fixed-bed reactor, 533 K, 1 bar, 15 - 30 mg of zeolite, MeOH: N₂ molar ratio = 20:80, total flow rate = 150 mL/min. HZ is H-ZSM-5, HZA is acid treated H-ZSM-5 [74].

1.4.3. Bifunctional catalysts for the one-stage process

As mentioned in the above section, the one-stage process like methanol synthesis is an equilibrium limited exothermic reaction process. Although the equilibrium syngas conversion is more favorable than for sole methanol synthesis, one of the most important points in the one-stage process is catalyst integration [12, 69, 77, 78]; the methanol synthesis catalyst (CZA) and the dehydration catalyst (ZSM-5) are in one reactor by one of following methods, respectively.

Mechanical mixing

Mechanical (physical) mixing is the most common and simplest method to get a catalyst bed for one-stage DME synthesis [69, 74, 79]. Catalyst particles of both methanol synthesis and dehydration catalyst are mixed mechanically without any special treatment. It is normally employed for packed bed reactors [45]. Beyond this simple mixing, specially designed 'bifunctional' catalysts can provide enhanced catalytic performance [80–82].

Co-precipitation

Bae et al. [77] have reported co-precipitation of Cu/ZnO/Al₂O₃ and γ -Al₂O₃. In order to obtain high yield of DME with low CO₂ production, Cu/ZnO/Al₂O₃ should be well dispersed on the γ -Al₂O₃. They could achieve a high dispersion of Cu/ZnO/Al₂O₃ by controlling the aging time during co-precipitation.

Ahmad et al. [83] showed the co-precipitation of Cu/ZnO/Al₂O₃ with ZSM-5. By comparison of two precipitating agents, the influence on catalyst structure and surface area was investigated. This report suggested that oxalic acid as precipitating agent can give better catalytic performance than sodium carbonate.

Core-shell

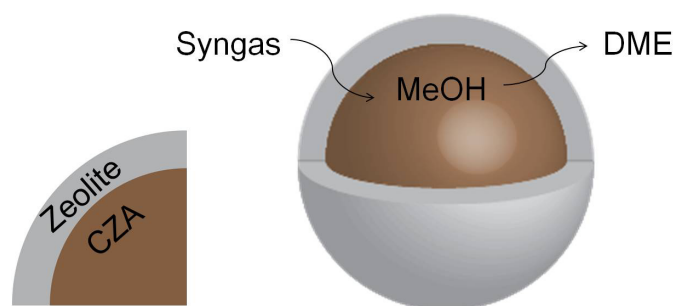


Figure 1.15.: Illustration of a core-shell type bifunctional catalyst.

Another interesting type of bifunctional catalysts is a core-shell structure. High DME selectivities can be obtained by using a core-shell type catalyst having CZA catalyst as a core and porous solid acidic catalysts, e.g. zeolites, as the shell [12, 82, 84]. In the core-shell catalyst, the CZA catalyst converts syngas into methanol in the core, and methanol is dehydrated to DME when it diffuses out through the zeolite shell (Figure 1.15). One of the challenges in the core-shell catalyst synthesis is the deactivation of the core catalyst. Copper oxides can be easily dissolved in the basic ZSM-5 synthesis mixture. Na⁺ in the ZSM-5 synthesis mixture is a poison for the CZA catalyst [12]. Therefore, modified ZSM-5 synthesis methods have to be studied for the core-shell synthesis. Researchers from the Institute of Chemical Reaction Engineering (CRT) at the University of Erlangen-Nuremberg (FAU) (a cooperating partner of this thesis) have synthesized core-shell catalysts by in situ seeding and secondary growth (Figure 1.16). The core catalyst, CZA, was coated first with silicalite-1 seeds and then growth of ZSM-5 particles

was carried out sequentially.

The core-shell system generates an additional diffusion barrier for the syngas to the CZA catalyst. To identify the optimal shell thickness and zeolite pore structural properties is essential for maximizing the performance of a core-shell system.

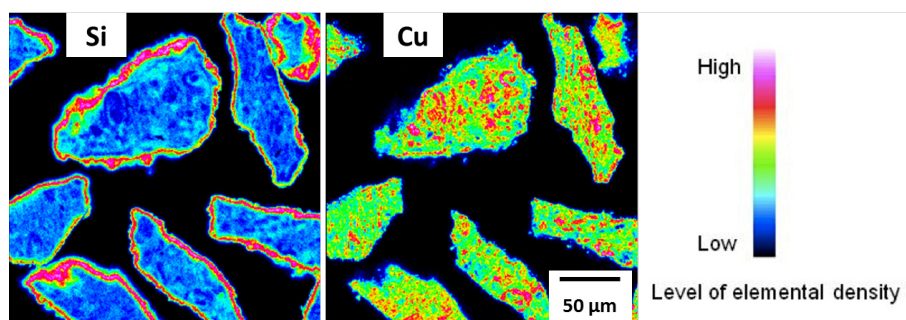


Figure 1.16.: Cross-sectional electron probe microanalysis (EPMA) images with elemental mapping of core-shell particles. Si and Cu represent ZSM-5 and CZA catalyst, respectively.

Double-layer

The core-shell system can also be implemented in the form of a catalytic double-layer with CZA as a bottom layer and zeolite as a top layer in microchannel reactors (Figure 1.17). This type can be applied where the reactor has catalyst-coated walls. To achieve it, both catalysts should be uniformly distributed along the reactor wall. As the shell thickness and uniform structure in the core-shell catalyst is critical, the top layer thickness should be optimized and an effective coating method for the double-layer must be worked out. In this thesis, this type of double-layer catalyst was applied in a microchannel reactor.

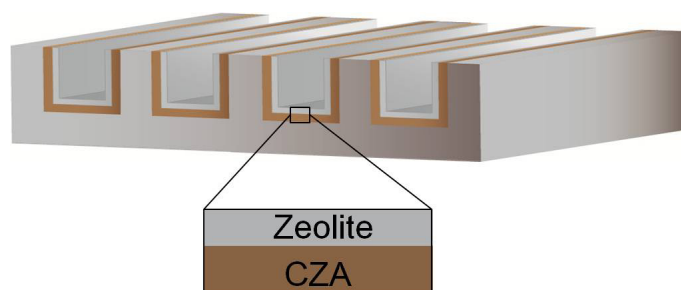


Figure 1.17.: Illustration of a double-layer type bifunctional catalyst.

1.5. Microstructured reactors

A microstructured device for process engineering is characterized by internal flow areas which have at least one lateral dimension in the micrometer range, i.e., below 1 mm. It is applicable to thermal or chemical process engineering e.g. heat exchange, mixing and chemical reactions [85]. When this device is designed for chemical reactions, it is also often called 'microreactor'. This refers not only to the flow channel with dimensions in the micron scale, but usually also the size of the reactor. However, such a device may contain numerous individual channels that provide huge area, and may reach sizable dimensions so that the term microstructured reactor is more apprehensible. Since the high heat and mass transport rate are characteristic advantages of microstructured reactors, precise control of the reaction conditions such as temperature and mixing is possible.

1.5.1. Advantages of microstructured reactors

Microstructured reactors have been intensively researched because of its attractive advantages regarding heat and mass transport rates, high space time yield and improved safety [86–89].

Microstructured reactors show a high surface-to-volume ratio due to the small channel height. This ratio is typically a factor of 10 - 100 higher than for conventional reactors [86]. Therefore, efficient heat exchange between the catalyst bed and the reactor wall can be expected.

Scaling up of microstructured reactors is often easier than for conventional reactors. Instead of increasing the reactor size, increasing the number of microchannels basically can enlarge the production [90, 91]. Nevertheless, different designs of a large scale reactor are sometimes required in order to avoid dissimilar performance such as flow maldistribution. Due to the small diameters of the microchannels, a small amount of reactants is reacted in one microchannel. This allows to improve the operational safety.

1.5.2. Introduction of catalysts in microstructured reactors

Two main methods for catalyst introduction can be considered. When the catalyst particles fill the microchannel space, it becomes a packed bed system. In this case, the microchannel dimension, especially length, should be well designed to avoid excessive pressure drop and to achieve uniform flow distribution. Microstructured reactors for packed bed systems are flexible regarding the use of different catalysts. The catalyst loaded into the system can be removed rather easily, and the reactor will be ready for the next catalyst. The second type is a catalyst coating on the microchannel wall. In this type, the catalyst layer is fixed so that an exchange of catalyst is not possible. The catalytic performance of this system is influenced by the quality of the catalyst layer. Non-uniform catalyst layers in microchannels can lead to reactant flow maldistribution and a drop in reactor performance [16]. Another issue is undesired coating on the fins and side bands when coating open microchannel structures. This may create problems during stacking and joining of coated foils. Therefore, a proper coating method should be developed. Many coating techniques have been demonstrated in the literature for laboratory microchannel reactors [16, 86, 92–95].

Anodic oxidation of aluminum foils

This coating method uses aluminum based microchannels, and the surface of the microchannel is anodically oxidized. An Al_2O_3 layer forms on the microchannel walls. The thickness of the oxide layer can be adjusted with this technique. The produced oxide layer is quite homogeneous and reproducible (Figure 1.18) Pore density and oxidation efficiency depend on the electrolyte, temperature and electric potential. The formed porous oxide layers are usually used as catalyst supports for catalytically active components [96].

Sol-gel coating

One of the widely used methods for surface coating (walls) is the sol-gel method. It facilitates metal oxide coatings with high porosity, which can be used as catalyst supports or catalytic coatings themselves. By appropriate

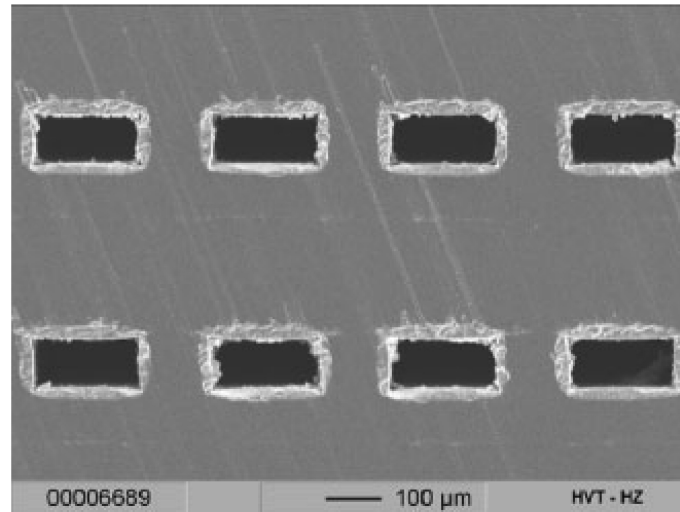


Figure 1.18.: Cross sectional SEM image of anodically oxidized microchannels [94].

preparation of the sol-gel metal precursor, a multi component catalyst coating is also possible. Two options for the sol-gel precursor of metal oxides have been suggested; aqueous metal salt solutions or metal alkoxides formation by hydrolysis and polycondensation [95]. In the aqueous metal salt solution, metals exist as metal ions so that further treatment to form a metal oxide layer should be well established. The latter uses a metal oxide colloidal suspension. In this process, the hydrolysed metal precursors form a polymeric network by polycondensation. The metal sol-gel can be coated on microchannel substrates, and by heat treatment, drying and calcination the metal oxide layer is formed. In order to increase the porosity of the metal oxide layer, pore- or structure-directing agents can be used, which is usually done for ordered porous materials [97].

With this method, zeolite coatings can be established. The common zeolite synthesis uses aluminosilicon alkoxide prepared by acid or base treatment. In order to make crystalline material, high pressure and temperature treatment are required. Iglesia et al. [98] showed zeolite coating and growth on microchannels. Two methods were compared in this study. A microchannel plate was immersed in the precursor solution or stood above water during hydrothermal treatment in the autoclave (Figure 1.19). In the latter, the microchannel was treated previously with zeolite seeds only within the microchannels, i.e., not on the fins in order to make a selective zeolite coating. The steam generated from the water assists crystallization of the zeolite and further prevents undesirable zeolite growth on the fins.

They observed that a long crystallization time is required for the steam assisted method. The formed zeolite layer was thin and uniform, and Pt was successfully introduced by ion-exchange procedures. These studies have shown well-crystallized zeolite coatings and its selective growth on microchannels.

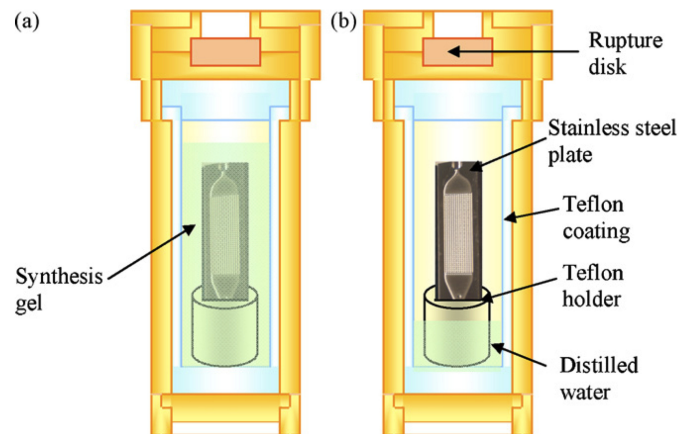


Figure 1.19.: Scheme of zeolite coating in microchannels by using in situ crystallization. (a) immersion of microchannel in the precursor gel, (b) steam assisted method [98].

There are some challenging points in the sol-gel coating. The sol-gel precursor should be precisely deposited in a confined microchannel space. The coating adhesion depends on the material combination of catalyst and microchannel substrate as well as on the surface conditions. Therefore, a deliberate design is necessary for high coating adhesion.

Wash coating with catalyst particles

Catalyst particles are prepared and a catalyst dispersion with small enough particle size (favorably nanoparticles) is formed. Then, the microchannel foil can be wash-coated with catalyst particles [99, 100]. The catalyst particles on the microchannel walls are sintered after the drying process and form a porous structure. This method can directly coat active catalysts on microchannel walls without further impregnation of active metals. It is widely used for monoliths [101–103]. For this method, especially on metallic microchannel substrates, selective coating only in the microchannels and coating adhesion are challenging points.

Electrophoretic deposition (EPD)

When the microchannel is electrically conductive and a suspension of catalyst nanoparticles is prepared, this method can be applied for catalyst coating in microchannels [104]. The colloidal catalyst nanoparticles move to the electrode (microchannel) by electrophoresis. The properties of the coating can be controlled by the process parameters such as voltage, temperature, time and pH value.

Chemical vapor deposition (CVD)

When the surface of the microchannel is already a porous ceramic layer, CVD provides the deposition of active metal catalysts on the support layer. Janicke et al. [105] showed CVD deposition of platinum into alumina coated microchannels for safe water formation from explosive hydrogen/oxygen mixture.

1.5.3. Application to DME synthesis

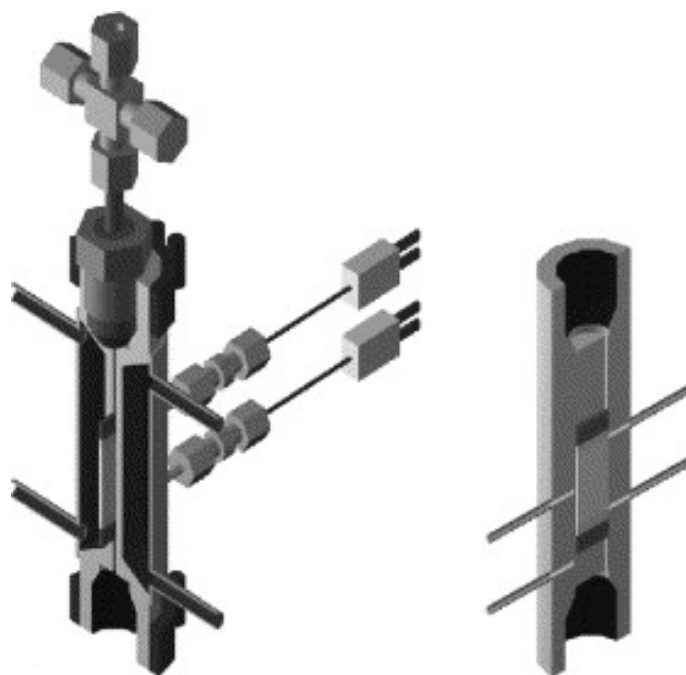


Figure 1.20.: Scheme of the microchannel reactor of Hu et al. [106].

Microstructured reactors are useful for exothermic reactions. Hence process intensification for DME synthesis from syngas is expected in microstructured reactors. Several research groups reported on the

effectiveness of this approach.

Hu et al. [79] used a fixed-bed type microchannel reactor (Figure 1.20). Microchannels were designed with 0.508 mm width. The microchannel foil was covered with two oil-heating systems to maintain good heat transfer. With this reactor, they could obtain higher space time yield than for a conventional slurry reactor in direct DME synthesis. This microchannel reactor showed good stability of the catalyst without hot spots in a long term reaction test.

Hayer et al. [107] and Tauro [45] used a micro packed-bed reactor which was manufactured by Institute for the Micro Process Engineering (IMVT) at Karlsruhe Institute of Technology (KIT) (Figure 1.21). The reactor has reaction platelets with cylindrical pillars. Heat exchange platelets are located between the reaction platelets in cross flow. By reactor modelling it has been shown that the micro packed-bed reactor provides a uniform temperature profile along the reactor channel. The temperature deviation was less than 2 K, lower than for a conventional laboratory fixed bed reactor. Experimentally, this advantage led to good performance in DME production in the direct DME synthesis.



Figure 1.21.: Micropacked bed reactor.

1.6. Contribution of the thesis

This thesis was supported by the focused programme 1570 of the German Research Foundation DFG: Porous media with defined pore structure for process engineering — modelling, application, synthesis, through the project "Bifunctional hierarchical porous layered systems for efficient one-stage conversion of synthesis gas to liquid fuels in microreactors. Two institutes, IMVT at KIT and CRT at FAU, collaborate for this project. The project aims at efficient syngas conversion to DME with novel bifunctional catalysts in microstructured reactors. Two bifunctional concepts were proposed, core-shell (Figure 1.15) and double-layer (Figure 1.17) catalysts. The CRT group focuses on the synthesis of core-shell catalysts and the IMVT group on the preparation of double-layer catalyst in microchannels. Besides, simulation works regarding the pore structure of the zeolite layers and the catalytic reactions were carried out together. Eventually, catalysts preparation and integration, activity evaluation and simulation are aligned according to Figure 1.22. This thesis contributes to the whole effort regarding CZA catalyst preparation, catalyst coating in microchannels, establishment of double-layer catalysts and its activity evaluation. Regarding the CZA catalyst preparation, flame spray pyrolysis was developed. In order to substantiate double-layer catalyst coatings in microchannels, inkjet printing technology was adopted and developed.

1.7. Outline of the thesis

This thesis consists of six chapters.

Chapter 1 Introduction

The objective and motivation are described. General literature survey and background are mentioned.

Chapter 2 Materials and method

Preparation of catalysts, characterization methods, reactors used, coating methods and experimental procedure of activity tests are described.

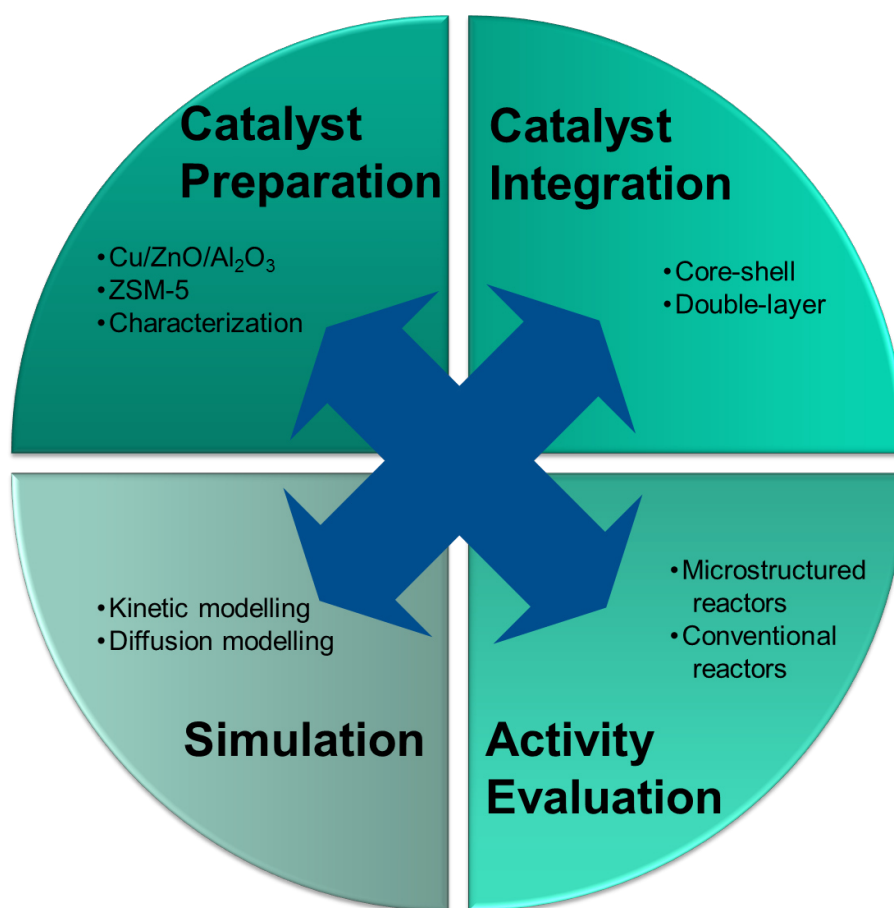


Figure 1.22.: Cooperation of CRT and IMVT in the DFG-focused programme.

Chapter 3 Investigation of Cu/ZnO/Al₂O₃ (CZA) via flame spray pyrolysis (FSP)

The FSP method for catalyst synthesis and the characterization of the produced catalysts are presented. By investigation of metal precursor effect in FSP synthesis, the most reliable CZA catalyst was selected. The catalytic activity of FSP-CZA was tested for direct DME synthesis.

Chapter 4 Inkjet printing for catalyst coating into microchannels

Inkjet printing methods for well-designed catalyst coatings in the microchannels are described. Catalyst ink formulation and demonstration of catalyst coating in microchannels are mentioned.

Chapter 5 Direct DME synthesis over double-layer catalysts in microchannel

Experimental works for double-layer catalyst formation in microchannels by using inkjet printing and its application for the direct DME synthesis are

described.

Chapter 6 Conclusion and outlook

Conclusions obtained through all studies and future perspectives are highlighted.

2. Materials and methods

2.1. Catalyst preparation

2.1.1. CZA synthesis via FSP

Flame processes are widely applied for the synthesis of nanoparticles such as fumed silica, carbon blacks, alumina and titania [108]. Moreover, as catalysts synthesized by the flame processes showed reliable catalytic properties, alternative synthesis routes using the flame processes have been researched [109–111]. In this work, flame spray pyrolysis (FSP), one of the flame processes was applied for CZA catalyst synthesis [112]. Two general types of metal precursors were applied to synthesize CZA by FSP; one type was based on nitrate precursors, the other was based on organometallic compounds. The nitrate based precursor solutions (Type A) were prepared by mixing copper (II) nitrate tri-hydrate (Sigma-Aldrich, > 99 %), zinc nitrate hexa-hydrate (Sigma-Aldrich, > 99 %) and aluminum nitrate nona-hydrate (ChemPur, 98.5 %) in ethanol. Different molar ratios of copper, zinc and aluminum were prepared (Cu:Zn:Al = 5:4:1, 6:3:1 and 7:2:1) and are abbreviated as A541, A631 and A721 respectively. The organometallic precursor solutions (Type B) were prepared with copper bis-2-ethylhexanoate (Alfa Aesar, 98%), zinc bis-2-ethylhexanoate (Alfa Aesar, 80 % in mineral spirits) and aluminum sec-butoxide (Alfa Aesar, 97 %), and a di-methylformamide (DMF)/xylene mixture (volume ratio = 1/1) was used as a solvent. The same three different molar ratios were prepared for Type B samples, and are abbreviated as B541, B631 and B721. The total molar concentration of the metal precursors in all solutions was set to 0.5 M.

A flame generator (NanoPowderNozzle[®]) and collection cylinder purchased from Tethis (Milano, Italy) was set up in a fume hood. Figure 2.1

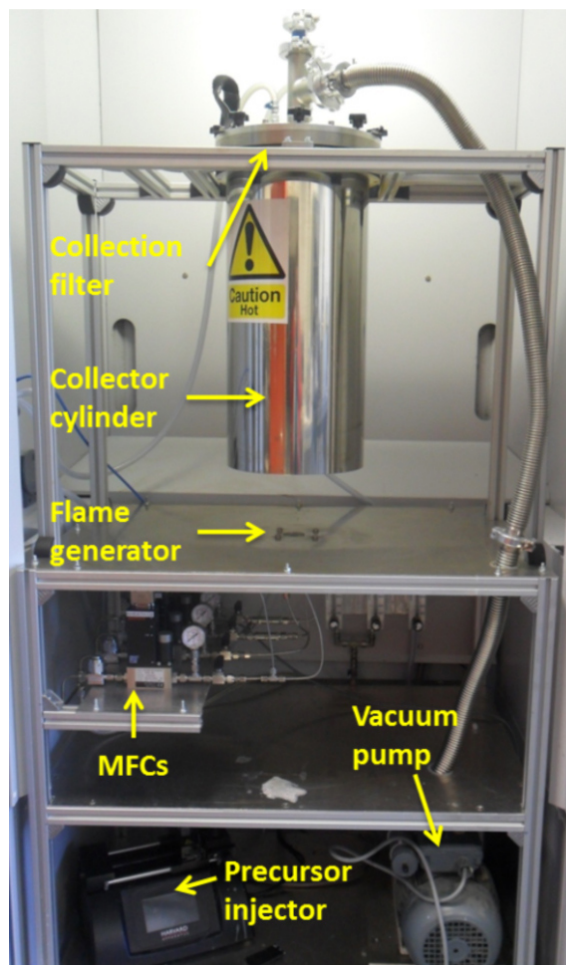


Figure 2.1.: Picture of the flame spray pyrolysis system installed at IMVT.

shows the installed FSP apparatus. The flame generator was located in the middle of the table. Under it all the gas lines were connected. The gas flows were controlled by Brooks mass flow controllers (MFCs). Furthermore, metal precursor lines were connected beneath the flame generator. Above the flame generator a collection cylinder was hanged with a gap between them. On top of the collection cylinder, a collection filter was located and connected to a vacuum pump.

The scheme of the flame generator used for this study is shown in Figure 2.2. At the center of the flame generator, there is a needle connecting it to the metal precursor solution. The metal precursor solution was fed to the needle by a syringe pump (PHD UltraTM, Harvard). Dispersion gas (O₂) was fed through the gap around the nozzle of the needle. Supporting flame

gas (mixture of CH_4 and O_2) holes are in place around the nozzle. Sheath gas was fed to the outermost gas line.

Operating procedure

The operating procedure of FSP for CZA has been adapted from previous studies [113–115]. At first, a supporting flame was generated by CH_4 and O_2 mixture with a flow rate of 0.5 L/min and 1.9 L/min, respectively. Additional dispersion gas (O_2) was fed with a flow rate of 3.5 L/min, and pressure at the nozzle tip was kept at 2 bar. The metal precursor solution was fed to the nozzle inside of the supporting flame with a flow rate of 5 ml/min. Thereby, the main flame was generated and particle production was started. In order to stabilize the main flame, sheath gas (O_2) was fed with 5 L/min flow rate. A vacuum pump facilitated particle deposition on a glass fiber filter on top of the collection cylinder. After finishing the particle generation and cooling down, the deposited particles were scratched from the filter.

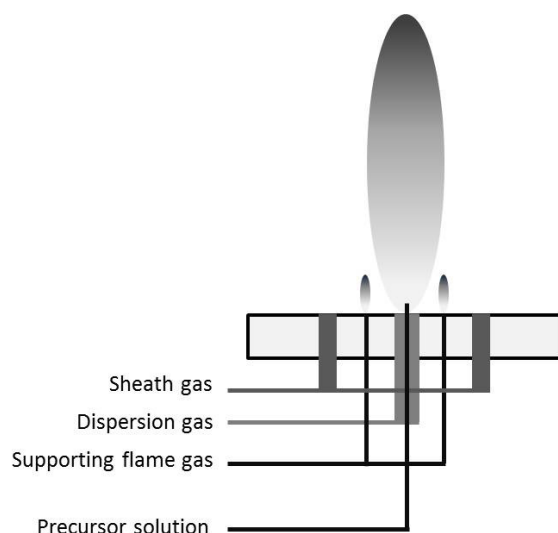


Figure 2.2.: Scheme of the flame generator.

2.1.2. ZSM-5 preparation

For synthesizing ZSM-5, sodium hydroxide and the template TPAOH (tetra-propylammonium hydroxide, Sigma-Aldrich, 1.0 M in water) were initially dissolved in water. TEOS (tetra-ethylorthosilicate, Sigma-Aldrich, > 99 %) as a silica source was added to the template solution under stirring.

After stirring the mixture for 2 hours, aluminum nitrate nona-hydrate (ChemPur, 98.5 %) was added under vigorous stirring. The final molar ratio was 1 TPAOH: 21 TEOS: 3 NaOH: 987 H₂O: 0.105 Al₂O₃ [98]. The solution was transferred to an autoclave vessel for hydrothermal treatment. The autoclave was put into a preheated oven at 170 °C and kept there for 24 hours. After the hydrothermal treatment, the obtained white powder was collected by filtration and washed with plenty of water to remove residual reagents. The powder was dried at 80 °C and calcined at 550 °C for 10 hours to remove the template. For the ion-exchange, the obtained Na-ZSM-5 was put into the 0.5 M aqueous NH₄Cl solution at 70 °C under stirring for 24 hours. By filtration and washing with water, excess ions were removed and H-ZSM-5 was finally obtained after calcination at 550 °C for 10 hours.

2.2. Characterization

X-ray diffraction (XRD) of the catalysts was performed with an X'Pert Pro MPD (PANalytical) instrument in order to understand the crystal structure of the synthesized catalysts. Diffraction data was obtained by exposing to Cu-K α X-ray radiation. The identification of peaks was done by the X'pert High Score software.

The reducibility of catalysts was investigated by temperature programmed reduction (TPR). In order to perform the TPR, the catalysts were pretreated in the same way as for reaction experiments; the primary catalyst particles were pelletized, pellets were grinded, and the grinded powders were sieved to obtain a particle size distribution of 50 - 100 μ m (agglomeration diameter). The sieved powder was then put in a quartz cell of a ChemBET TPR/TPD machine (Quantachrome). The catalyst was pretreated under a helium flow at 200 °C. Finally, the reducibility of the sample was investigated in a flow of a hydrogen/argon mixture (5 vol. % H₂) with a heating rate of 1 °C/min and a final ramp temperature of 400 °C.

At the same instrument, ammonia temperature programmed desorption (NH₃-TPD) was performed to know the acidity of the catalysts. Catalyst was equipped in a quartz cell and flushed with a helium flow at 450 °C to clean the catalyst surface. Then the sample was cooled down to 50 °C.

Ammonia gas was flowed for absorption on acid sites and then by helium gas flow physisorbed ammonia was removed. TPD was carried out heating up the sample with a heating rate of 15 °C/min up to 600 °C.

BET surface area and pore size distribution were measured in an Autosorb1 machine (Quantachrome). Before the measurement, the sample was degassed at 250 °C.

Particle morphology and size were investigated by transmission electron microscopy (TEM), and elemental analysis (EDX) was performed to identify elemental components.

A field emission electron probe microanalyzer (EPMA) JXA-8530F was used to investigate the catalyst layers, and elemental maps of the materials were detected by WDS (wavelength dispersive spectroscopy).

By N₂O-reactive frontal chromatography [116] the N₂O chemisorption capacity of CZA catalysts was determined. Approximately 100 mg of calcined sample (agglomerated to 50 - 100 μm in diameter) were placed in a fixed bed reactor. After in-situ reduction, the sample was cooled down to room temperature in the reducing gas, purged with He and then analyzed with a flow rate of 10 mL/min of a mixture of 1 % N₂O in He. The N₂O chemisorption capacity was determined from the mass spectrometer signal of the N₂ trace (m/z = 28). On the assumption that N₂O reacts only with the surface copper atoms and according to the stoichiometry of $\text{N}_2\text{O} + 2\text{Cu} \rightarrow \text{Cu}_2\text{O} + \text{N}_2$, the copper surface area was calculated.

2.3. Reactors

2.3.1. Tubular reactor

Common tubular reactors were used for activity testing of the prepared catalysts. They were made from stainless-steel tubes (Swagelok). Tubes with 8 or 6 mm inner diameter were regulated to 18 cm length, and the bottom of the tubes was plugged with a porous metal frit to prevent loss of catalyst particles; gases can pass through this (Figure 2.3). Catalyst powder was pelletized under a pressure of 39 kN. After that, The pellets were ground and sieved to 50-100 μm particle size. The prepared catalysts were filled

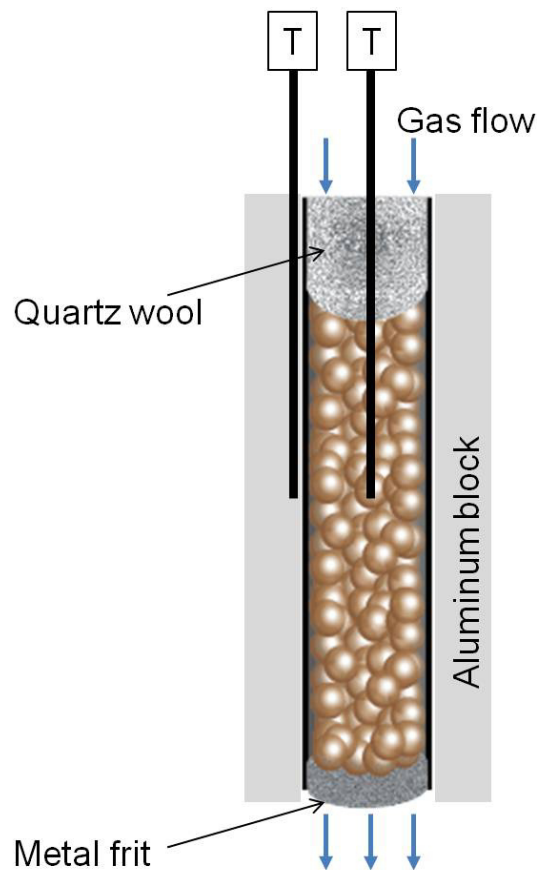


Figure 2.3.: Illustration of the tubular reactor. T: thermocouple.

into the tube and then quartz wool was inserted above the catalyst bed for packing. Two thermocouples were equipped in the middle of the catalyst bed and on the surface of the reactor body. The reactor was surrounded by a cylindrical aluminum block, above which electrical heating band and isolation band were wrapped sequentially. The measured temperature difference between the reactor wall and catalyst bed was ± 2 K. According to the former research, the simulated temperature profile along the catalyst bed showed a maximum difference of 5.6 K [45].

2.3.2. Berty-type reactor

A Berty-type reactor (Micro Berty Reactor, Parker Autoclave Engineers) was equipped in the test rig. A catalyst basket is placed there in the reactor body. Particle size of catalysts was regulated by the same method described

in the section 2.3.1. The prepared catalysts were placed in the basket, and firmly packed by using quartz wool and metal nets at the bottom and top of the basket. In the reactor gases are recycled with upward flow through the catalyst bed according to Figure 2.4. Gas circulation is driven by a top mounted vane type blower. Table A.1 provides specific details of the reactor. Two thermocouples are located in the basket and outside of the basket. The reactor body is wrapped with heating band and surrounded with an insulation jacket (Figure A.1).

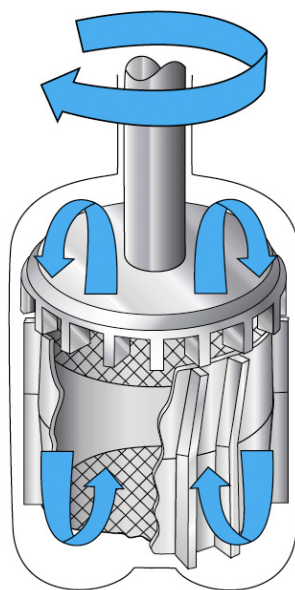


Figure 2.4.: Scheme of the Micro Berty Reactor [117].

2.3.3. Microchannel reactor

The microchannel reactor was made of a nickel-chromium-iron alloy (Material No. 1.4876). The reactor was designed to endure high pressure (max. 80 bar) and temperature (500 °C). The scheme of the reactor is shown in Figure 2.5. Item (5) is a stack of microchannel foils that are sandwiched by metal blocks (4, 7). The inlet and outlet of the microchannel foils are blocked with porous metal frits (6, 11). These foils are equipped in the reactor housing (1, 9). The reactor is sealed hermetically with graphite gaskets (novaphit[®], Frenzelit Werke GmbH) (3, 10). The reactor is closed with 28 screws, greased with Molykote[®] (Dow Corning) anti-seize paste, with 22

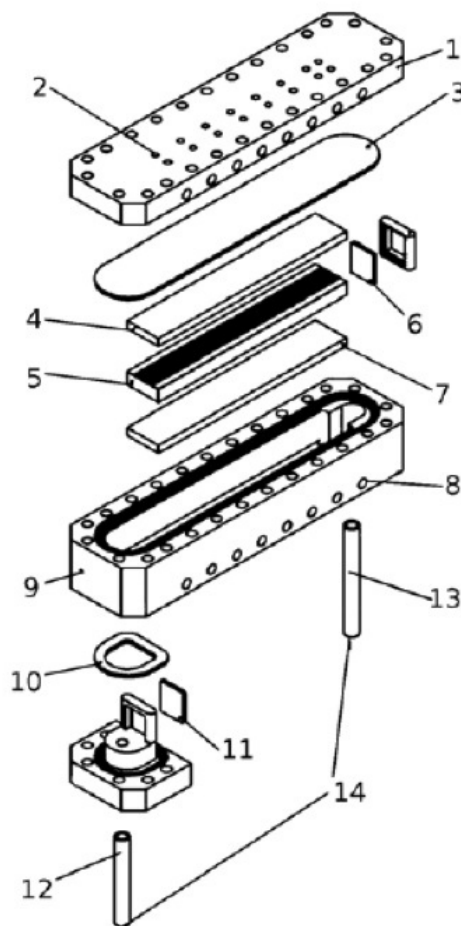


Figure 2.5.: Scheme of the microchannel reactor (for MF-1).

Nm torques. Thermocouples are located at (2) and electrical heating blocks at (8) with Ferrotherm 4 heat conductive paste (IBF) in order to enhance heat conduction. The electrical heating is operated with a power of 300 W for each unit, which allows to reach about 750 °C temperature. The reactor is connected to the test rig by VCR connectors (14). The reactor equipped in the test rig is insulated by PROMAFORM[®] insulation blocks.

Microchannel foils

For the direct DME synthesis reaction, rectangular microchannel foils (MF-1) were employed. The material of the foil was stainless steel (Material No. 1.4301). The microchannel foils were usually fabricated by micro milling. A microchannel foil contained 50 channels with a channel geometry of width x depth x length of 200 μm x 200 μm x 150 mm.

For the preliminary study on inkjet printing, both semicircular and

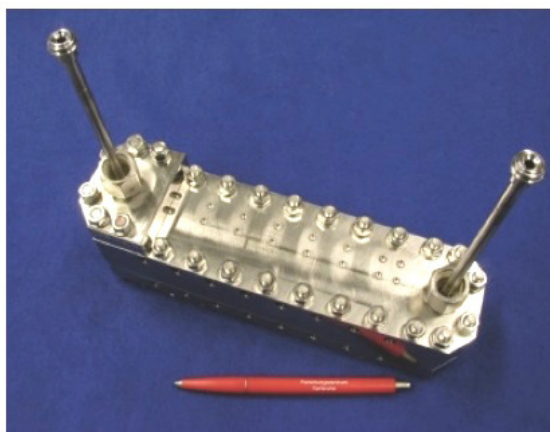
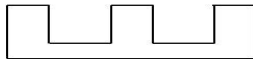

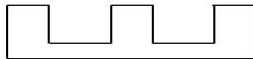


Figure 2.6.: Picture of the assembled microchannel reactor (for MF-1).

Table 2.1.: Details of microchannel foils.

| | MF-1 | MF-2 | MF-3 |
|--|---|--|---|
| Microchannel dimension (width x depth x length) | 200 μm x 200 μm x 150 mm | 300 μm x 90 μm x 50 mm | 200 μm x 200 μm x 80 mm |
| Number of microchannels in a foil | 50 | 105 | 100 |
| Material | stainless steel | stainless steel | Nicrofer [®] |
| Microchannel fabrication | micro milling | chemical etching | micro milling |
| Purpose | DME reaction | inkjet printing study | inkjet printing study |
| Cross section scheme |  |  |  |

rectangular microchannels were selected. Those differ also in terms of aspect ratio (depth versus width) and surface roughness. The semicircular microchannels (MF-2) were fabricated in stainless steel foils (Material No. 1.4301) (width x depth x length = 300 μm x 90 μm x 50 mm, 105 channels/foil) by wet chemical etching (Herz Ätztechnik, Germany). This method leads to a roughness level of the structured surface in the range of several microns (typically $> 5 \mu\text{m}$) resulting in a matt appearance. The rectangular microchannels were fabricated by micro milling with a hard metal tool in high temperature resistant Nicrofer[®] foils (MF-3) (Material No. 1.4876, Thyssen-Krupp VDM, Germany) in order to be used for high temperature reactions. They contained 100 channels/foil with a channel geometry of width x depth x length of 200 μm x 200 μm x 80 mm. The roughness level for micro milling is usually well below 1 μm giving the

structured surface a shiny appearance.

Before applying a catalyst coating, the foils were oxidized in air (MF-1 and MF-2 at 650 °C & MF-3 at 800 °C) to form an oxide layer on the surface for increased adhesion of the coating [118, 119].

2.4. Catalyst coating in microchannels

2.4.1. Inkjet printing

Catalyst ink formulation

Alumina ink

The alumina-based inks were prepared from a commercial stable aqueous colloidal nano-suspension of aluminum oxide having a particle size (d_{90}) of 100 nm (Alfa Aesar GmbH & Co KG), which exists at pH = 4 as pseudo-Boehmite ($\text{AlO}(\text{OH})$), CAS No. 1344-28-1). This colloidal suspension was either used directly as ink or further modified with ethylene glycol or polyethylene glycol-600. The density of the inks was measured by the pycnometer method. The surface tension of the inks was measured using the pendant drop technique with the help of a liquid dosing nozzle, an optical cell (both from SITEC AG, Maur/Zurich) and a CCD camera (Sony AVC-D5CE). The viscosity of the inks was measured at a shear rate of 100 s^{-1} , using a Thermo Scientific HAAKE rheometer having a plate and cone arrangement.

Cu/ZnO/ Al_2O_3 ink

5 g of FSP-CZA powder was suspended in 44.5 g of water with 0.5 g of Dolapix CE 64 (carbonic acid based polyelectrolyte; Zschimer & Schwarz GmbH) as a dispersing agent [5]. This suspension was loaded in the vessel of a ball milling machine (MicroCer[®] NETZSCH) in order to break down agglomerated nanoparticles. 170 g of yttria-stabilized zirconia (YSZ) balls with a diameter of 200 μm was added in the vessel. The milling process was carried out with 1000 rpm. Particle size of the milled FSP-CZA suspension was measured by using a dynamic light scattering equipment

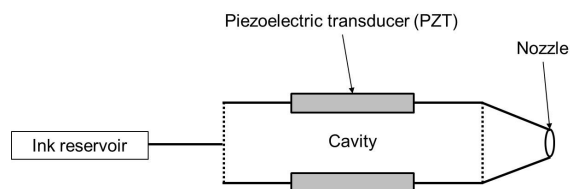


Figure 2.7.: Schematic diagram of the piezoelectric print head.

(Beckman Coulter, Delsa™ Nano C Particle Analyzer). The milled FSP-CZA suspension was further formulated with ethylene glycol to adjust it to a printable Z number (the inverse of the Ohnesorge number Oh). Surface tension, viscosity and density were measured in the same manner as for the alumina ink preparation.

ZSM-5 ink

ZSM-5 ink was prepared according to the same method than the Cu/ZnO/Al₂O₃ ink. However, Dolapix CE 64 was not applied since after ball milling ZSM-5 was quite stable in water without it.

Catalyst coating in microchannel via inkjet printing

Operation of the printer

Inkjet printing was conducted with a commercial printer (microdrop Technology GmbH). The inkjet printer was equipped with a print head (MD-K-140) containing a 100 μm diameter nozzle. The ink reservoir (5 ml) supplies the ink to the print head. The print head was filled with the ink from the ink reservoir, and a negative holding pressure (about 10 mbar) was applied to keep the ink in the print head cavity. A schematic diagram of a piezoelectric print head used in DOD inkjet printing is shown in Figure 2.7. The print head cavity is surrounded by a piezoelectric transducer. In the present work, two different types of pulse modes, single and bi-polar pulse, were applied to generate the droplets. In the single pulse mode, only positive voltages were used. In the bi-polar pulse mode, both a positive and a negative voltage were applied sequentially. Positive voltage ejects the ink fluid, and then the negative voltage breaks off the drop and withdraws the rest of the ejected fluid.

Drying of the printed foils

After printing of the alumina ink the foils were dried at 70 °C in an oven for 24 hours and subsequently calcined in air at 550 °C (MF-2) or 750 °C (MF-3) for 6 hours. The temperature ramp was set to 2 °C/min. At 380 °C the temperature was held for 6 hours.

An immediate drying technique at high temperature was applied for printed MF-1 foils. FSP-CZA printed foils were dried at 450 °C for 2 minutes. ZSM-5 printed foils were dried at 30 °C for 10 minutes and then at 450 °C for 2 minutes.

2.4.2. Catalyst coating with micropipette

Catalyst coating in microchannels by using a micropipette was performed as a reference coating to compare to the inkjet printed layers. As a simple catalyst coating method in microchannels it uses catalyst dispersions in water [120–123]. Here, already prepared catalyst inks were used. The catalyst ink was put in microchannels by using a micropipette. Then the filled microchannel foil was treated for drying in the same manner as the inkjet printed foils. This process was repeated until obtaining the desired catalyst mass.

2.4.3. Double-layer catalyst coating for direct DME synthesis

For the double-layer printing, the FSP-CZA ink and ZSM-5 ink were used. At the optimized printing condition, the FSP-CZA ink was printed on MF-1 foils until the microchannel bottom and walls were totally wet with the ink. Total 675000 ink droplets were deposited in one microchannel foil at one printing sequence. Afterwards, the printed microchannel plate was dried at the above mentioned conditions. This printing process was repeated until the desired mass of the catalyst was obtained. On the printed and dried FSP-CZA catalyst layers, the ZSM-5 ink was printed. ZSM-5 printing was executed until the FSP-CZA catalyst layer was sufficiently wet. The same number of ink droplets with the FSP-CZA printing was needed for ZSM-5 printing at one sequence. The drying of the printed microchannel foils was

performed as mentioned above. The mass of the printed catalyst layer was determined by the weight difference before and after printing. The printed layers were observed by EPMA and an optical microscope.

2.5. Reaction experiments and analysis

2.5.1. Test rig design

The reaction study was carried out in an existing test rig designed for the DME synthesis reaction. The process flow diagram of the test rig is shown in Figure 2.8. All the gas lines in the test rig are made of stainless steel. It can endure the high pressure and temperature conditions of DME synthesis, ≤ 50 bar and ≤ 350 °C. Gas flow rates are controlled by gas mass flow controllers (MFCs). Those were calibrated according to the used gases. Two regulation valves for pressure control are used, one for low (0-16 bar) and the other for high (up to 50 bar) pressure. Between the MFCs and the pressure control valves, the gas line was divided into three branches, one bypass line and two reactor lines. Hence, two reactors can be equipped.

Methanol feeding was established by using a microchannel evaporating device. Methanol was filled in a storage vessel and flowed to the evaporator by a liquid mass flow controller (LFC). The liquid methanol stream at the evaporator was brought in contact with nitrogen gas. Methanol was dispersed into droplets and vaporized by heating. The heating temperature was set to the temperature required to achieve the desired partial pressure. When the evaporator was unavailable, an alternative methanol feed method, N₂ gas blowing through a methanol reservoir, was used. The temperature of the methanol reservoir was kept at room temperature (about 23 °C). This method provided a low methanol concentration in the feed gas mixture.

The MFCs, LFC, pressure valves and electrical heating were controlled by a LabVIEW program. The automation of these controls as well as the data acquisition was also established by this program.

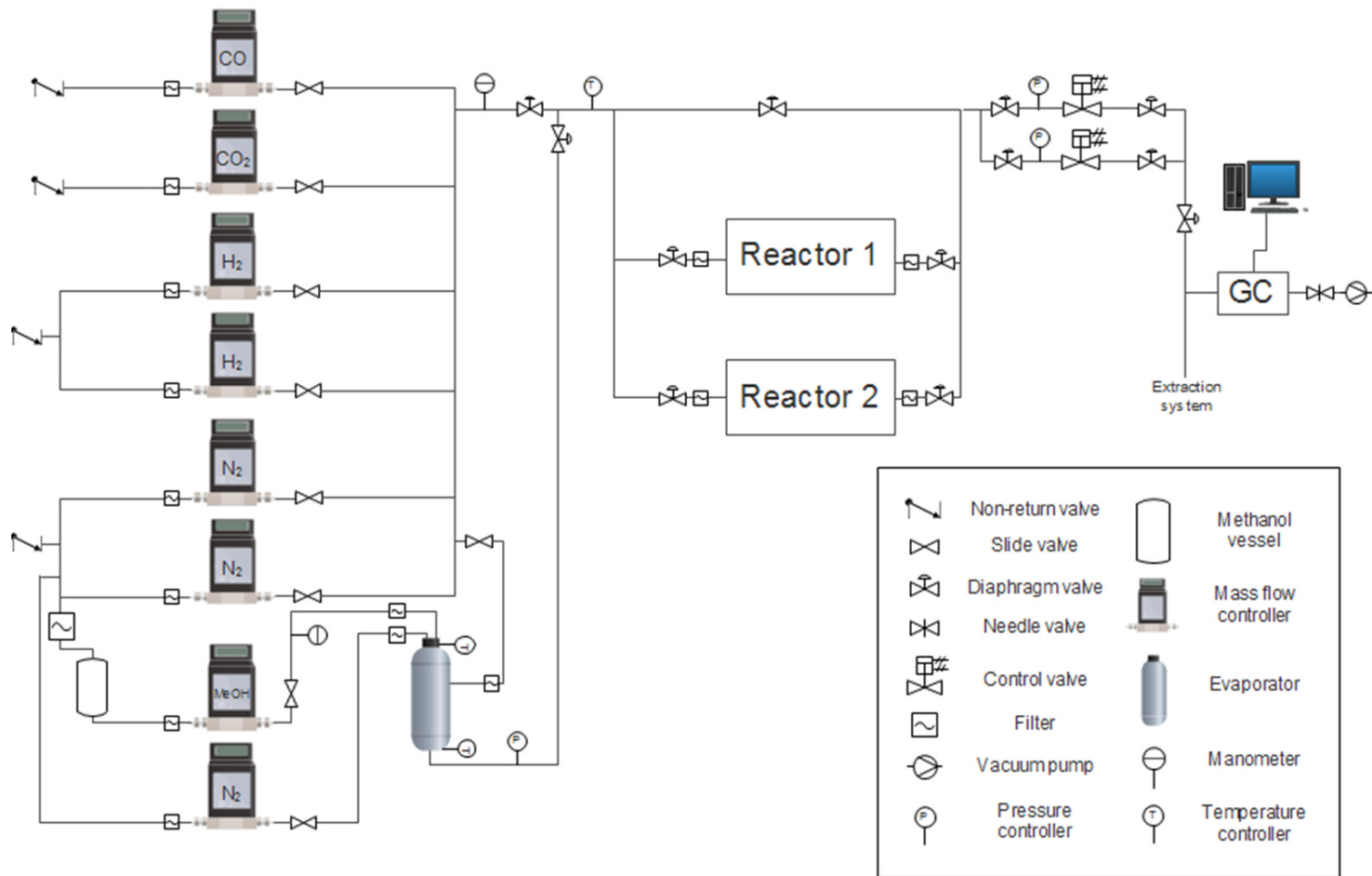


Figure 2.8.: Process flow diagram of the test rig.

2.5.2. Gas analysis by gas chromatography (GC)

The reactants and products were analyzed with a gas chromatograph 7890A (Agilent Technologies) equipped with a methanation unit, a thermal conductivity detector (TCD) and a flame ionization detector (FID). Two columns, HP-Plot Q (30 m x 0.530 mm x 40.00 μm) and HP-Molesieve (5 m x 0.530 mm x 25.00 μm), were used to separate all gas components. Figure 2.9 shows the schematic diagram of the GC setup.

In order to make an efficient separation of gas components, a GC method with a temperature program of an oven where the columns are placed and six port valve operation was established. A HP-Molesieve column was used for CO, N₂ and H₂ separation, but this is not suitable for large molecules (CO₂, MeOH, DME and hydrocarbons). After CO, N₂ and H₂ were trapped in the HP-Molesieve column, the rest of components were separated by a HP-Plot Q column with an appropriate temperature program. After that, the trapped gases were separated by the HP-Molesieve column and then went to the detectors. The GC temperature and valve action procedure is indicated in Table A.2. For the gaseous components, CO, CO₂, N₂, H₂ and hydrocarbons (methane up to hexane), a GC calibration was performed by using standard gas mixtures with defined volume concentrations. Methanol was calibrated by using a vaporization and reflux system. Methanol was filled in a vessel having a reflux condenser. By heating and injection of N₂ carrier gas, vaporized methanol was injected to the GC. The partial pressure of methanol was calculated by the Antoine-equation (2.1): p and T are the vapor pressure and temperature respectively, and A , B and C are component specific constants.

$$\ln(p) = A + \frac{B}{C + T} \quad (2.1)$$

A carbon balance over the reactions was calculated with the assumption of ideal gas behavior according to the following equation:

$$\left(\frac{\dot{N}}{\dot{N}_0} \right)_C = \left(\frac{\dot{V}}{\dot{V}_0} \right)_C = \frac{y_{CO,0} + y_{CO_2,0}}{\sum y_i \nu_i} \quad (2.2)$$

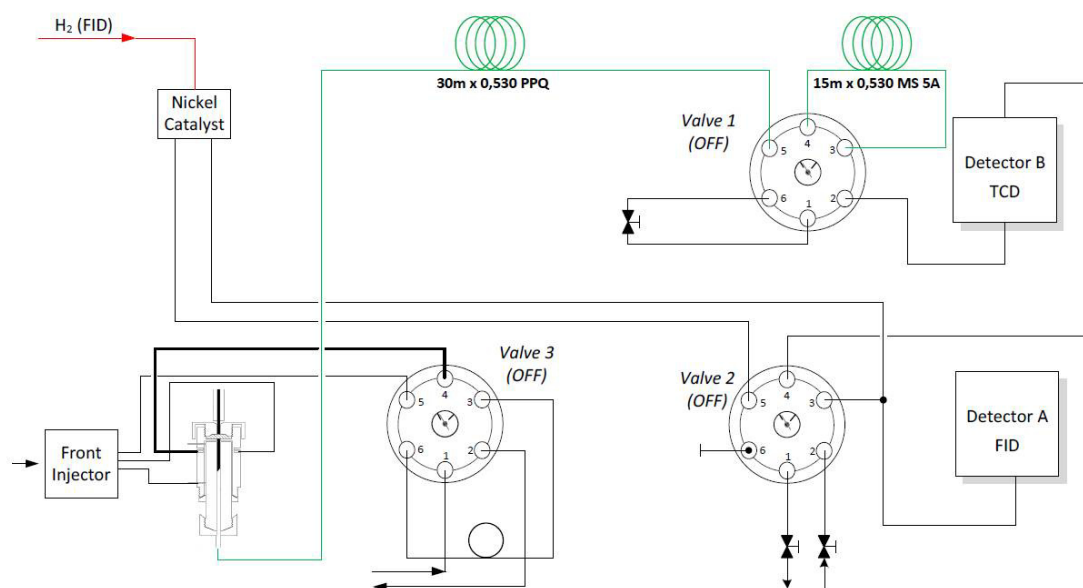


Figure 2.9.: Schematic diagram of the GC.

ν_i is the number of carbon atoms of the component i . The deviation of the carbon balance was maintained below 5 %.

2.5.3. Catalyst activation

Since metallic copper is the active phase, reduction of CZA was carried out before all reactions. Equation 2.3 shows conversion of copper oxide to metallic copper. The reduction program is shown in Table 2.2. The reduction was started with a 3 vol. % H_2 in N_2 mixture, and the catalyst was heated up to 240 °C. The temperature ramp in this step was very low. After that, the gas was changed to pure hydrogen and temperature was elaborated up to 250 °C. This reduction process has been recommended in order to obtain sound catalytic activity, although at the laboratory scale the effect of the reduction process on activity is minimal [45].

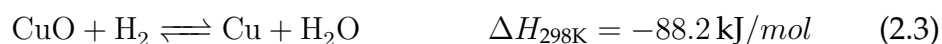


Table 2.2.: Reduction program for the CZA catalyst [45].

| Gas mixture | Starting temperature [°C] | Target temperature [°C] | Temperature ramp [°C/min] | Holding time [hour] |
|--|---------------------------|-------------------------|---------------------------|---------------------|
| 3 vol.% H ₂ /N ₂ | 100 | 150 | 1.92 | 0 |
| | 150 | 200 | 12 | 0 |
| | 200 | 240 | 30 | 0 |
| | 240 | 240 | 0 | 8 |
| H ₂ | 240 | 250 | 6 | 0 |
| | 250 | 250 | 0 | 5 |

2.5.4. Reaction performance

The volume contraction by the change of the total number of moles after the reaction was calculated from an internal standard, nitrogen. Since the molar flow of nitrogen at inlet and outlet is constant, the volume contraction is expressed in the following equations with the assumption of ideal gas behavior.

$$\dot{N}_{N_2,0} = \dot{N}_{N_2} \quad (2.4)$$

$$\dot{V}_0 \cdot y_{N_2,0} = \dot{V} \cdot y_{N_2} \quad (2.5)$$

$$F = \left(\frac{\dot{V}}{\dot{V}_0} \right) = \frac{y_{N_2,0}}{y_{N_2}} \quad (2.6)$$

With the volume contraction factor (F), CO and methanol conversion were calculated by the following equations, respectively.

$$X_{CO} = \frac{(\dot{N}_{CO,0} - \dot{N}_{CO})}{\dot{N}_{CO,0}} = 1 - \frac{\dot{N}}{\dot{N}_0} \frac{y_{CO}}{y_{CO,0}} = \left[1 - F \frac{y_{CO}}{y_{CO,0}} \right] \cdot 100 [\%] \quad (2.7)$$

$$X_{MeOH} = \frac{(\dot{N}_{MeOH,0} - \dot{N}_{MeOH})}{\dot{N}_{MeOH,0}} = \left[1 - F \frac{y_{MeOH}}{y_{MeOH,0}} \right] \cdot 100 [\%] \quad (2.8)$$

The selectivities of the products and DME productivity are defined in the following equation.

$$S_i = \frac{\nu_i}{\nu_{CO}} \cdot \frac{F y_i - y_{i,0}}{y_{CO,0} - F y_{CO}} \cdot 100 [\%] \quad (2.9)$$

$$P_{DME} = \frac{\dot{m}_{DME}}{m_{cat}} \quad (2.10)$$

\dot{m}_{DME} is the mass flow of DME.

Direct DME synthesis was carried out with the reactants, H₂, CO and CO₂. N₂ was used as an internal standard. The volumetric percentages of the gases were H₂ 57.6 %, CO 28.8 %, CO₂ 3.6 % and N₂ 10 %.

3. Investigation of Cu/ZnO/Al₂O₃ (CZA) via flame spray pyrolysis (FSP)

3.1. Flame technique for catalyst production

Flame synthesis of fine particles was initially developed for production of ceramics. However, there is a possibility for using similar technology for large scale production of catalyst nanoparticles [124, 125]. FSP is one possibility within the flame synthesis of fine particles. It uses a liquid, flammable solvent and typically also flammable metal precursors. The metal precursors need to be dissolved and the mixture is sprayed along with air or oxygen into a flame. The metal precursors are decomposed in the high temperature flame (up to 2000 °C) into gaseous metal ions. They subsequently nucleate to form particles. By coalescence and aggregation, the particles grow up in size. The process conditions such as the flame temperature and the residence time in the flame determine the particle size and crystal structure [112]. This technique has been used for single metal oxides and frequently also for multi-component metal oxide particles [112].

In FSP, parameters for flame generation are greatly influencing particle formation e.g. size, structure, oxidation state and homogeneity. Mädler et al. [113] synthesized silica nanoparticles (primary size 8 - 40 nm) by FSP. Hexamethyldisiloxane (HDMSO) was used as a silica source and was mixed with ethanol as a fuel. O₂ or Air was used as a dispersion gas. Figure 3.1 shows images of the flame. O₂ dispersion gas generated a brighter flame. The temperature was approximately 1000 K higher with oxygen than with air. The flame height was decreased and the temperature

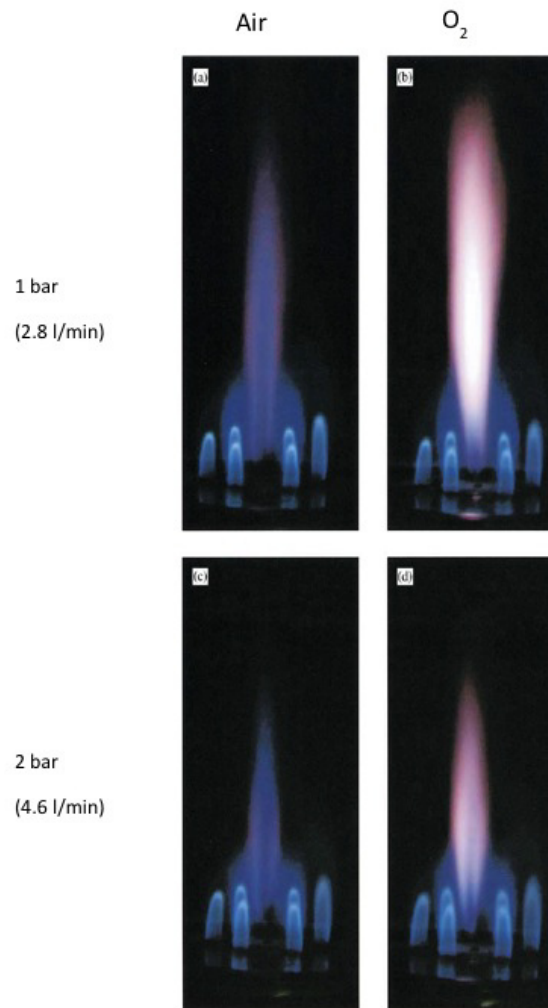


Figure 3.1.: Long exposure time (1/60 s) images of luminescence of turbulent HMDSO/ethanol spray flame [113].

was increased by increasing the dispersion gas flow to a certain level. The flow rate of the dispersion gas predominantly affected the particle size and surface area. In Figure 3.2, the specific surface area of the synthesized silica particles was increased at first by increasing the flow rate to a certain value (2.4 L/min for air and 3.0 L/min for O₂). However, a further increase of the flow rate decreased the specific surface area. Generally, droplet evaporation, precursor release and particle formation took place at short times while increasing the flow rate. Increasing the flow rates induces a decrease of the residence time of the particles in the flame and avoids sintering of the particles. Beyond the maximum of the surface area value, the flame height was reduced considerably with increasing the flow rate. The position of the maximum against the flow rate can be changed when

other fuels are used (Figure 3.3). Methanol as a fuel also gave a maximum at a flow rate similar to ethanol. Iso-octane fuel showed only a declining tendency in the same flow range of the oxidant, which shows that the particle formation and behavior in the flame is also determined by the heating value, combustion rate and evaporation rate.

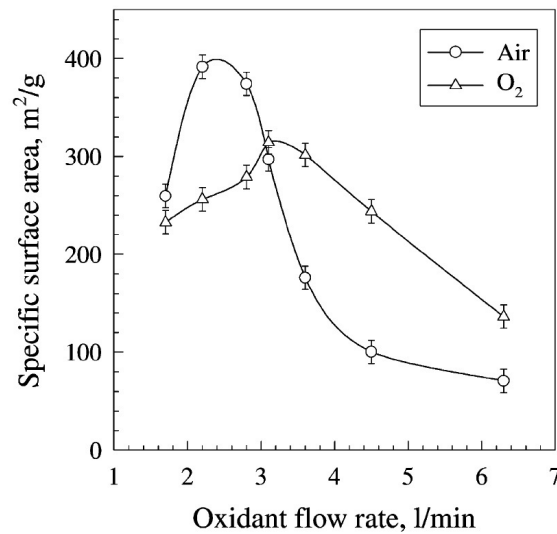


Figure 3.2.: Specific surface area as a function of dispersion gas flow rate [113].

Mädler et al. [113] investigated the effect of sheath gas. O₂ sheath gas accelerates the combustion, which increases the rate of silica particle formation and growth. When the spray flame is diluted by O₂, less particle collisions are induced. It leads to a reduction of particle growth, which decreases the particle diameter. The precursor feed rate was also investigated with O₂ dispersion gas. At low precursor feed rate, agglomerated small primary particles (dozens of nanometers) were produced. At higher precursor feed rates, agglomeration of small particles was not severe, but larger particles (hundreds of nanometers) co-existed.

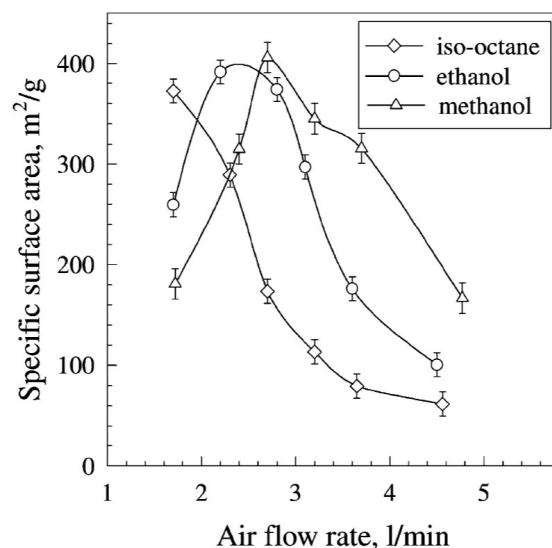


Figure 3.3.: Specific surface area of FSP made silica nanoparticles as a function of dispersion air flow rate with different solvents [113].

3.2. FSP synthesis of Cu/ZnO/Al₂O₃

3.2.1. State-of-the-art of FSP-CZA

A few research groups have reported CZA particle synthesis via flame synthesis. Jensen et al. reported CZA preparation by flame combustion synthesis using vapor phase metal precursors (aerosol technique); these catalysts have been well characterized and were applied in methanol synthesis [126]. Huber et al. and Ahmad et al. showed catalytic applications of the flame synthesized CZA with liquid phase metal precursors in the water-gas shift reaction and DME synthesis, respectively [127, 128]. The latter demonstrated that a FSP synthesized CZA can be comparable to a commercial CZA catalyst. Kam et al. demonstrated advantages by doping with another element, La, on the Cu/ZnO by FSP [129]. They could enhance the activity of the catalyst by the FSP technique. According to all former reports, FSP could provide similar, or even better, physicochemical and catalytic properties of copper catalysts compared to the conventional catalysts.

In this work, two kinds of metal precursors, metal nitrate and organometallic, were compared. Characterizations to know material and catalytic properties were performed and catalytic activity test for

direct DME synthesis was carried out with H-ZSM-5 in a tubular fixed-bed reactor. Finally the most active FSP-CZA was used for inkjet printing and the double-layer catalyst.

3.2.2. Characterization of FSP-CZA

The flames generated by both precursor types are shown in Figure 3.4. Each precursor type gave different types of flames. The greenish color of the flames of both precursors might be due to the copper. Injection of the organometallic type gave more intense and vigorous flames compared to the nitrate type. The DMF/xylene mixture has a lower heating value of 31.1 MJ/L. Ethanol possesses a lower heating value of 23.5 MJ/L. Organometallic precursors possess a higher combustion enthalpy than nitrate precursors. Thus, the same volumetric injection of the organometallic precursor solution provides more energy for the flame. This leads to a difference in heat release between these precursors which could be one of the reasons for the difference in flame height. From the pictures it can be known that the organometallic precursor solution generated a taller flame. The change of the metal ratio in the same precursor type did not give a visible difference in flame color and height. Thus, it can be concluded that the different solvent heating value was the main reason for the difference in the flame height.

TEM analyses were used to investigate the FSP particle arrangement and size. The TEM images of CZA catalysts prepared from both precursor types are shown in Figure 3.5 (by example of a same Cu/Zn molar ratio). Both precursors gave nanoparticles, and most of them were in the nanometer size range (Figure 3.5 (c) and (d)). However, also some relatively large spherical particles were found (Figure 3.5 (a) and (b)). The EDX analysis revealed that the small particles consisted of copper and zinc oxides without any aluminum whereas the big particles consisted almost exclusively of aluminum oxide. The small particles located on the big particles were also copper and zinc species without aluminum. The former studies about the flame synthesis process of CZA [126] indicated that zinc aluminate and copper aluminate spinel are formed at high temperature (>1300 °C). Formation of copper or zinc oxides is favorable at lower temperature. In

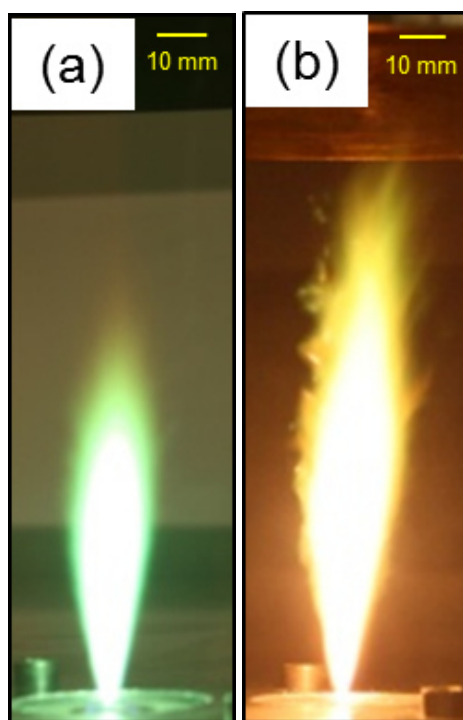


Figure 3.4.: Flame pictures of FSP for catalysts A631 (a) and B631 (b).

the present work, spinel formation could not fully be excluded, but it was assumed that aluminate or aluminum oxide forms prior to the zinc and copper species and aggregates to bigger clusters. As the aluminum fraction in the precursor mixtures was the smallest amongst the metals, only a few of the big clusters could be found in TEM images. Most of copper and zinc oxide clusters exist separately from the big clusters.

The particle size was measured piecewise from TEM images. The identified copper and zinc oxide particles from both the nitrate type and the organometallic type systems were nearly the same in size. The particle sintering rate was reported to be proportional to the residence time [124]. The mean particle sizes of both A631 and B631 were 8.91 and 9.55 nm respectively. As shown in Figure 3.6, the size distributions of both catalysts were quite similar. From this observation, it can be known that the effect of the precursor selection on size is minor at least in this case even if different metal precursors and solvents were used. The residence time is one of the greatest effects on the particle size, so that the residence time difference of both precursor systems apparently was not significant.

The crystal structure of the catalysts was investigated by XRD. The XRD patterns of samples A631 and B631 are shown in Figure 3.7. Both samples

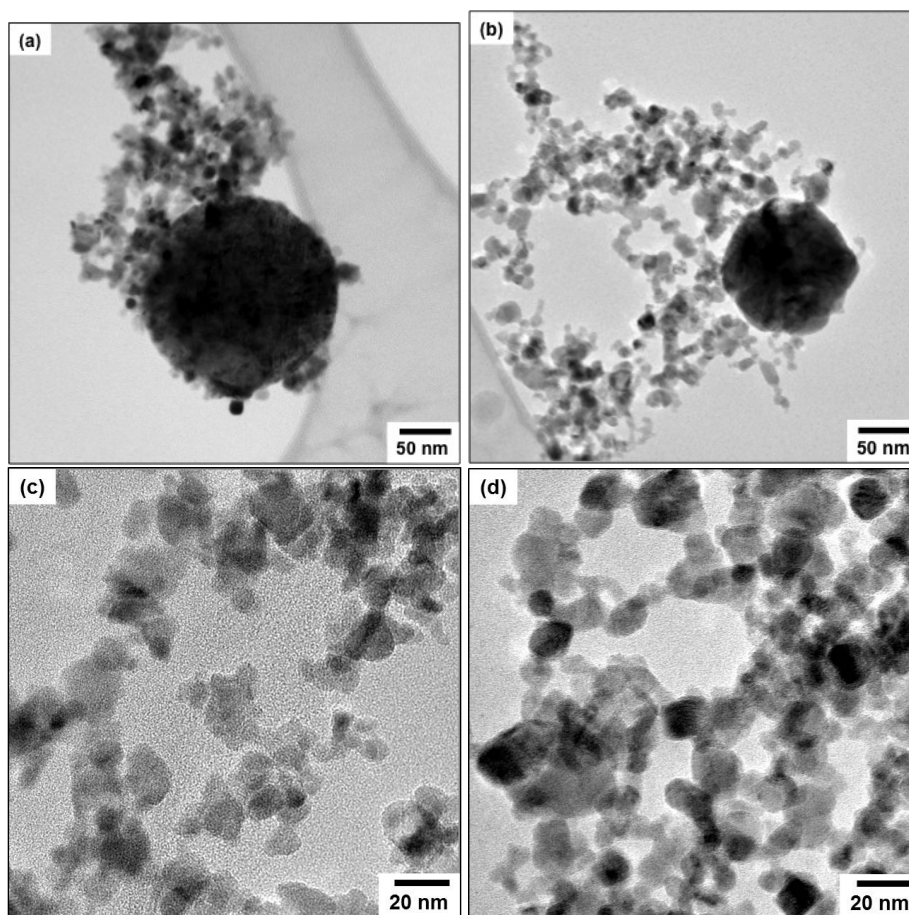


Figure 3.5.: TEM images of FSP synthesized CZA: A631 (a, c), B631 (b, d).

possess diffraction patterns of copper oxide, zinc oxide and aluminum oxide. According to the previous reports [126, 128], CZA synthesized by the flame technique gives broadened peaks by the dispersion of the different crystal phases. Only copper oxide was identified in their reports and other oxides could not be observed due to lower contents than copper. In this work, however, all metal oxides were well identified by XRD analysis, which means that each metal oxide is at least partially crystalline. The peaks for Al_2O_3 were found, although the aluminum content was low and the molar ratio was only 10 %. The A631 showed more intense Al_2O_3 peaks than the B631 in spite of equal molar fraction of aluminum in the precursor mixture. The peaks for zinc oxide were also more intense for the A631. As the intensity difference correlates to surface morphology and structure of metal oxides [130], the nanostructure of the copper surface and its interaction with other metal oxides are related to the activity in

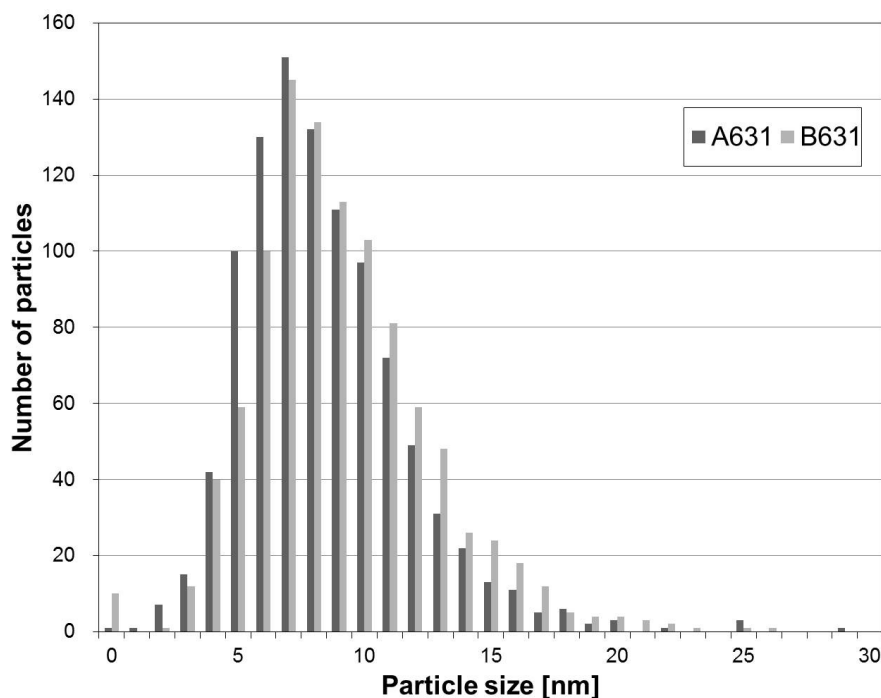


Figure 3.6.: Particle size distribution of A631 and B631.

reactions. These two catalysts should possess different catalytic activity.

The effect of the copper and zinc ratio on the crystal structure was also investigated for each precursor type via XRD. As shown in Figure 3.8, an increase of the Cu/Zn ratio generally led to more intense peaks assigned to CuO and to a reduction of the peaks for ZnO. Interestingly, the peak for CuO at 39.0 (2 theta degree) was reduced for the nitrate type catalysts by increasing the Cu/Zn ratio. The peaks for Al₂O₃ were more intense while increasing the Cu/Zn ratio for both precursor types. This was more noticeable in Type A than in Type B. Although the amount of aluminum compound was kept equal in all samples, the crystal shape and morphology was affected by the composition of the other elements. As mentioned in a former report, this can also influence the catalytic activity [131].

For methanol synthesis and consequently for direct DME synthesis, copper oxide should be easily reducible to metallic copper. Hence, the reducibility of the catalyst was investigated by TPR. Figure 3.9 shows TPR spectra of all catalysts. For all the compositions, Type A catalysts showed lower reduction temperatures than Type B catalysts. Some shoulder peaks were eventually assigned to the reduction process of Cu²⁺ to Cu¹⁺ and then to Cu⁰ in the main peak. All catalysts except for the B721 possessed a maximum in the reduction temperature well below 300 °C; above this

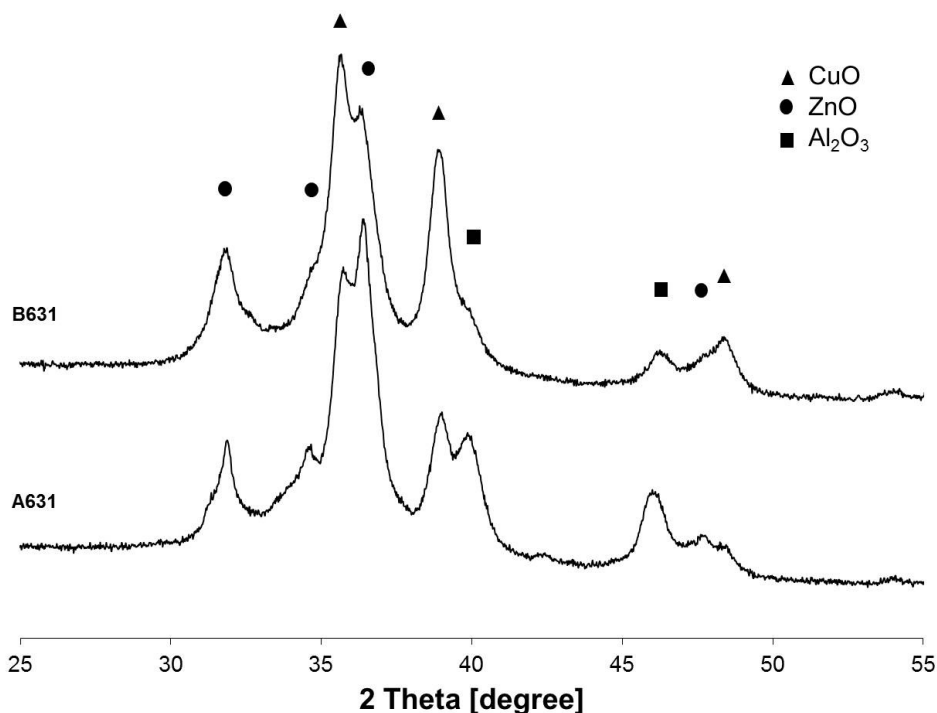


Figure 3.7.: XRD patterns of A631 and B631.

temperature, copper sintering would occur quite fast if such temperature is required for reduction. The maximum reduction temperature was increased by the increase of the copper content. It is assumed that higher copper loading produces a bulk-like copper oxide. Therefore, the dispersion of copper oxide is lower as the reduction temperature is higher [132].

Further investigation of the BET surface area and exposed copper surface area was performed. The measured values for Type A and B catalysts are shown in Table 3.1. The catalyst prepared from organometallic precursors has a little higher BET surface area. As mentioned above, the selection of precursor did not affect the particle size distribution much. However, the particle morphology of multi-metallic particles was influenced by the precursor. It has been reported in literature that nitrate metal precursors and ethanol are not favorable; due to the presence of water in the flame, the particle homogeneity and particle size distribution may be poor [124]. This is in line with our observation that Type A has a lower BET surface area than Type B. When the Cu/Zn ratio was altered, the surface area was also changed. The highest value was observed with Cu/Zn/Al=6/3/1 for both precursor types.

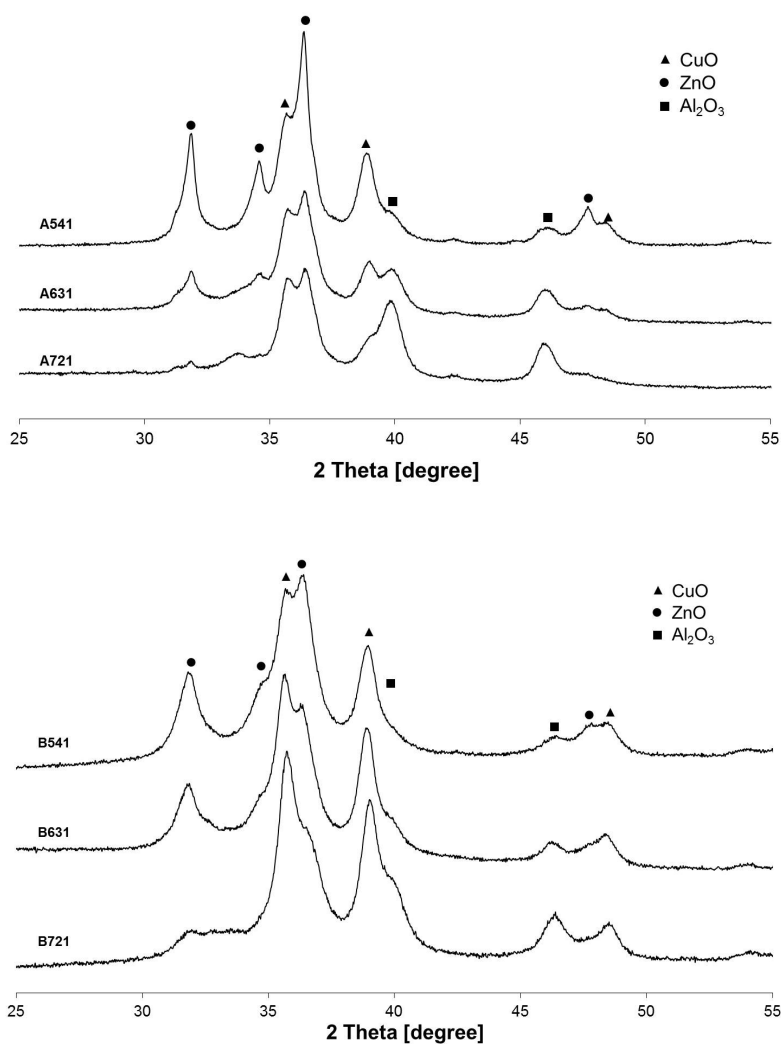


Figure 3.8.: XRD patterns of Type A and B catalysts.

The copper surface area was measured by N_2O -adsorption analysis. As given in Table 3.1, the result of the copper surface area was opposite to the BET surface area. Type B catalysts surpassed Type A in the BET surface area, but not in the copper surface area. The A631 catalyst showed the highest copper surface area. It therefore should have the most exposed copper sites among all samples. Although both A631 and B631 were synthesized with the same starting Cu/Zn ratio, by the selection of precursor the amount of copper sites was found to be much different. Therefore, a higher catalytic activity with the A631 would be expected. This is in line with the results of the TPR measurement, where lower reduction temperatures were observed for the nitrate type catalysts, and lower reduction temperatures are usually indicating a higher dispersion of the copper species. However,

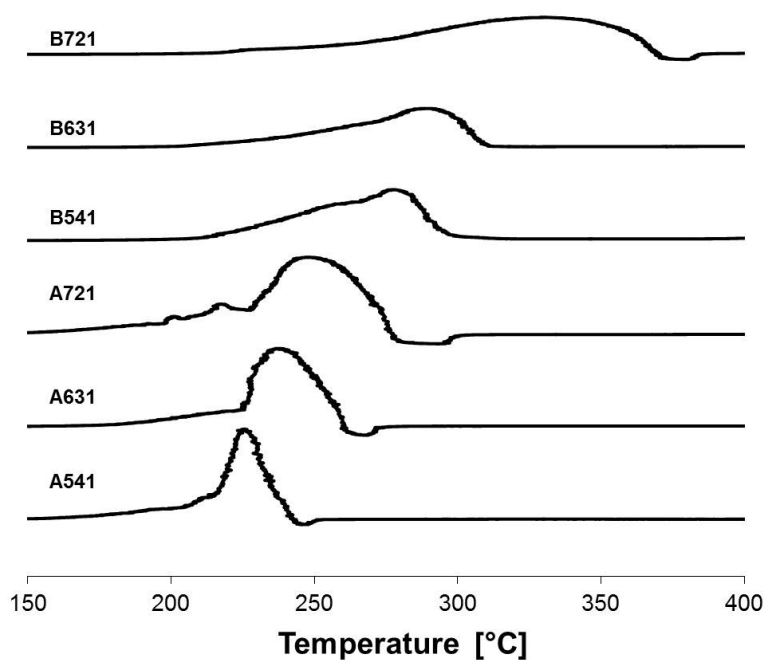


Figure 3.9.: TPR spectra of Type A and B catalysts.

low reduction temperature is not unequivocally associated with a high copper surface area [133]. Within the same precursor type, the reduction temperature and the copper surface area did not show a linear correlation. For sake of completeness, the determined copper amount of the A631 and B631 from TPR is also given in Table 3.1. The mass fraction of copper was relatively close to the nominal copper-to-metals ratio in the precursor solutions.

3.2.3. Catalytic activity of FSP-CZA for direct DME synthesis

The activity of each type of catalyst for direct DME synthesis was tested in a tubular fixed-bed reactor. CZA and H-ZSM-5 catalysts were mechanically mixed in 1:1 weight ratio, and then packed in the reactor. As predicted from the characterization results, the nitrate and organometallic type revealed different activity in direct DME synthesis. As shown in Figure 3.10, the CO conversion increased for both catalysts with the reaction temperature. The A631 sample exhibited superior catalytic activity and the

Table 3.1.: Surface area, copper surface area and CuO content.

| | BET surface area (m ² /g _{cat}) | Cu surface area (m ² /g _{cat}) ¹⁾ | N ₂ O chemisorption capacity (μmol/g _{cat}) | CuO (wt. %) ²⁾ |
|------|---|--|--|------------------------------|
| A541 | 33.39 | 13.8 | 170 | - |
| A631 | 41.04 | 18.6 | 226 | 63.4 |
| A721 | 39.95 | 16.4 | 200 | - |
| B541 | 54.00 | 8.6 | 104 | - |
| B631 | 63.70 | 10.6 | 130 | 55.1 |
| B721 | 60.77 | 7.0 | 86 | - |

¹⁾Determined by N₂O-RFC. ²⁾Amount of CuO was measured based on TPR before the N₂O chemisorption analysis.

Table 3.2.: Testing condition of direct DME synthesis in a tubular reactor.

| | |
|--|------------------|
| Temperature | 215 - 260 °C |
| Pressure | 10 - 40 bar |
| Mass of catalyst | 6 g |
| Mass ratio of CZA and H-ZSM-5 | 1:1 |
| Particle size of catalyst | 50 - 100 μm |
| H ₂ :CO:CO ₂ :N ₂ | 57.6:28.8:3.6:10 |

CO conversion could reach the thermodynamic equilibrium at 260 °C for the contact time applied. One commercial CZA catalyst was tested as a reference. At the same reaction conditions the commercial catalyst gave higher CO conversion than the FSP synthesized catalysts. At 245 °C, the CO conversion reached the equilibrium. The B631 showed lower activity with the pre-defined reduction protocol. According to the TPR study, the reduction temperature of the B631 was between 250 and 300 °C. Hence, an additional reaction experiment was carried out after extending the temperature ramp of the in-situ reduction to the highest temperature of 300 °C for the catalyst, but no obvious change in the conversion or selectivity was observed. Figure 3.11 shows the DME productivity of three catalysts. The commercial catalyst gave the highest DME productivity at all examined temperatures than the FSP catalysts. A631 is comparable only at 260 °C. The B631 system intrinsically has a lower activity. Catalysts having a higher copper surface area showed higher activity than the one having higher total surface area and lower copper surface area. Hence, the control of the surface area of the active copper sites is very crucial.

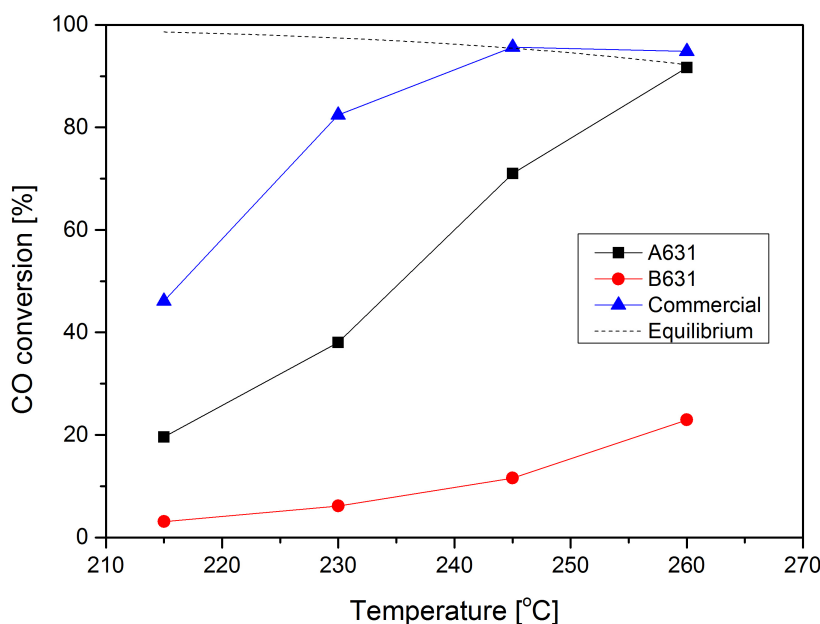


Figure 3.10.: CO conversion of the commercial CZA catalyst, A631 and B631 as a function of temperature. GHSV = 900 Nml/g_{cat}h, p = 40 bar.

Table 3.3.: Selectivity of the commercial CZA catalyst, A631 and B631. GHSV = 900 Nml/g_{cat}h, p = 40 bar, T = 260 °C. unit = %.

| | DME | Methanol | CO ₂ | CH ₄ | C2+ |
|------------|-------|----------|-----------------|-----------------|------|
| A631 | 66.28 | 3.92 | 27.27 | 1.37 | 1.16 |
| B631 | 62.86 | - | 30.12 | 4.01 | 3.01 |
| Commercial | 69.36 | 3.19 | 26.50 | 0.78 | 0.17 |

There was no big difference in selectivity between the A631 and B631 catalysts as shown in Figure 3.3. The catalyst mixture with the A631 sample produced a little more DME and less side products: CO₂, CH₄ and other hydrocarbons. Methanol was detected along with the A631 and commercial catalysts. The CZA and H-ZSM-5 particles were mechanically mixed so that some methanol produced could pass the H-ZSM-5 in case of high activity of the CZA catalyst. In the case of the B631 catalyst, the overall activity was so low that methanol could be completely converted over the H-ZSM-5 to DME and sequential side products. As shown in Figure 3.12, the selectivity for DME increased with the reaction temperature, and the CO₂ selectivity was influenced only slightly by the reaction temperature. The DME selectivity is strongly related to the activity of the dehydration

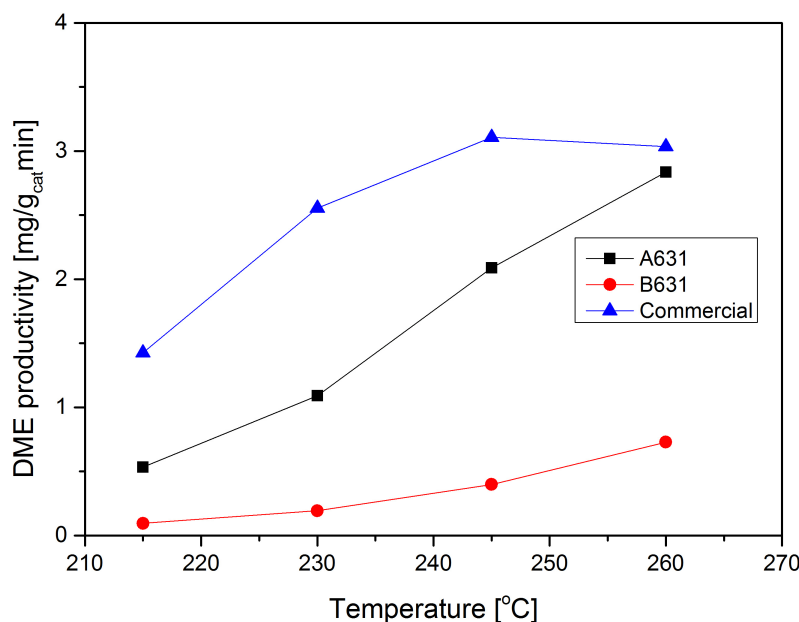


Figure 3.11.: DME productivity of the commercial CZA catalyst, A631 and B631 as a function of temperature. GHSV = 900 Nml/g_{cat}h, p = 40 bar.

catalyst [134]. The produced methanol can mainly be converted to DME since the H-ZSM-5 can give high conversion of methanol to DME at similar reaction conditions [135].

The influence of the Cu/Zn ratio was investigated on Type A catalysts. Table 3.4 shows the activity of the three different Type A catalysts. The A631 sample was the most active one for converting CO. The A541 sample had the lowest copper reduction temperature, but the catalytic activity was lower than for the A631 sample. The A721 sample having a higher copper content does not provide high activity. CO conversion and DME yield of the A721 sample were lower than for the A541 sample. The selectivity, however, was not influenced much by the Cu/Zn ratio. It can be concluded that copper and zinc have its optimal ratio in the A631 sample. This agreed well with the former research that copper cannot be solely responsible for high activity [136]. Zinc oxides should interact with copper defect sites as well as there should be a high enough accessible copper surface area. In addition, the activity is not exclusively related to the reduction temperature for FSP catalysts.

The A631 catalyst was further investigated. Figure 3.13 shows the

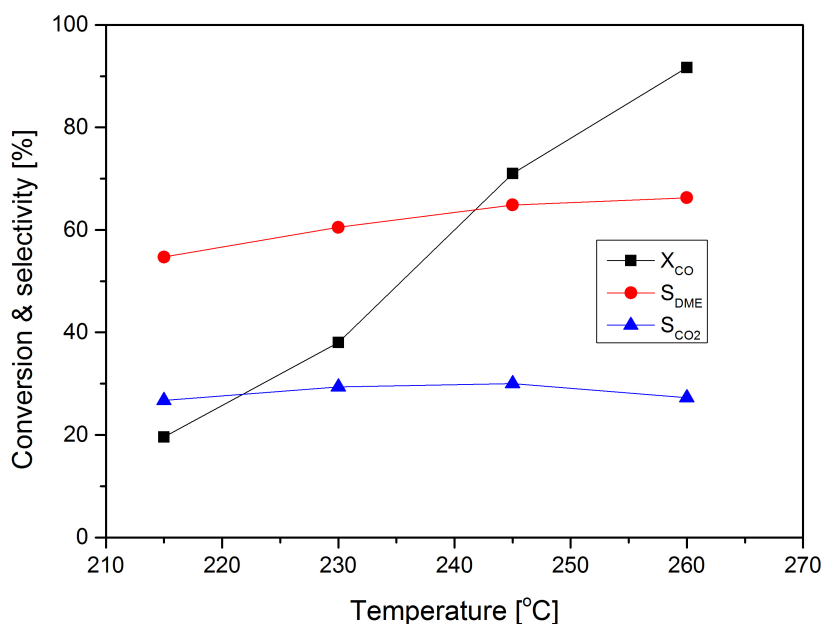


Figure 3.12.: CO conversion and DME and CO₂ selectivity for the A631 catalyst as a function of temperature. GHSV = 900 Nml/g_{cat}h, p = 40 bar.

Table 3.4.: CO conversion, DME and CO₂ selectivity and DME yield of Type A catalysts. GHSV = 900 Nml/g_{cat}h, p = 40 bar, T = 260 °C. unit = %.

| | X _{CO} | S _{DME} | S _{CO₂} | Y _{DME} |
|------|-----------------|------------------|-----------------------------|------------------|
| A541 | 86.73 | 64.07 | 28.22 | 55.56 |
| A631 | 91.70 | 66.28 | 27.27 | 60.78 |
| A721 | 78.05 | 65.17 | 29.26 | 50.87 |

conversion and selectivity with various pressures and GHSVs. Decreasing of the reaction pressure reduced the conversion of CO (Figure 3.13 (a)). This is due to the fact that the thermodynamic equilibrium conversion of methanol synthesis and also that of direct DME synthesis are lower at reduced pressure [35]. The DME selectivity was not influenced by the reaction pressure except for 215 °C. At low temperature and low pressure condition, due to the low activity of the catalysts the measurement uncertainty becomes large. Therefore, the deviation of the DME selectivity at 215 °C (Figure 3.13 (b)) cannot be explained straightforward. As shown in Figure 3.13 (c), the CO conversion decreases with an increase of the GHSV. The DME selectivity remained constant. Methanol synthesis was restricted

by pressure and GHSV, while methanol dehydration was not. Therefore, the development of methanol synthesis catalysts is crucial in order to increase the overall DME yield in direct DME synthesis.

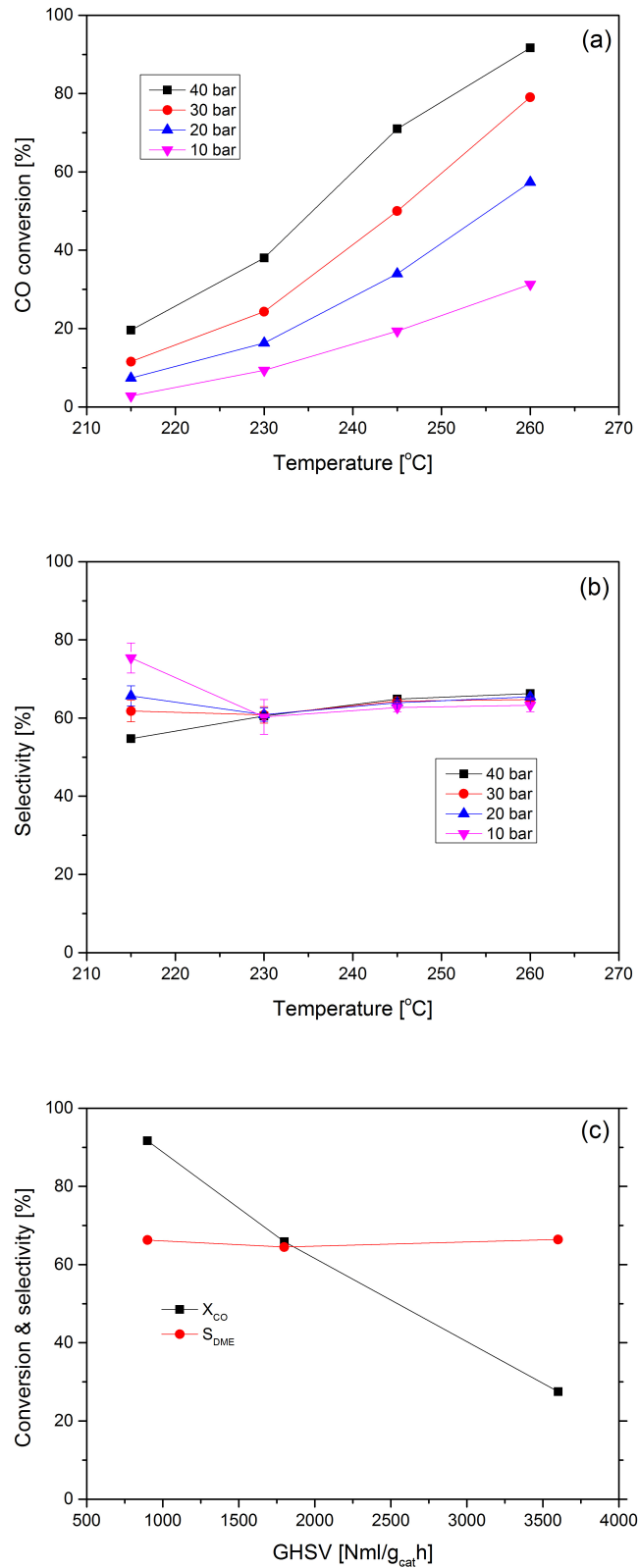


Figure 3.13.: Pressure effect in direct DME synthesis over A631: CO conversion (a) and DME selectivity (b) as a function of temperature; GHSV = 900 Nml/g_{cat}h, T = 260 °C. CO conversion and DME selectivity of A631 as a function of GHSV (c); p = 40 bar, T = 260 °C.

4. Inkjet printing for catalyst coating into microchannels

4.1. Introduction of inkjet printing

4.1.1. Principle and application of inkjet printing technology

Inkjet printing principle

Inkjet printing technology is well known in the paper printing industry. Since 1970s, the inkjet industry has been growing markedly. Inkjet printing has been demonstrated as a powerful tool in manufacturing chemical sensors, refractive optical components, electrodes, thin film transistors, solar devices, microspheres, microstructured pillars, printed batteries, catalyst coatings on fuel cell membranes, biomaterials, etc. [137–145].

In general, there are two different mechanisms to generate droplets with an inkjet printer: continuous drop formation and drop-on-demand (DOD) [146]. In the former, a liquid stream is continuously pumped through a small orifice and small droplets are generated by Rayleigh instability. The latter generates droplets by pressure waves in a liquid-filled cavity using a piezo-electric transducer. The DOD printing technique is preferred for the deposition of ceramic or metallic particle suspensions acting as support or catalytically active materials [146]. The drop-on-demand (DOD) inkjet printing offers some advantages compared to other printing technologies. DOD inkjet printing does not need any additional conducting materials or volatile organics. Excellent reproducibility and repeatability are possible with DOD inkjet printers with little maintenance.

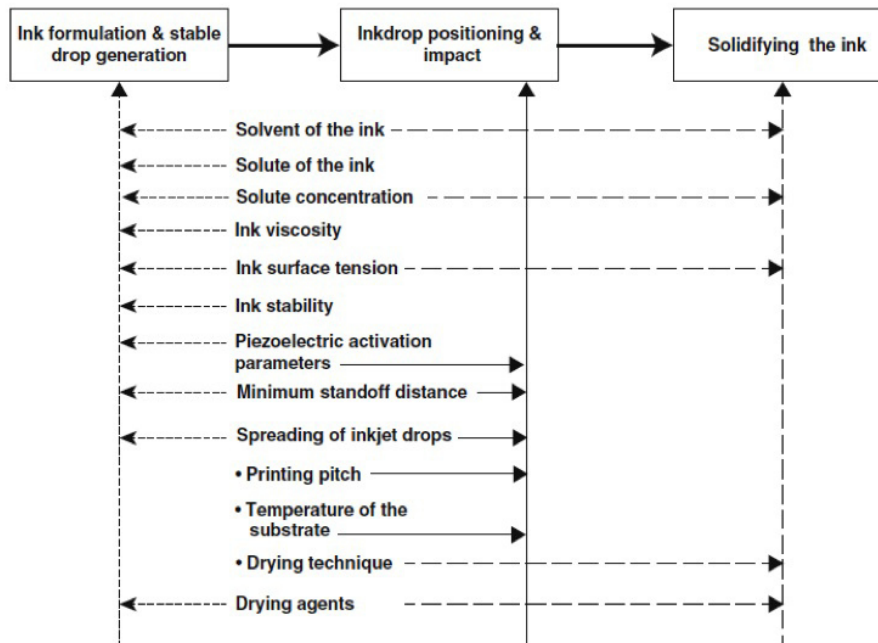


Figure 4.1.: Parameters for inkjet printing processes.

The inkjet printing is a three-step process: (a) ink formulation and drop generation, (b) drop positioning and impact, (c) solidification. As shown in Figure 4.1, there are several parameters that have a different extent of influences on these three steps in the printing. A number of review articles have been appearing in the literature with improved understanding toward the significance of these parameters in DOD inkjet printing. De Gans et al. [147] reviewed the state of the art in polymer printing with specific emphasis on polymer structures, solvents and concentrations. Derby [148, 149] reviewed the significance of fluid properties and target-ink interactions on the stability of the printing process and on the resolution of the printing. Nevertheless, all three steps of the inkjet printing are not yet fully understood, and more systematic studies on inkjet printing process parameters are required.

Ink viscosity and surface tension have to be considered for successful printing. The physical properties of the ink such as density, surface tension, and viscosity do have a large influence on the drop formation mechanism in DOD printers and the resulting inkjet drop characteristics such as drop size, drop ejection velocity, satellite drop formation and drop relaxation time. The printability of an ink is connected with the Z number, which is a dimensionless grouping of fluid properties equivalent to the inverse of the

Ohnesorge number Oh [149]:

$$Z = \frac{1}{Oh} = \frac{Re}{\sqrt{We}} = \frac{(\gamma\rho\alpha)^{1/2}}{\eta} \quad (4.1)$$

In this equation η , γ , ρ and α are the dynamic viscosity, surface tension, density and nozzle diameter. The Z number describes the ratio of the surface forces to the inertial forces during drop formation in DOD print heads. If the Z value is too low or too high, satellite droplets may be generated during printing operation. This shows that the ink formulation is a crucial step for the successful application of inkjet printing. The region $4 < Z < 14$ has been considered normally as the printable range for various systems [150]. Nevertheless, there is a large discrepancy in the literature regarding the optimum range. Kuscer et al. [151] observed stable drop formation for Z values in between 4 and 9. Perelaer et al. [152] generated stable drops of organic solvents having Z values ranging from 8 to 63.

Several authors have reported a decrease in drop diameter with decrease in the Z value of the ink [144, 150, 153]. In contrast, Kuscer et al. [151] has reported no influence of the Z number on drop size. Reis et al. [153] observed a plateau in drop size at higher Z numbers. Differences in printer nozzle diameters, nozzle internal design and the applied voltage wave form for the activating piezoelectric material might be the reasons for unusual observations from distinct groups.

A piezoelectric print head is composed of a capillary glass tube surrounded by a piezoelectric material. One end of the glass tube in a cylindrical shape is a nozzle and the other end is connected to an ink reservoir (Figure 2.7). The operation of the print head can be explained in a wave propagation model [154]. In this theory, the nozzle side is considered as close-end. The other side is considered as open-end. Figure 4.2 shows a schematic illustration of the wave propagation. Initial expansion giving negative pressure takes place by application of voltage. The pressure is distributed to each end where it is reflected. When the applied voltage is relieved, the tube is contracted and a new positive pressure is generated. By the interference of the pressure waves, the right propagating pressure is amplified. The ink can be ejected if the pressure is sufficiently high. If there is no more voltage applied, the next high positive pressure wave reaches the nozzle after $4 l/c$ time, that is the meniscus oscillation period in this model.

Lin et al. [155] developed this model for double voltage pulse system. The second voltage makes necking and breaking of the ejected drop. Reis et al. [153] extended this model for optimizing piezoelectric activation parameters for ceramic inks. However, to exploit this theory properly, the structure of the print head should be known, e.g., length of tube, location and area of the piezoelectric material, extent of the contraction and expansion of the tube, etc.

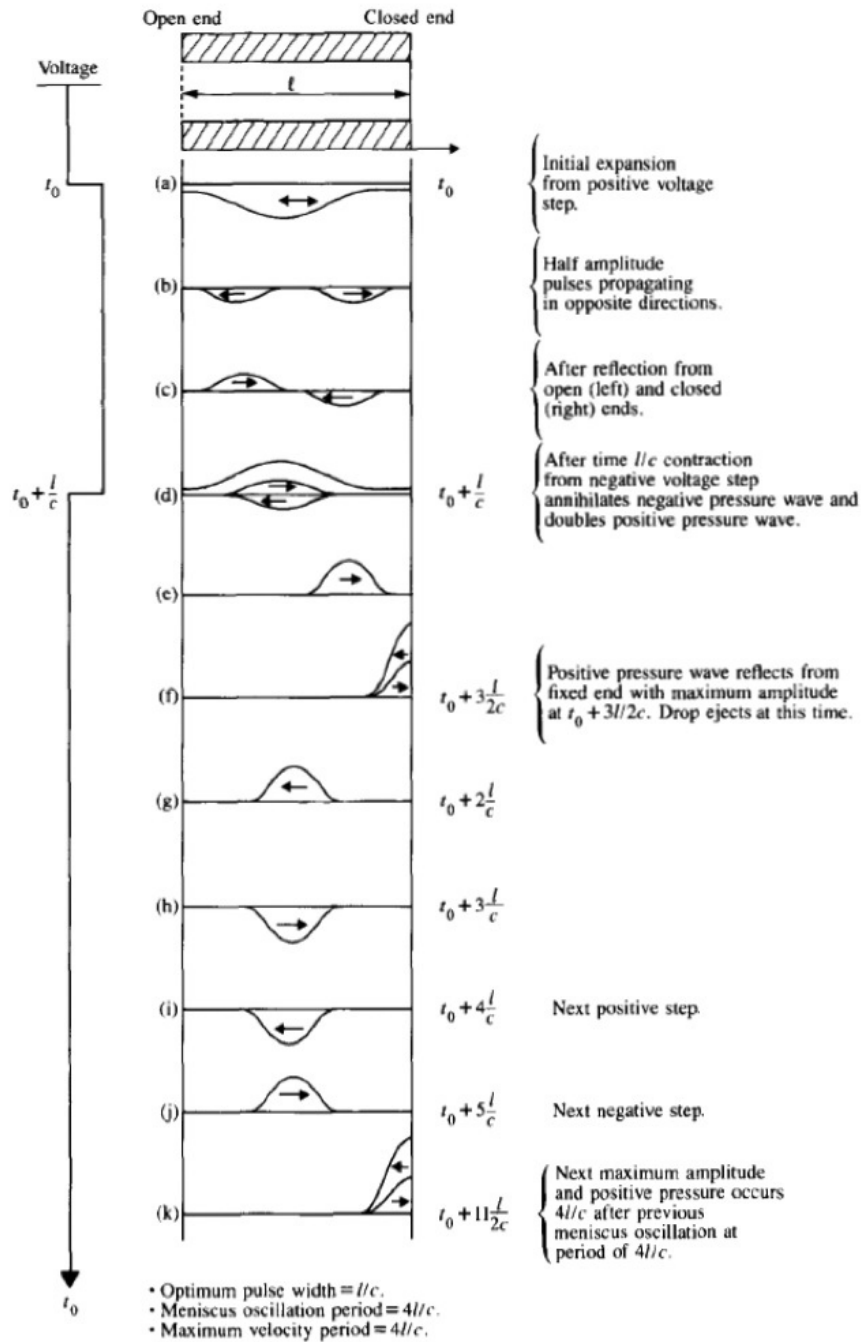


Figure 4.2.: Scheme of wave propagation and reflection in an open-closed squeeze tube [154]. c is the sound speed.

4.1.2. Particle printing

One of the most critical parts in inkjet printing is the preparation of the ink. There are several issues that must be considered to make a good ink.

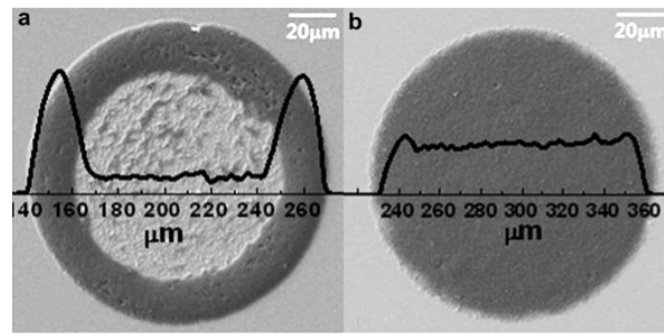


Figure 4.3.: SEM images and surface profiles of Al_2O_3 ink droplets. (a) water single-solvent ink and (b) DMF + water co-solvent ink [158].

At first the solid particles must be well dispersed in a solvent to form a stable suspension. Sedimentation of the particles leads to nonuniform particle concentration of ejected ink drops as well as clogging of the nozzle. In the formulation of an ink, rheology is an overriding consideration. The viscosity of particle suspensions is depending on the shear rate. The volume fraction, size, shape and inter-particle forces of the solid particles are influencing the viscosity. The ink in the printer nozzle is subjected to very high shear rates up to 10^6 s^{-1} , which influences the ink ejection mechanism. Moreover, as solid particles may be hard materials, a print head can be worn quickly. The nozzle size can be enlarged and the lifetime of the print head reduced. Another issue is the first drop problem, that is the clogging of the nozzle by dried ink [156]. Therefore, low volatile solvents are required and an addition of humectants retarding the solvent evaporation at the nozzle tip by facilitating rapid rehydration of the ink [157].

Recently, many researches about the formation of stable nanoparticle inks have been published. The suggested methods include reducing the particle size [158], modification of the solvent system [143, 158], introducing stabilizing agents such as surfactants or polymers [159, 160]. In a single solvent system, a deposited droplet on a substrate shows accumulation of particles at the circumference of the droplet (coffee ring effect) because solvent evaporation takes place along the contact line of the droplet, which induces the outward flow (Figure 4.3 (a)). One solution to avoid the coffee ring effect is a co-solvent system [158]. Figure 4.3 (b) shows an ink droplet formed from DMF and water as a co-solvent. DMF has a higher boiling point and lowers the surface tension compared to water. Water evaporates

at the edge of the droplet, which induces a surface tension gradient. Both inward and outward flows compensate and produce homogeneously dispersed particles. The inward flow caused by the surface tension gradient is called Marangoni flow. The Marangoni flow can be defined with the Marangoni number, M :

$$M = \frac{\Delta\gamma L}{\eta D_{AB}} \quad (4.2)$$

Where $\Delta\gamma$ is the surface tension difference between the center and the edge of the drop, L is the radius of the ink droplet on the substrate, η is the viscosity of the co-solvent, and D_{AB} is the diffusion coefficient of solvent A (drying agent, DMF) in solvent B (main solvent, water).

4.1.3. Heterogeneous catalyst ink

In addition to the condition for particle inks, more circumspect formulation is necessary for heterogeneous catalyst inks. Solvents and additives for the formulation should not be harmful to the catalysts. There must not be any undesired chemical reaction between particles and solvents or additives. The pH value of the ink also must be considered. Some catalysts are sensitive to a change of the pH value; active sites or the catalyst particle can be destroyed.

There are some researches about the application of inkjet printing in heterogeneous catalysis, e.g. photocatalysis and fuel cell technology. Taylor et al. demonstrated layer by layer deposition of platinum catalysts for fuel cell applications [138]. On the confined area, the control of the catalyst loading in the film is a big advantage of inkjet printing. In this report, the feasibility of this fine loading control was demonstrated. The performance of the printed catalyst was comparable to the conventional coating method. Arin et al. printed a transparent 85 nm thin TiO_2 film on a glass substrate by inkjet printing and tested its photocatalytic activity [161]. The inkjet printing technique helped to control the layer thickness, which is relevant to the photocatalytic activity. TiO_2 layer formation by inkjet printing is cheap and fast and produces less waste material.

In order to avoid this difficulty of particle printing, the printing using

catalyst precursor solutions was suggested [162]. In there, aqueous solutions were used instead of colloidal solutions to avoid particle sedimentation. In this case, the solubility of metal salts should be high enough to prevent deposition of particles by precipitation before sticking on the heated substrate. While the solvent evaporates, metal will form oxide hydrates and oxides on the substrate (Figure 4.4). Fousseret et al. [163] reported inkjet printing of a mesoporous silica sol. A poloxamer was used as a structure directing agent, and the formation of a mesoporous structure was driven by an evaporation-induced self-assembly (EISA) method. The precursor sol was inkjet-dropped on the silicon surface, and by the EISA method mesoporous silica microdots were formed. These techniques can be applied in more or less simple catalyst synthesis.

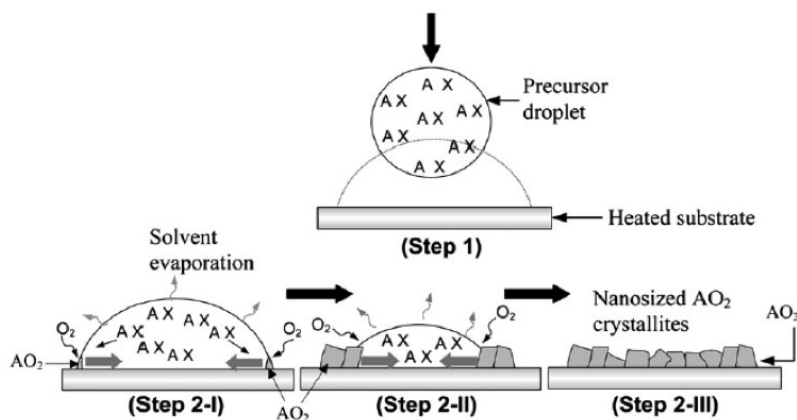


Figure 4.4.: Schematic illustration of film formation by inkjet printing of metal surface [162].

Inkjet printing for catalysis is still not fully explored in spite of large potential benefits such as catalyst structure and thin film formation. Especially, as microstructured reactors need a fine control of catalyst coating, inkjet printing is promising.

4.1.4. Inkjet printing in microstructured plates

Inkjet printing in microchannels is different from printing on a planar surface due to the geometrical character. There are a few studies on inkjet printing in microstructures. In the microstructure, side walls exist and are wetted as well by cases. Liou et al. [164] studied the inkjet printing

of polymers in a rectangular microcavity having different surface wetting properties at side walls and bottom. They reported that the microcavity would be uniformly filled when an ink drop deposits with a Weber number from 19.9 to 31.2 and at a ratio of the contact angle of the ink with the side wall to the bottom from 0.34 to 0.77. Chen et al. [165] uniformly deposited polymers in n-sided regular polygonal cavities. In case of microchannels, the shape can influence the formation of the printed material [166]. Also the drying process in a microstructured geometry would be different. The microcavity does not have an open side, but the microchannel can have it. Wallenstein and Russel [167] proposed a model for the drying process in a rectangular microchannel. According to this model, the evaporation of the solvent creates a flow of particles in the microchannels toward the drying plane, and the convection-diffusion process of the solvent at the open end of the microchannel determines instabilities such as cracks or delamination. Han and Lin [32] reported that when a colloidal suspension dries in a confined zone, the evaporation rate is controlled and the temperature gradient in the liquid is minimized, which can suppress the Marangoni flow and natural convection. However, the Marangoni flow and natural convection generate a coffee ring effect in the case of drying of microdrops on planar surfaces. On the other hand, Loffelmann et al. [166] reported a decrease in the evaporation rate in V-shaped microchannels, which results in an improved particle packing in microchannels. These findings contradict the observation of Shin et al. [168] who found that good particle packing was obtained by rapid solvent evaporation on planar surfaces. In order to understand the drying process on the thin film shape in the microchannels, it is necessary to explore the significance of the coffee ring effect for the formulated inks.

4.2. Investigation of the printer operating parameters

The list of inks used for this work having different physical properties characterized by different Z values are summarized in Table 4.1. The ink without co-solvent (Ink-1 & Ink-2) blocked the printer nozzle within a short

Table 4.1.: Composition and physical properties of the formulated inks at room temperature.

| Inks | Aluminum oxide (wt. %) | Ethylene glycol (wt. %) | Polyethylene glycol-600 (wt. %) | Density (kg/m ³) | Surface tension (10 ⁻³ N/m) | Dynamic viscosity (mPas)* | Z | Drop generation |
|-------|------------------------|-------------------------|---------------------------------|------------------------------|--|---------------------------|------|-----------------|
| Ink-1 | 20 | - | - | 1189 | 42.2 | 6.2 | 11.5 | Non-stable drop |
| Ink-2 | 10 | - | - | 1083 | 47.2 | 4.1 | 17.6 | Non-stable drop |
| Ink-3 | 5 | 33 | - | 1088 | 53.0 | 2.4 | 30.5 | Stable drop |
| Ink-4 | 5 | 75 | - | 1140 | 48.0 | 9.6 | 7.7 | Stable drop |
| Ink-5 | 5 | 50 | 25 | 1141 | 41.0 | 22.9 | 3.5 | Stable drop |
| Ink-6 | 10 | 50 | - | 1175 | 44.6 | 7.4 | 9.8 | Stable drop |
| Ink-7 | 10 | 25 | 25 | 1180 | 40.0 | 15.6 | 4.4 | Stable drop |
| Ink-8 | 15 | - | 25 | 1095 | 48.1 | 12.2 | 5.9 | Stable drop |

*measured at a shear rate of 100 s⁻¹

period of operation. The other inks (from Ink-3 to Ink-8) were formulated with co-solvents as humectants and viscosity modifiers which can lead to stable drop formation. Therefore, stable drops were generated with these inks, and their Z numbers range from 3.5 to 30.5. The Z numbers of Ink-1 and Ink-2 are also in this range, but the drop generation with them was not stable. This corresponds to the literature survey in section 4.1.1. that each research report provides a divergent optimum Z number range. The acoustic phenomena in DOD printer heads (Figure 4.2) take place with very high shear rate ($\sim 10^6 \text{ sec}^{-1}$). This is able to increase coagulation of the particles in the ink [157, 169]. In order to determine more reliable Z values, the ink's rheological behavior should be observed at high shear rate [170].

The physical properties and the values for the dimensionless Z number of the formulated inks are given in Table 4.1. The viscosity of the ceramic particle suspension inks decreases generally with increasing shear rate and becomes constant for shear rates above 100 s⁻¹ [171]. Therefore, the viscosity at 100 s⁻¹ was used for calculating the Z number. A 10 wt. % alumina suspension (Ink-2) gave stable single droplet formation, but blocking of the nozzle was observed after a few minutes of printer operation, and the jetting was stopped. This may be attributed to the high Z number of 17.6 which is out of the general printable range [150]. However, the Z number of Ink-1 was in the printable range, but nozzle blocking was observed as well. In general, the ink spreads as a thin layer (10 - 20 nm) on and around the print head nozzle during drop ejection. The solvent of the ink rapidly

evaporates due to the air motion around the thin layer caused by pushing ink drops out of the nozzle at high speed. This results in the formation of a solid layer of particles on the nozzle surface, which in turn causes local surface tension gradients and Marangoni flow of the particles on the print head [172]. Nozzle blockage is then often observed. As mentioned in a previous study [157], additives are necessary for stable drop formation for water-based inks. Additives such as ethylene glycol, used in Ink-3 ~ Ink-7, or poly ethylene glycol, used in Ink-5, Ink-7 and Ink-8, are hygroscopic in nature and act as humectants to retard the evaporation of the solvent. The additives were also used for the adjustment of surface tension and viscosity.

4.2.1. Drop generation and printing parameter investigation

As shown in Figure 4.5, there are three different time zones in stable drop formation. In the initial period, events such as fluid ejection and necking of fluid ligaments take place. In the second stage, incidents such as fluid pinch off from the printer head nozzle (where ligaments have the maximum length) take place. It is observed that the maximum ligament length at the time of fluid pinch off is not only dependent on the Z value of the ink but also on the applied voltage and pulse width. A similar observation has been made by others [173] during printing of solvents (ethylene glycol and isopropyl alcohol) without solid particles. The ligament necking velocity is also a function of ink rheology, applied voltage and pulse width. Different ligament lengths were observed for each ink at various voltages and pulse widths. As the Z value decreased, the printer generated drops with longer ligaments. The ligament pinch off time was observed to range between 237 μs and 200 μs for Ink-5 (Z: 3.5), between 150 μs and 155 μs for Ink-8 (Z: 5.9) and between 86 μs and 100 μs for Ink-3 (30.5). In the third stage, the ligament starts to shrink and a stable drop is formed. It is observed that the time and distance at which a stable drop was forming is also a function of Z and the applied voltage and pulse width. A stable drop forms at 325 μs for Ink-5, between 175 μs to 250 μs for Ink-8 and between 110 μs to 125 μs for Ink-3. It has been reported that ligament length and distance required to form stable drops largely influence the minimum standoff distance

(distance between nozzle and the target) and subsequently the printing quality [144, 170]. Insufficient standoff distance leads to mechanical interaction between target and nozzle via fluid ligaments, which destroys the printing resolution.

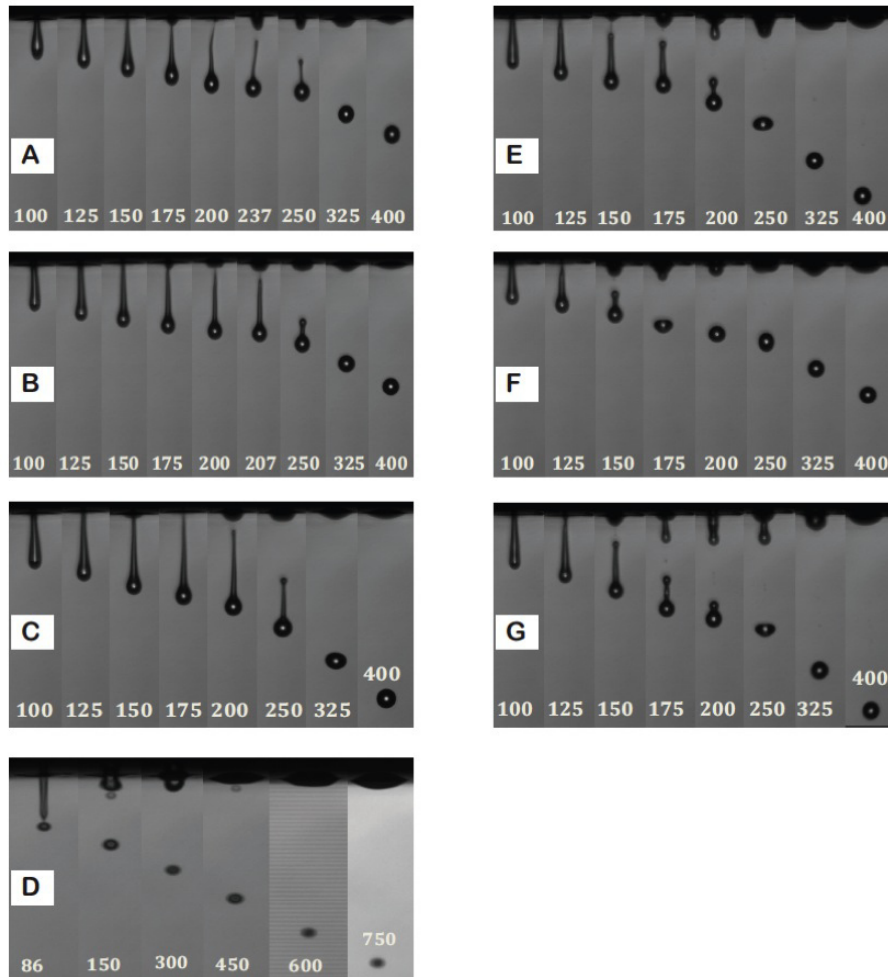


Figure 4.5.: Sequence of photographs taken for different inks at different time intervals (μs) during drop generation; (A) Ink-5, voltage: 100 V, pulse width: 40 μs , (B) Ink-5, voltage: 90 V, pulse width: 35 μs , (C) Ink-5, voltage: 80 V, pulse width: 30 μs , (D) Ink-3, voltage: 42 V, pulse width: 20 μs (E) Ink-8, voltage: 70 V, pulse width: 32 μs , (F) Ink-8, voltage: 60 V, pulse width: 30 μs , (G) Ink-8, voltage: 80 V, pulse width: 36 μs .

Variations in drop size and drop velocity with a variation of voltage and pulse width are shown in Figure 4.6. For a given pulse width (21 μs), the

drop velocity increased from 0.04 to 1.8 m/s by increasing the voltage from 40 to 45 V (Figure 4.6 (a)). At higher voltage, more energy is supplied to the ink and transmitted as kinetic energy to the drop. However, the influence of the voltage on the drop size was marginal. For all voltages applied, the diameter varied only between 50 and 52 μm . The drop velocity and diameter are shown as a function of the pulse width in Figure 4.6 (b) for a given voltage (45 V). The velocity increased with increasing pulse width between 16 and 21 μs . For higher pulse width the drop velocity decreased dramatically. At the maximum drop velocity, droplets with a minimum diameter of 50 μm were generated. Similar trends with pure solvents were reported previously [174]. Moreover, at the maximum velocity stable droplet generation was observed. Hence, for each printing process the pulse width connected to the maximum velocity was applied. The connection of drop diameter and velocity to the Z number cannot be defined clearly as these parameters also depend on many other factors of the printer system, i.e., nozzle diameter, nozzle internal design and the applied voltage wave form for activating the piezoelectric material [151, 175].

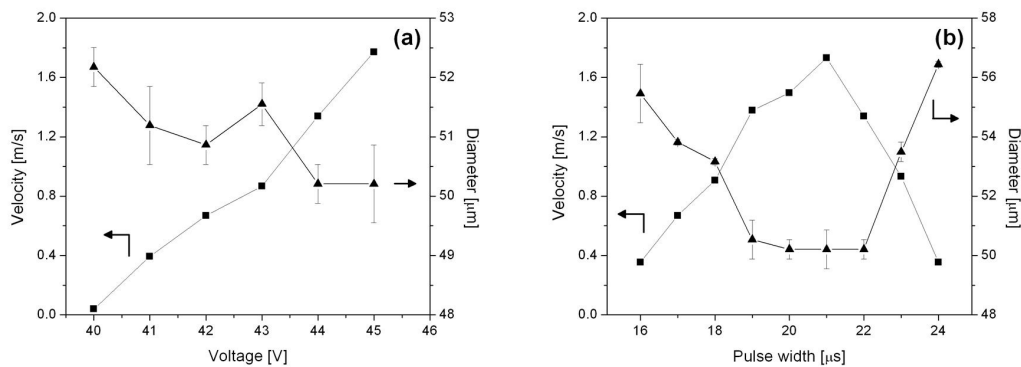


Figure 4.6.: Drop diameter and drop velocity in inkjet printing as a function of (a) voltage with constant pulse width (21 μs) and (b) pulse width with constant voltage (45 V) of Ink-6.

Due to the small width of microchannels, the quality of inkjet printing in microchannels also depends on the precise positioning of the inkjet drops at the desired location, into microchannels. Several factors such as the distance between the nozzle and the target, pinch-off phenomena of the drop and the relative velocity between the print head and the inkjet drop have a large influence on the resolution of the printing [150]. Regarding the relative velocity, the moving velocity of the print head was maintained at 5

$\times 10^{-3}$ m/s. It is much smaller compared to the drop velocity (1.6 - 2.2 m/s) so that the deflection of the jetting angle can be minimized.

4.2.2. Drying and coffee ring formation

For study of the coffee ring effect, individual microdrops were deposited on a planar stainless steel surface as single dots, dried on a heating plate at 70 °C and observed by SEM. As shown in Figure 4.7, for all the inks other than Ink-4 (Z: 7.7) and Ink-1 (Z: 11.5; not used for printing) the coffee ring was absent. During the drying of a single solvent-based inkjet drop, evaporation takes place at the edges of the drop due to contact line pinning. The solvent is continuously supplied to the evaporation zone from the center of the microdrop, which also carries the solid particles to the edges and forms a coffee ring. The Ink-1 (Figure 4.7 (f)) has a coffee ring effect because it is a single solvent system. Figure 4.7 (a), (c) and (d) using co-solvent systems do not show a coffee ring effect. Ethylene glycol was used for these inks.

Kim et al. [176] studied the effect of the concentration of different co-solvents in distinct alumina inks, and they reported that higher concentrations of the co-solvent in the ink decrease the rate of drying and minimize the gradients (concentration gradient and surface tension gradient) required for particle circulation during the drying process. This again leads to a coffee ring effect. Therefore, in case of Figure 4.7 (b), the coffee ring was observed where the concentration of co-solvent (ethylene glycol) was much higher (75 wt. %). Ink-5 and Ink-8 (Figure 4.7 (c) and (e)) have a water soluble polymer (polyethylene glycol-600) as a co-solvent, which blocks the capillary flow of particles from the drop center to the drying plane and suppresses the coffee ring formation. A similar observation was made by Cui et al. [177] for the case of silica inks.

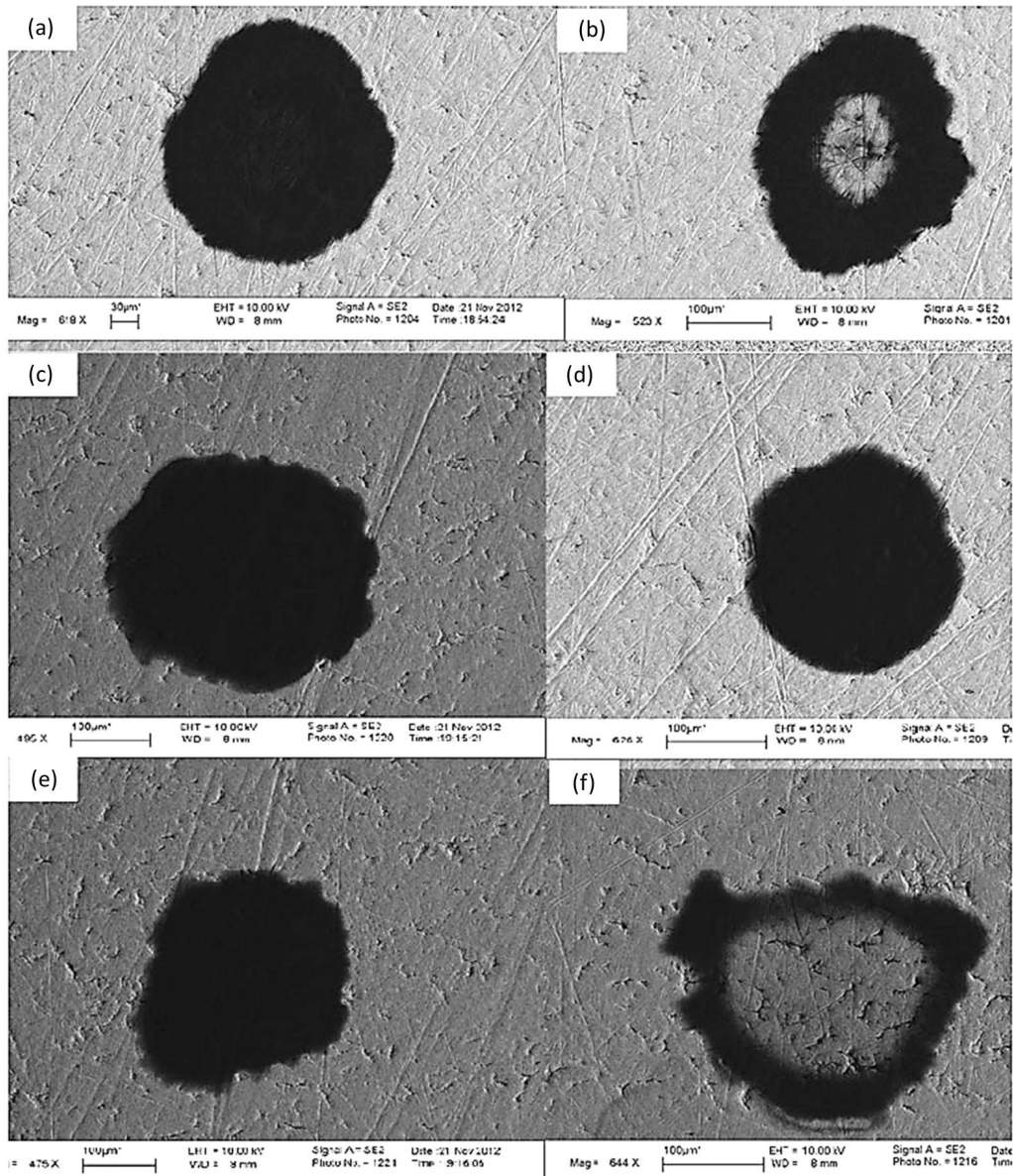


Figure 4.7.: SEM images of dried microdrops of different inks on plain stainless metal surface. (a) Ink-3, (b) Ink-4, (c) Ink-5, (d) Ink-6, (e) Ink-8, (f) Ink-1.

4.3. Investigation of printing in microchannels

4.3.1. Printing of catalyst inks into etched semicircular microchannels

The deposition of inkjet drops (Ink-6) in the semicircular microchannels (MF-2) at different printing pitches was investigated in order to know the spreading and the precision of the drop deposition (Figure 4.8). The inkjet drops are not spreading well in the microchannels due to the surface tension of the ink. The spreading diameter of the 50 μm ink drop at the bottom of the chemically etched stainless steel channels was 85 μm , which is smaller than the channel width (330 μm). In Figure 4.8 (a) and (b), the deposited drops are separated from each other when the ink was printed with 200 μm and 100 μm pitch. For the ink printed with 50 μm pitch (Figure 4.8 (c)), the drops got connected, and a line of ink with a width of 84 μm was formed in the middle of the microchannel. The ink was printed well in the desired place in different patterns. Coating of the entire microchannel surface area is preferred for efficient usage of the geometric surface area available and incorporation of a large amount of catalyst per microchannel. Hence, several series of drops were printed on top of the previously deposited inkjet line. This repetitive printing increased the amount of material deposited. In this way, the mass of support or catalyst placed in the microchannels can be adjusted to the desired level. Ink-6 was printed with 50 μm drop diameter in semicircular microchannels for 17 times to fill the microchannels up to 2/3 of the channel volume. Filling was not increased beyond this level in order to avoid splashing. The printed microchannels were dried at 70 $^{\circ}\text{C}$ for 24 h and calcined as described. A cross-sectional elemental mapping image of a coated microchannel is presented in Figure 4.9 confirming the presence of a uniform and thin coating layer. The coating thickness was around 3 μm over the whole channel length and cross section. It has to be mentioned that the highest content in each graph is identified with pink color and the lowest with blue color. In turn, a direct comparison of the maps in terms of color is impossible (i.e. "red" in one graph may mean a totally different concentration than "red" in other graphs). This holds for all the maps in the following.

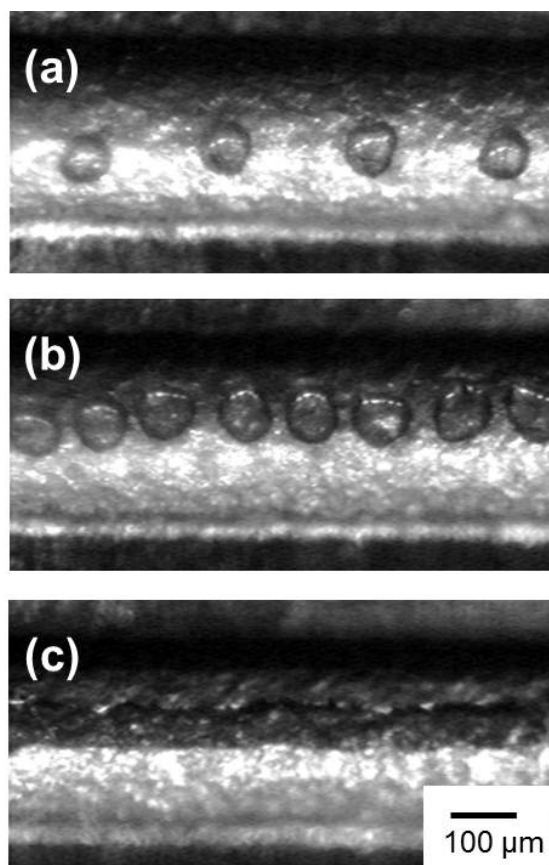


Figure 4.8.: Drop deposition of Ink-6 in a semicircular microchannel (MF-2) with (a) 200 μm , (b) 100 μm , and (c) 50 μm pitch. Voltage 45 V and pulse width 21 μs .

As the ink deposition process was adequately controlled by the inkjet printer, deposition of the alumina layer occurred solely in the microchannels. The adhesion of the alumina layer after calcination was tested through sonication of the coated foils in acetone and measuring the weight difference before and after the sonication treatment. A weight loss of 10 % of the printed alumina layer was observed after 5 min of sonication. It has to be mentioned here, though, that sonication of the coated microchannel foils is a rather harsh condition for an adhesion test on catalyst coatings in a microreactor. Therefore, no significant loss of material due to the gas flow under reaction conditions is expected for the prepared inkjet-printed layers in chemically etched semicircular microchannels.

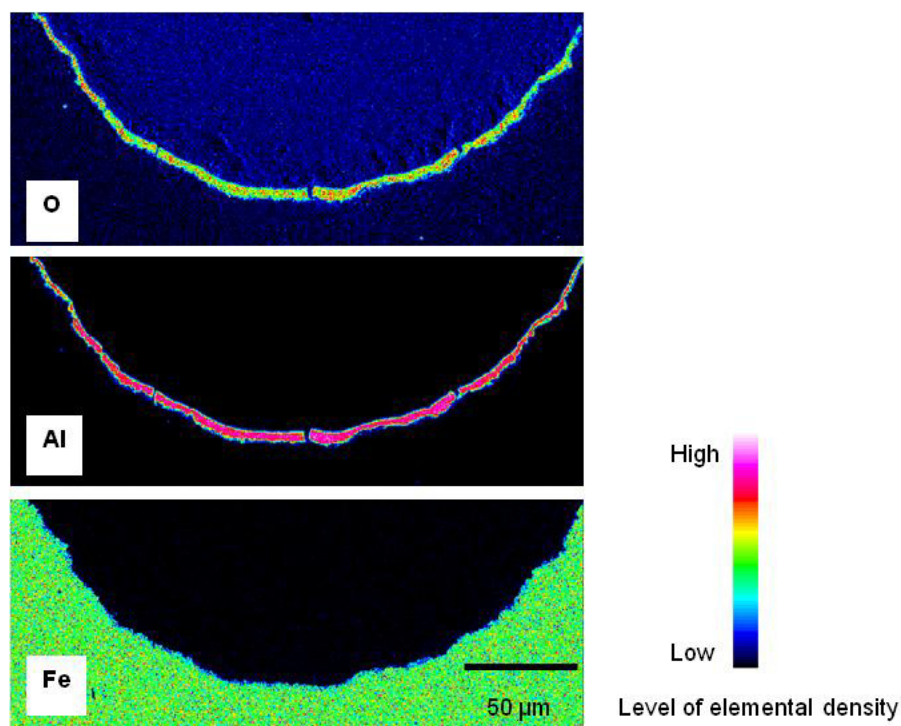


Figure 4.9.: Cross sectional elemental mapping images of an inkjet printed semicircular shaped microchannel (MF-2) with Ink-6, printing repetition 17 times, after drying at 70 °C for 24 h followed by calcination at 550 °C in air for 6 h.

4.3.2. Deposition of catalyst support layers into milled rectangular microchannels

It was observed that in bi-polar pulse mode drop size and drop velocity were higher for inks having lower Z numbers. This reduced the number of cycles required to achieve the desired catalyst loading in microchannels. Therefore, the bi-polar pulse mode was used with Ink-7 to print the alumina support into rectangular microchannels (MF-3). Rectangular microchannels were chosen since the rectangular shape gives a higher surface to volume ratio compared to the semicircular shape. Moreover, as opposed to the semicircular channels having a low aspect ratio of 0.27, for the rectangular microchannels with a higher aspect ratio of 1 undesired deposition on the fins between the channels and the sidebands around the structured area had been observed for the low viscous Ink-7. The trajectory of the smaller size Ink-7 drops with low velocity might be affected by additional air drag generated by the microchannel walls, which influences the positional

accuracy of the printing process. The effect could be minimized by the increase of drop size and jetting velocity. Ink-7 did contain polyethylene glycol and therefore had a higher viscosity (Table 4.1). Higher voltages, i.e., 105 V, than the one used for Ink-6 were applied positively and negatively with 40 μ s pulse width each for the bi-polar pulse mode. In this printing condition, bigger drops and higher jetting velocity were established (drop diameter 100 μ m, velocity 3 m/s) and the printing accuracy was improved. The spreading diameter of the 100 μ m drops of Ink-7 on the bottom of the milled stainless steel channels was about 145 μ m. Hence the spreading ratio was 1.4 in milled rectangular microchannels, where it was 1.7 in etched semicircular microchannels. As different inks were used, the difference in the spreading ratio might be due to differences in the viscosity, drop Weber number and channel surface roughness. In addition, due to the larger drop diameter, the printing time to fill about 2/3 of the channel volume was reduced; each foil was printed only five times. An amount of 55.8 (\pm 1.5) mg of alumina was deposited in one microchannel foil (MF-3). After printing, the alumina layers were dried at 70 $^{\circ}$ C in an oven for 24 h and subsequently calcined in air at 750 $^{\circ}$ C for 6 h. The temperature ramp was set to 2 $^{\circ}$ C/min. At 380 $^{\circ}$ C the temperature was held for 6 h to reduce crack formation of the coating layer during transition from AlO(OH) to γ -Al₂O₃. After the calcination of the inkjet printed alumina layer, impregnation of Rh from an aqueous Rh(NO₃)₃ solution was attempted in order to establish a Rh/Al₂O₃ catalyst. The solution was equally distributed over the surface of the foils using a micropipette. The performance of this catalyst in methane steam reforming was evaluated by a colleague at IMVT [178].

Before the catalysis, several characterization was carried out. The cross-sectional elemental mapping image of a printed microchannel foil in Figure 4.10 shows the distribution of the elements in the catalyst layer. The aluminum map indicates the inkjet-printed support layer. A catalyst layer with a rather homogeneous thickness of 13 ± 0.5 μ m was formed at the bottom of the channel without significantly preferred accumulation of ink in the edges of the channel which is usually observed in filling and drying coating methods. The shape of a deposited solids layer in a confined geometry such as a microchannel depends on the rate of vapor removal versus the rate of agglomeration of particles during the drying process. The geometry of the microchannel affects the vapor removal rate, which is believed to be responsible for the different cross-sectional

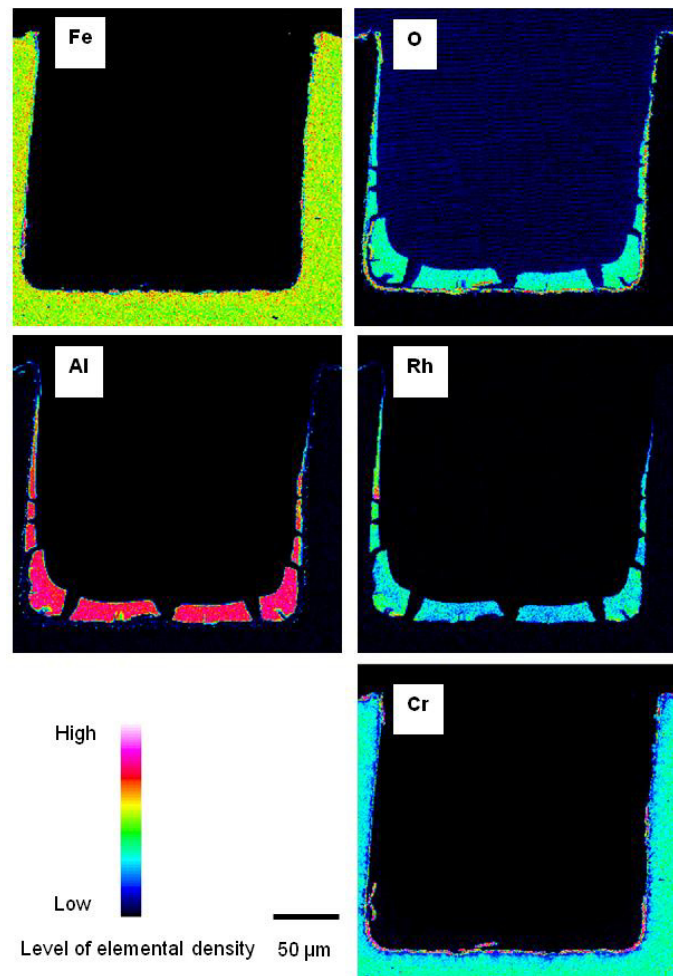


Figure 4.10.: Cross sectional elemental mapping images of an inkjet printed alumina layer in a rectangular microchannel impregnated manually with Rh (15 wt. %).

shapes of the alumina layers obtained in rectangular versus semicircular microchannels (Figure 4.9 and 4.10). This interpretation is supported by results reported by Leng [179] who found that during the drying of a colloidal suspension in rectangular microchannels, the solid concentration in the suspension increases due to solvent evaporation and the drying plane moves along the sidewalls toward the center of the microchannel. Therefore, the particle agglomeration rate and coating thickness were lower at the sidewalls compared with the bottom of the channels.

The catalyst layer in Figure 4.10 shows cracks that have been formed during the drying process. Structural defects in coatings such as delamination and crack formation are more intense in microchannels than on plane surfaces due to unevenly developed capillary forces during drying. Moreover, the

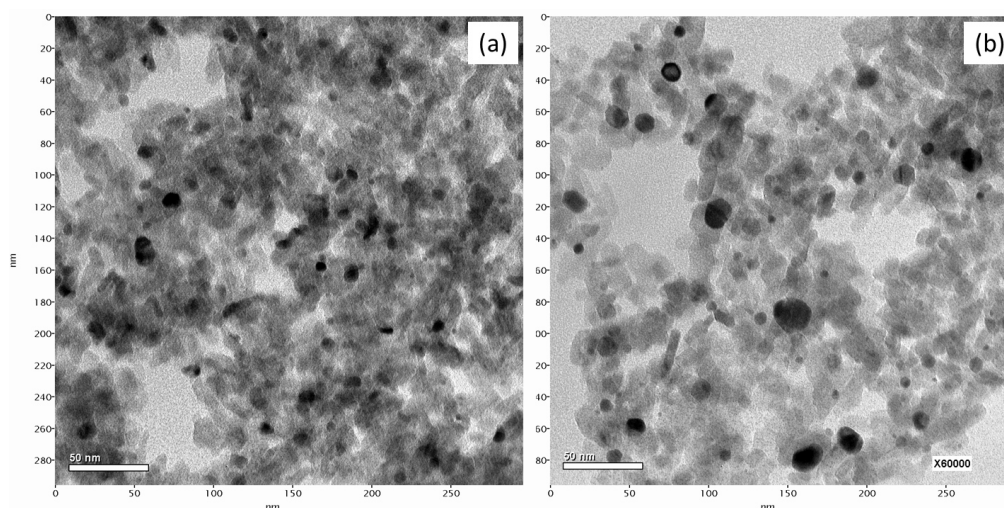


Figure 4.11.: TEM images of inkjet printed Rh/Al₂O₃: (a) fresh state, (b) after reaction.

dehydration of pseudo-Boehmite during drying and calcination releases a large amount of water (near 30 wt.% of the pseudo-Boehmite) changing its shape along with the crystal structure [180]. All this promotes crack formation and delamination.

WDS analysis of the cross sections showed the presence of an alumina/chromia-rich layer beneath the printed alumina layer, which was formed due to the oxidative heat treatment of the Nicrofer[®] foils at 800 °C prior to the coating (Figure 4.10). The active metal Rh is uniformly distributed in the alumina layer. The surface area and pore volume of the as prepared catalyst were 79.7 m²/g and 0.375 ml/g, respectively (BJH desorption) corresponding to a surface area enlargement ratio of 915 m²/m² relative to the channel wall, which is pretty high compared to the surface area enlargement ratio of 78 m²/m² for 1 μm thin CeO₂-based steam reforming catalyst coatings established in earlier research at the institute [181]. Hydrogen chemisorption performed on pieces of catalyst-coated microchannel plates in fresh state revealed a Rh surface area of 3.4 m²/g of catalyst layer which translates into a Rh dispersion of 5.1 % (average Rh particle size 21 nm). By TEM investigations performed on powdery samples recovered from the catalyst-coated microchannels in fresh state and after a total time of 167 hours under reaction conditions, a higher Rh dispersion of 12.4 % (average Rh particle size 8.8 nm) was determined for the fresh catalyst as well as a gradual shift of the Rh particle size distribution toward larger particles indicating sintering during reaction, which decreased the

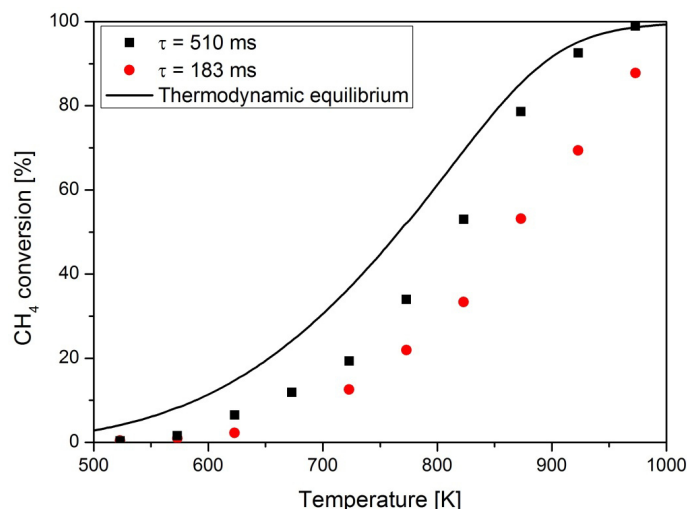


Figure 4.12.: Methane conversion as a function of temperature for two different residence times and constant molar ratios at ambient pressure ($c_{\text{CH}_4} = 10$ vol. % and $c_{\text{H}_2\text{O}} = 40$ vol. %, corresponding to a steam to carbon ratio of 4).

Rh dispersion to 9.4 % (11.8 nm). A TEM image is shown in Figure 4.11. The BET surface area showed a concomitant reduction to $53.6 \text{ m}^2/\text{g}$. Given the limitations of the chemisorption measurements with catalyst-coated plates, i.e., low and difficult to assess amount of catalyst, the TEM results are considered more reliable. Comparing these results to the Rh dispersion by TEM of 10.6 % reported by a group from Haldor Topsøe for a 1 wt. % Rh catalyst on a ZrO_2 support with low surface area ($15 \text{ m}^2/\text{g}$) [182] shows the benefit of a high surface area support in terms of accepting higher metal loadings without a detrimental effect on dispersion.

With $13 \mu\text{m}$ the thickness of the catalyst layer deposited in the rectangular microchannels is higher compared to that obtained with conventional sol-gel methods, where the catalyst layer thickness is often not exceeding $1 \mu\text{m}$ [183]. To assess whether its catalytic performance is still not influenced by heat and mass transport limitations well-known experimental diagnostic criteria adapted to the geometry of a catalyst layer on a metal plate were checked using effective reactor-averaged reaction rates and the apparent activation energy derived from the measured conversion data [184]. According to these calculations, no significant influence of the external mass transfer on the observed reaction rate is expected. Neither is there an overtemperature expected on the surface or inside of the catalyst layer. On the other hand, due to the high Rh content of the catalyst layer, at

the highest temperature and lowest contact time the estimated value of the generalized Weisz modulus is slightly exceeding the limiting value of 0.05 above which pore diffusion is considered to start influencing the performance ($\eta < 95\%$, valid for a first order irreversible reaction). Therefore, in accordance with the approximating nature of these criteria some influence of pore diffusion at the highest reaction temperature applied cannot be ruled out. However, a severe limitation of the reaction rate by pore diffusion can still safely be excluded.

The experimental methane conversion in the steam reforming reaction as a function of temperature for two different residence times (183 ms and 510 ms, corresponding to a W/F ratio of 6.8 and 19.7 ($\text{kg}_{\text{cat}}\text{s}$)/ mol_{CH_4} , respectively) is shown in Figure 4.12. The equilibrium conversion values indicated were calculated with the HSC[®] Software by accounting for CH_4 , H_2O , H_2 , CO , CO_2 and N_2 in the reaction mixture. CH_4 conversion increased with temperature. At the highest residence time, a maximum conversion of 98.9 % was reached, and the reaction was clearly limited by the thermodynamic equilibrium. For a lower residence time of 183 ms, the CH_4 conversion was less, i.e., reaching 87.8 % at 973 K.

4.3.3. Zeolite printing in microchannels

For solid particle printing, additional treatments such as particle size regulation and particle suspension are required. These processes may cause alteration of the catalytic properties. Hence, a printing of precursor solutions which do not contain the final form of catalyst particles but pre-phase nano seeds of metal oxides or metal hydroxides was evaluated.

In case of ZSM-5 synthesis, before hydrothermal synthesis the ZSM-5 precursor is a colloid of hydrolized alkoxy silanes [185]. This precursor can be used as an ink with additives to optimize printability. The ZSM-5 synthesis mixture was prepared by the CRT group and a ZSM-5 precursor ink was prepared at IMVT. The preparation method is reported in the appendix. Figure 4.13 shows the SEM images of the printed microchannel. At low magnification ZSM-5 particles were not visible. When the microchannel surface was magnified, small particles in nanometer size were observed. At the same time, large size particles ($> 1\ \mu\text{m}$) were

also observed. The small particles were ZSM-5 but the large particles could not be identified. As shown in Figure 4.13 (c), the fin was not coated with ZSM-5. Therefore, it can be known that the selective coating by inkjet printing was achieved. However, the uniformity of the catalyst layer thickness should be improved since some channels showed uneven coating surface. The same printing method was applied on CZA coated microchannels in order to establish the double-layer. After the treatment for ZSM-5 particle growth, some unknown materials which are not ZSM-5 crystals were observed (Figure A.2).

These attempts have opened a possibility for precursor printing for improved catalyst coatings in microchannels. Due to time restrictions, more thorough investigations could not be carried out within this thesis. Further studies are needed to develop the printing of precursor inks.

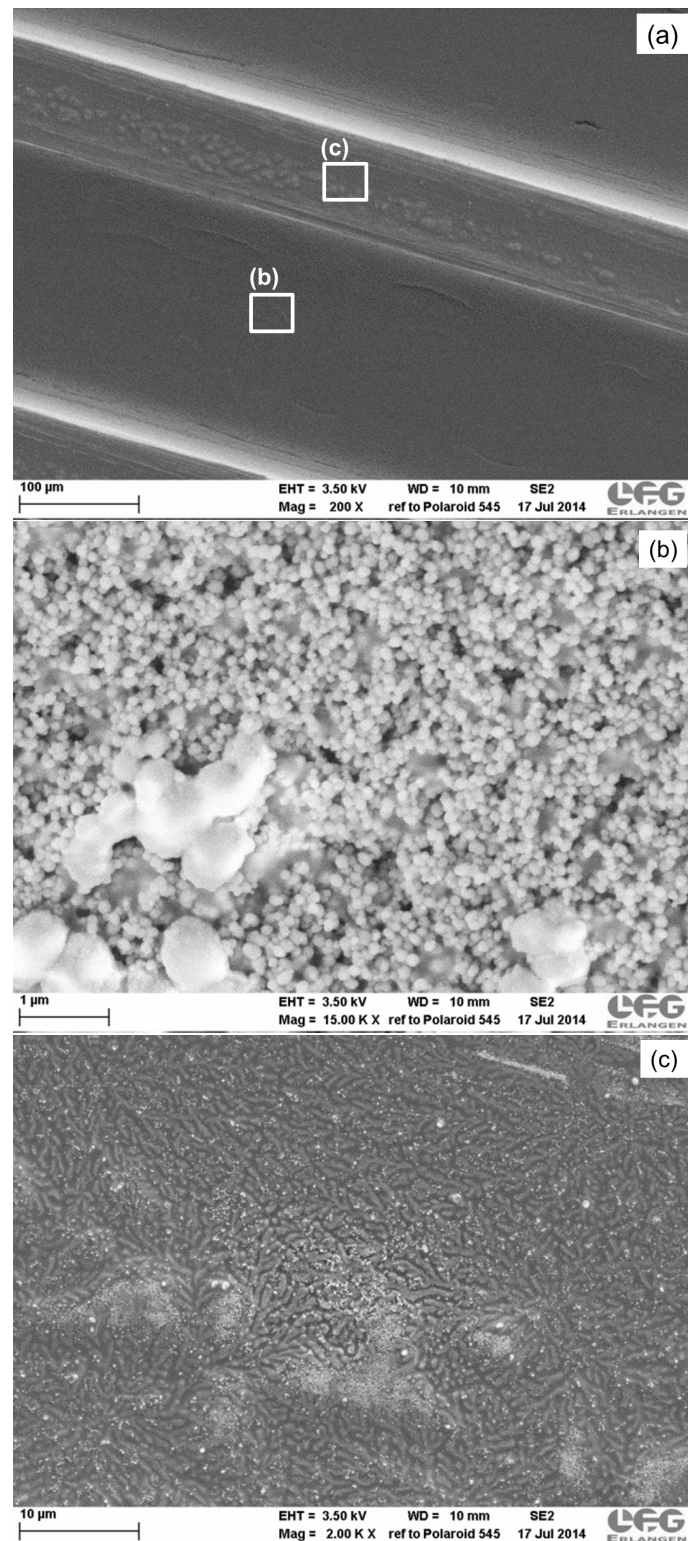


Figure 4.13.: SEM images of a ZSM-5 precursor printed microchannel. (a) Microchannel and fin, (b) higher magnification of the microchannel surface, (c) higher magnification of the surface of the fin.

5. Direct DME synthesis over double-layer catalysts in microchannel reactors

5.1. Bifunctional double-layer catalyst coating

5.1.1. Ink formulation

As mentioned in the previous chapter, the ink formulation is an important step prior to successful inkjet printing of catalyst layers. The ink formulation for FSP-CZA and ZSM-5 printing, from particle dispersion to Z number control, was investigated.

FSP-CZA ink

For catalyst ink formulation, water was employed as an ink solvent. Due to its non-toxicity and low evaporation rate, it is commonly used for paper printing inks as a primary solvent. The A631 catalyst showing the best catalytic activity was selected for preparation of a CZA ink. Good ink here means that particles are homogeneously distributed in the ink and there is no sedimentation of particles. Local variations of the particle concentration can induce non-uniform catalyst amounts on printed substrates. Moreover, non-dispersed ink means that the catalyst particles are agglomerated, which increases the risk of plugging the nozzle at the print head. At first the dispersibility of the CZA catalyst particles in water was studied. Figure 5.1 shows CZA dispersions in water with different pH values. The CZA

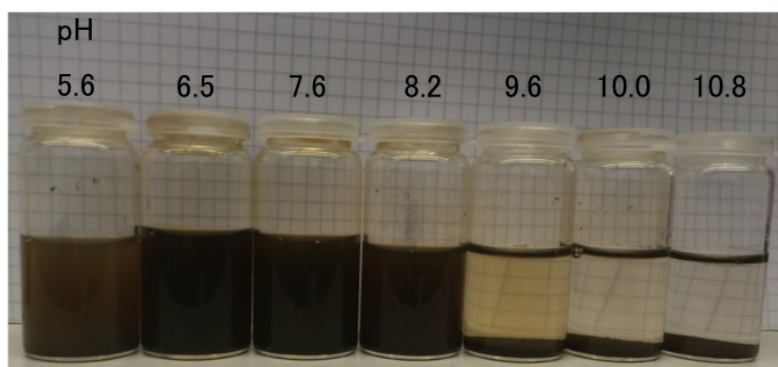


Figure 5.1.: Pictures of CZA (A631) 0.1 wt % in water after 24 hours.

catalyst is sensitive to the pH value, so that decomposition of the catalyst at strongly acidic or basic conditions takes place. As shown in Figure 5.1, CZA particles were quite well dispersed in neutral or slightly acidic condition, while sedimentation took place in weak basic condition.

In order to know the electrostatic charge change on the surface of the particles which are related to particle interaction and repulsion, zeta potential measurements were carried out. High zeta potential means high repulsion force between particles. Hence, particle agglomeration is reduced and the dispersion is improved. As to be seen in Figure 5.2, CZA showed a highly positive zeta potential near neutral pH area. At around pH = 10.3 the isoelectric point is observed. Therefore, electrically repulsive stability of CZA particles in water can be established without pH control. However, this does not guarantee the absence of sedimentation over long time. Nanoparticles usually possess a tendency of re-agglomeration following sedimentation due to the high surface energy [186]. An introduction of some dispersants is necessary to enhance the zeta potential or introduce a steric hindrance [187]. Two dispersants, poly acrylate (Dolapix CE 64) and poly ethyleneimine ($M_n \sim 60,000$, Sigma-Aldrich), were used. As shown in Figure 5.2, both dispersants can increase the zeta potential positively or negatively. After a few days of mixing poly ethyleneimine in a particle dispersion, clearing of the dispersion was observed. The particles were completely dissolved. The solution was bluish transparent. The strong basic poly ethyleneimine dissolved the catalyst particles. Although the pH of the dispersion was controlled to neutral pH after mixing poly ethyleneimine, it could not be avoided. It has been known that poly ethyleneimine is a strong copper scavenger [188]. Therefore, Dolapix CE 64 was used for the further ink formulation process.

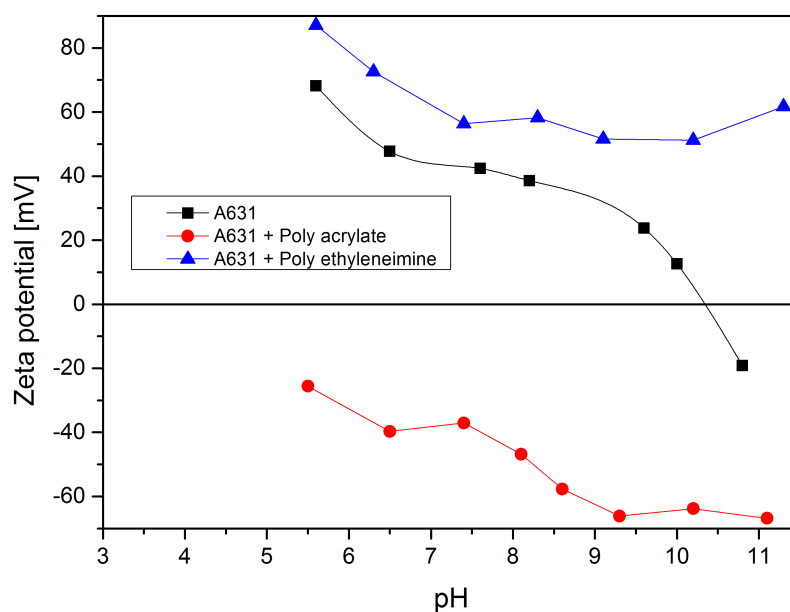


Figure 5.2.: Zeta potential diagram of CZA 0.1 wt% without and with additives (0.1 wt%) in water.

FSP produces nanoparticles in powder form. This means that the primary particles are nanosized, but these are agglomerated in the dry powder to micron size. Breaking of the agglomerates to small size is inevitable for achieving a good dispersion of dried powder in a solvent. In this study, a ball milling technique was used to break the agglomerated CZA particles. In order to prevent re-agglomeration, Dolapix CE 64 was added into the CZA dispersion. Figure 5.3 shows the effect of ball milling on the particle size. Within 10 minutes, the particle size was reduced dramatically below 1000 nm. Further ball milling rather increased the particle size. The high energy during the ball milling might cause re-agglomeration of particles. Therefore, 10 minutes ball milling was chosen for the CZA ink formulation.

Since during the ball milling process a high amount of energy is transferred mechanically to the catalyst particles, there might be change of structural or chemical properties [189]. Figure 5.4 shows x-ray diffraction patterns of the CZA material. After ball milling the peaks assigned to copper and zinc oxide were intensified. The mechanochemical treatment by ball milling is able to increase crystallinities of metal oxides following a sharpening of the corresponding XRD peaks for the metal oxides [190]. On the other hand,

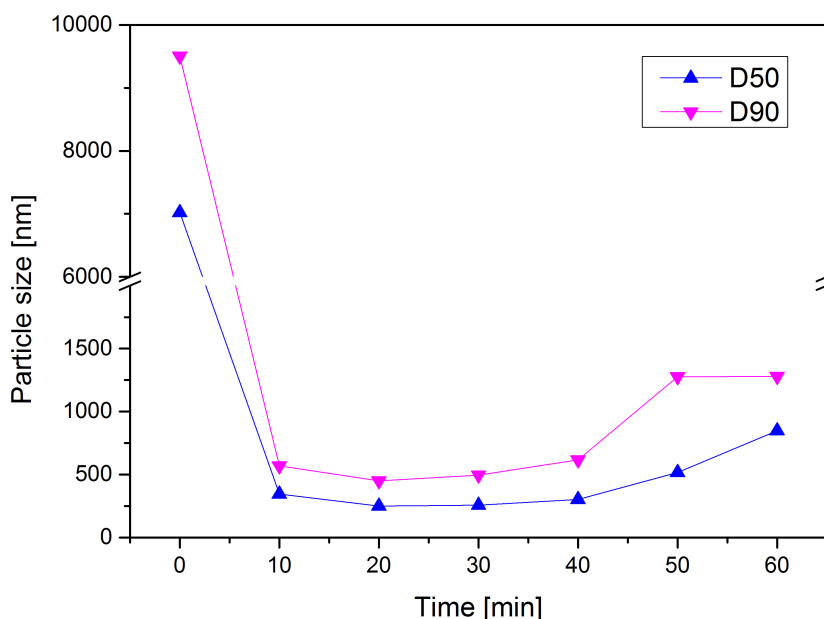


Figure 5.3.: Particle size change after ball milling of CZA dispersion. 10 wt. % CZA and 0.25 wt. % dispersant in water; 1000 rpm; 200 μm size YSZ beads. D50 and D90 indicate that 50 % and 90 % of the volume distribution are below these values, respectively.

the peaks for aluminum oxide (2 theta around 40 and 46) disappeared. The FSP-synthesized fresh CZA showed bulky particles of crystalline aluminum oxide (Figure 3.5). These particles were broken down and became x-ray amorphous. Aluminum is a promoter in CZA catalysts. Its distribution in the catalyst structure and interaction with zinc can improve the activity. It probably changed the catalytic activity of the CZA. If the distribution of aluminum oxide is high, a positive change of catalytic activity is expected [131].

The reducibility was investigated by TPR analysis. As shown in Figure A.3, after ball milling the reduction temperature was increased. This shift of the TPR peak may be related to an increase of the Cu-O bond and a strong interaction with the support [132, 191]. The BET surface area of the CZA sample after ball milling was decreased to about half of the original value. By ball milling the particle size was reduced, but probably the microporous structure of the original catalyst collapsed. As shown in Figure A.4, initially CZA possessed micro pores. Ball milled CZA showed mostly mesopores

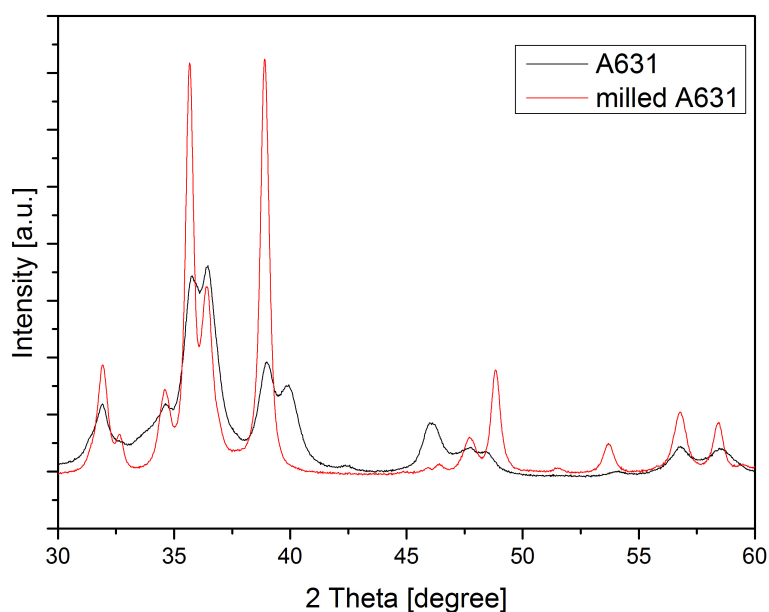


Figure 5.4.: XRD patterns of CZA (black) and 10 minutes ball-milled CZA (red).

Table 5.1.: BET surface area of CZA and 10 minutes ball-milled CZA.

| | CZA | Ball-milled CZA |
|--|-------|-----------------|
| BET surface area (m^2/g) | 41.04 | 22.73 |

and little volume of micro pores. The change of the BET surface area is related to this pore structure change.

Ball milling has altered not only the size of the catalyst particles, but also x-ray crystallinity, reduction property and pore structure. In order to clarify these observations and understand the effects on catalytic properties, further characterizations with regard to the catalytic activity have to be carried out.

ZSM-5

H-ZSM-5 ink was prepared in the same manner as the CZA ink. H-ZSM-5 was ball milled to decrease the particle size; the original particle size was around $10 \mu\text{m}$ (Figure A.5 (a)). H-ZSM-5 is a harder material than

Table 5.2.: BET surface area of H-ZSM-5 and ball-milled H-ZSM-5.

| | BET Surface area (m ² /g) |
|------------------------|--------------------------------------|
| H-ZSM-5 | 353.6 |
| H-ZSM-5 1 hour milled | 220.2 |
| H-ZSM-5 2 hours milled | 176.0 |

CZA, thus the ball milling time was increased to obtain small particle size. As shown in Figure 5.5, $< 1 \mu\text{m}$ particles could be obtained after 20 minutes ball milling. When the ball milling time reached 120 minutes, the suspension was stable and able to be applied in inkjet printing without any dispersants. The H-ZSM-5 was crushed to small particles losing its original shape (Figure A.5). The SEM images showed clumps of the crushed H-ZSM-5 particles.

The crystallinity of the ball milled H-ZSM-5 was analyzed by XRD (Figure 5.6). As shown, the crystalline H-ZSM-5 was maintained after ball milling, but the crystallinity got reduced. The reduction of crystallinity was estimated from the peak area change between 22.5 and 25 degrees [192]. After ball milling of 1 and 2 hours, the crystallinity was reduced to 46.9 % and 28.8 % of the original H-ZSM-5, respectively. On the contrary, the amount of acid sites was increased. Figure A.6 presents the NH₄-TPD analysis of the original H-ZSM-5 and the ball-milled H-ZSM-5. The longer the ball milling was carried out, the larger the TPD peak area. Therefore, by ball milling the activity of H-ZSM-5 can be increased, as also found in other research reports [192–194].

The BET surface area was also investigated (Table 5.2). The original H-ZSM-5 showed a surface area of 353.6 m²/g. The BET surface area of the ball-milled H-ZSM-5 was lower with 220.2 m²/g and 176 m²/g for 1 hour and 2 hours ball milling, respectively. This could be the consequence of a partial collapsing of the zeolite pore structure by the ball milling.

Through the characterization, it could be established that ball milling provides negative and positive effects on the catalytic properties. The ball-milled H-ZSM-5 was therefore studied in methanol dehydration. In Figure 5.7 it can be seen that the original H-ZSM-5 converted well methanol to DME below 260 °C although conversion was not high. It was increased at higher reaction temperature. Until 245 °C DME was almost the only product. Hydrocarbons, mostly propylene, were produced from

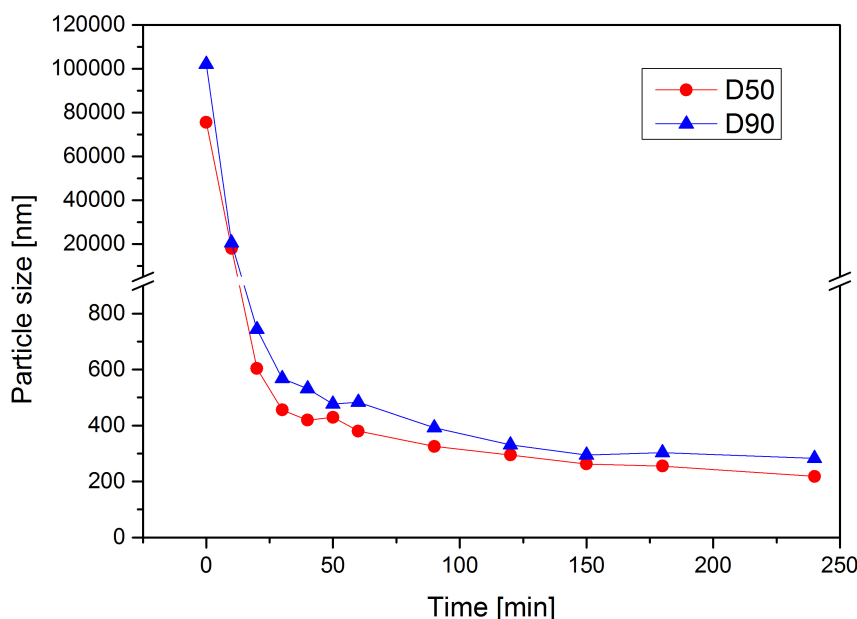


Figure 5.5.: Particle size change after ball milling of the H-ZSM-5 dispersion. 10 wt. % H-ZSM-5 in water; 1000 rpm; 200 μm size YSZ beads. D50 and D90 indicate that 50 % and 90 % of the volume distribution are below these values, respectively.

260 °C on. When the reaction temperature reached 290 °C, about 1/4 of the DME selectivity was lost. Below 300 °C, the dehydration to DME was the dominant reaction [195].

This trend was repeated with the ball-milled H-ZSM-5. DME was the major product, and hydrocarbons started to be produced at increased reaction temperature (Figure 5.7, 5.8, 5.9). 1 hour milled H-ZSM-5 showed a little higher methanol conversion than 2 hours milled H-ZSM-5. On the contrary, the DME selectivity was higher with 2 hour milled H-ZSM-5. It showed almost 100 % DME selectivity until 260 °C. In conclusion, the dehydration property of H-ZSM-5 was not changed significantly by the ball milling.

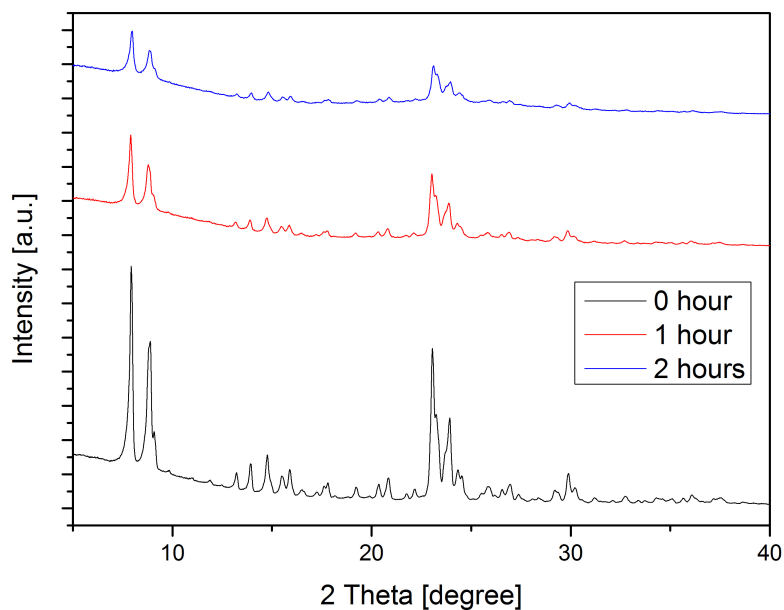


Figure 5.6.: Change of the XRD patterns of ZSM-5 by ball-milling.

Table 5.3.: Testing condition of methanol dehydration over H-ZSM-5 in a Bertly recycle reactor.

| | |
|---------------------------|----------------|
| Pretreatment | |
| Gas | N ₂ |
| Temperature | 250 °C |
| Duration | 24 hours |
| Reaction | |
| Temperature | 215 - 290 °C |
| Pressure | 1 bar |
| Mass of catalyst | 1.29 g |
| Particle size of catalyst | 50 - 100 μm |
| Blower speed | 2000 rpm |
| Methanol:N ₂ | 11.8:1 |

30

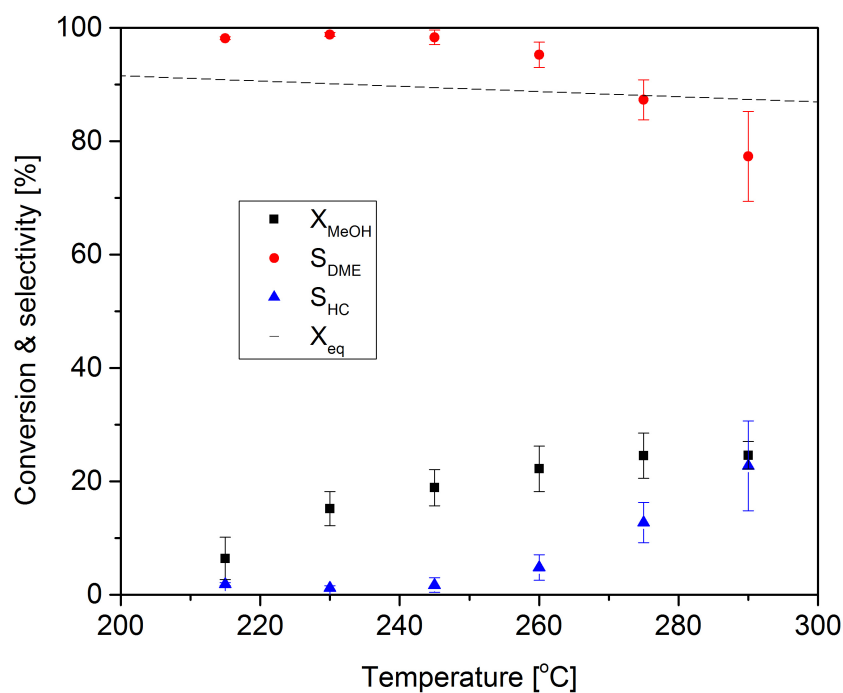


Figure 5.7.: Methanol dehydration over the as prepared H-ZSM-5 catalyst. High pressure Berty recycle reactor; particle size between 50-100 μm ; 250 °C pre-treated under N_2 flow; feeding Methanol: N_2 = 11.8: 1. GHSV = 5488 ml/ $\text{g}_{\text{cat}}\text{h}$, p = 1 bar. The equilibrium conversion values (X_{eq}) of methanol were calculated with the HSC[®] Software.

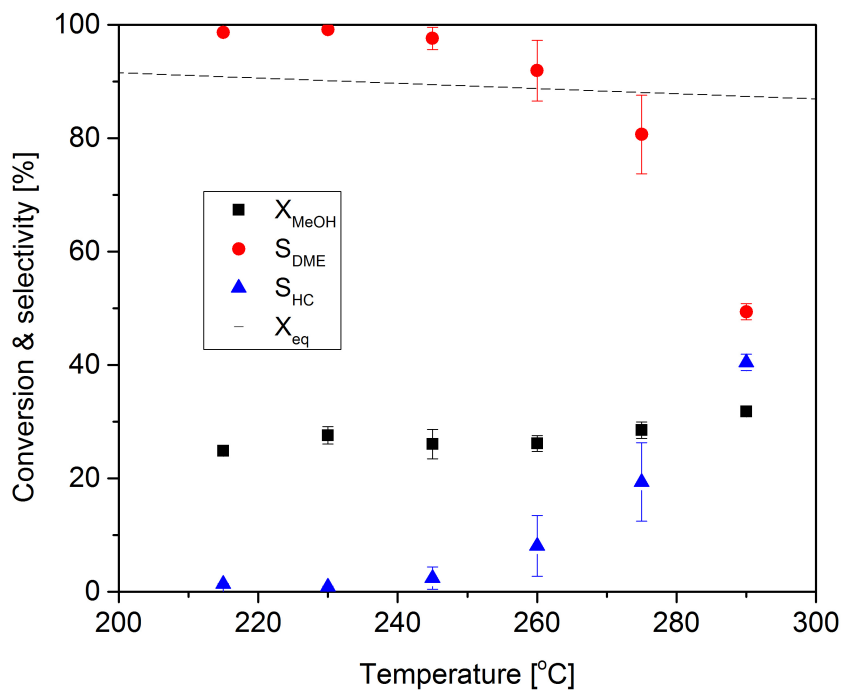


Figure 5.8.: Methanol dehydration over 1 hour ball milled ZSM-5. High pressure Bertly recycle reactor; particle size between 50-100 μm ; 250 °C pre-treated under N_2 flow; feeding Methanol: N_2 = 11.8: 1. GHSV = 5488 ml/ $\text{g}_{\text{cat}}\text{h}$, p = 1 bar. The equilibrium conversion values (X_{eq}) of methanol were calculated with the HSC[®] Software.

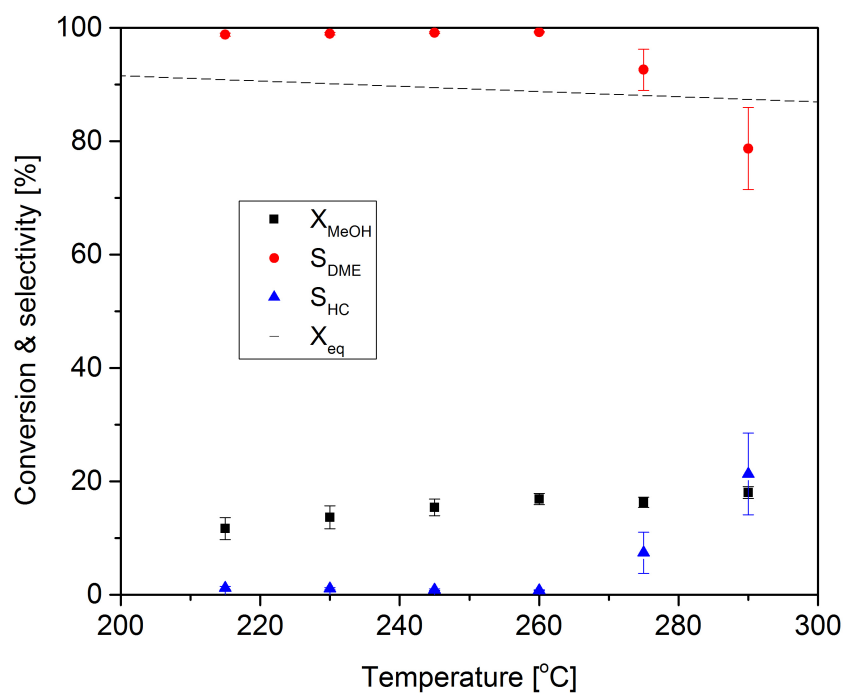


Figure 5.9.: Methanol dehydration over 2 hours ball milled H-ZSM-5. High pressure Bertly recycle reactor; particle size between 50-100 μm ; 250 $^{\circ}\text{C}$ pre-treated under N_2 flow; feeding Methanol: N_2 = 11.8: 1. GHSV = 5488 $\text{ml/g}_{\text{cat}}\text{h}$, p = 1 bar. The equilibrium conversion values (X_{eq}) of methanol were calculated with the HSC[®] Software.

Z number control

After establishing stable dispersions of particles, Z number control was carried out. In order to be printable, the Z number of an ink should be controlled within the range of 4 -14 even if this is not a fully reliable parameter as mentioned in the last chapter. Several additives are recommended in literature to improve the printability. Ethylene glycol, propylene glycol and glycerol as non-toxic and water-soluble additives were mixed with the prepared catalyst dispersion. Figure 5.10 shows the Z number of CZA and H-ZSM-5 inks. CZA inks have a higher Z number compared to H-ZSM-5 inks. The Z number of the CZA inks can be optimized with all additives. Propylene glycol-added CZA inks showed optimum Z numbers at concentrations between 30 and 50 wt%. With glycerol and ethylene glycol optimum Z numbers were given at above 40 %. In case of H-ZSM-5 inks only propylene glycol can give an optimum Z number at 40 and 50 %. Therefore, the final CZA and H-ZSM-5 inks were formulated with ethylene glycol 50 % and propylene glycol 50 %, respectively.

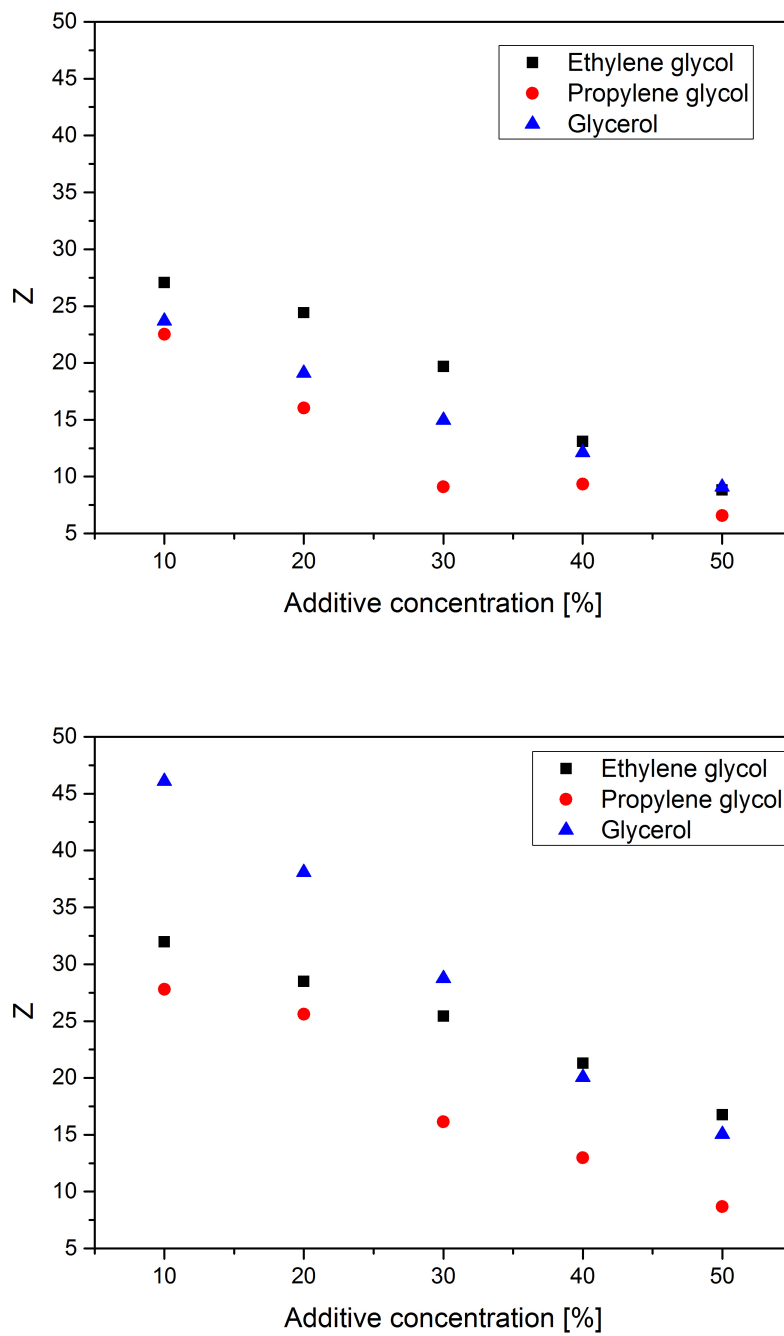


Figure 5.10.: Z number change of 10 minute milled CZA (top) and 2 hours milled H-ZSM-5 (bottom) with additives.

Table 5.4.: Properties of the final CZA and H-ZSM-5 inks.

| | CZA ink | H-ZSM-5 ink |
|---|-------------------------------|--------------------------------|
| Solvent | Water | Water |
| Particle concentration | 5 wt. % | 5 wt. % |
| Ball milling time | 10 minutes | 120 minutes |
| Dispersant | Dolapix CE 64 | - |
| Formulating additive (Concentration) | Ethylene glycol (50 wt. %) | Propylene glycol (50 wt. %) |

5.1.2. Double-layer printing

The double-layer catalyst was printed based on the results described in the previous sections. The specific information about the final formulation of the catalyst inks is in Table 5.5. The additives used were different for the two inks. The particle concentration was kept the same. The printing strategy using these inks for double-layer coating has been illustrated in Figure 1.17. At first the CZA layer was printed and fully dried, and then the H-ZSM-5 layer was printed on top of that.

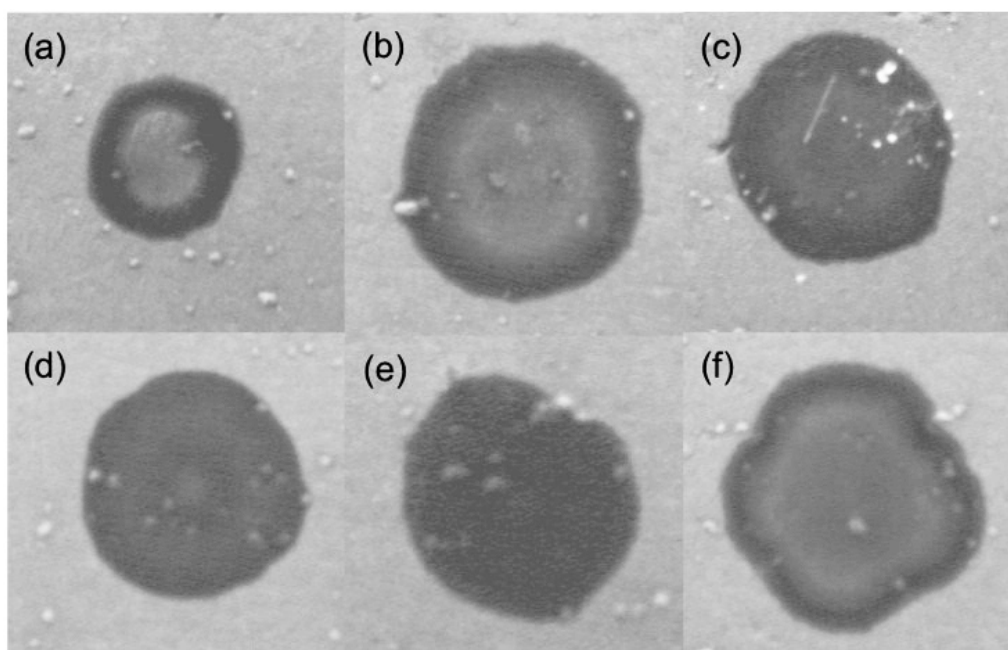


Figure 5.11.: Coffee ring effect of the CZA ink with 50 % ethylene glycol on a flat stainless steel surface at different drying temperature. (a) 80 °C, (b) 150 °C, (c) 250 °C, (d) 350 °C, (e) 450 °C, (f) 550 °C.

For the double-layer catalyst system in microchannels, the CZA catalyst is located at the bottom where it directly contacts the microchannel surface. Thus, uniform spreading without coffee ring effect, good adhesion and absence of cracks in this layer are important for successful top-layer formation. Once the CZA layer is well established, H-ZSM-5 will be formed along the bottom layer. The drying temperature can influence the coating distribution. In order to know the impact of the drying temperature, coffee ring formation of the CZA ink with different drying temperature was investigated on a flat stainless steel plate. Figure 5.11 shows pictures of dried CZA ink droplets at different drying temperature. Slow drying at a low temperature 80 °C gave an obvious coffee ring. When the temperature was higher, the coffee ring effect was minimized. Although this ink used a co-solvent system, water and ethylene glycol, the coffee ring appeared at 80 °C and 150 °C. The co-solvent effect is subject to the environment of the drop such as additives, temperature and geometry [196]. In this case, the coffee ring effect is probably due to the difference of the evaporation rate in the center and at the edges of the drop [197, 198]. At high temperature, 350 °C and 450 °C, this effect might be minimized because the evaporation rate is more or less similar everywhere and the movement of particles towards the edge is not fast compared to evaporation. However, a too high temperature, 550 °C, also produced a coffee ring. Therefore, 450 °C was applied for the drying process of the printed layers. In addition, a high temperature treatment above 350 °C is necessary to remove the polymeric dispersant.

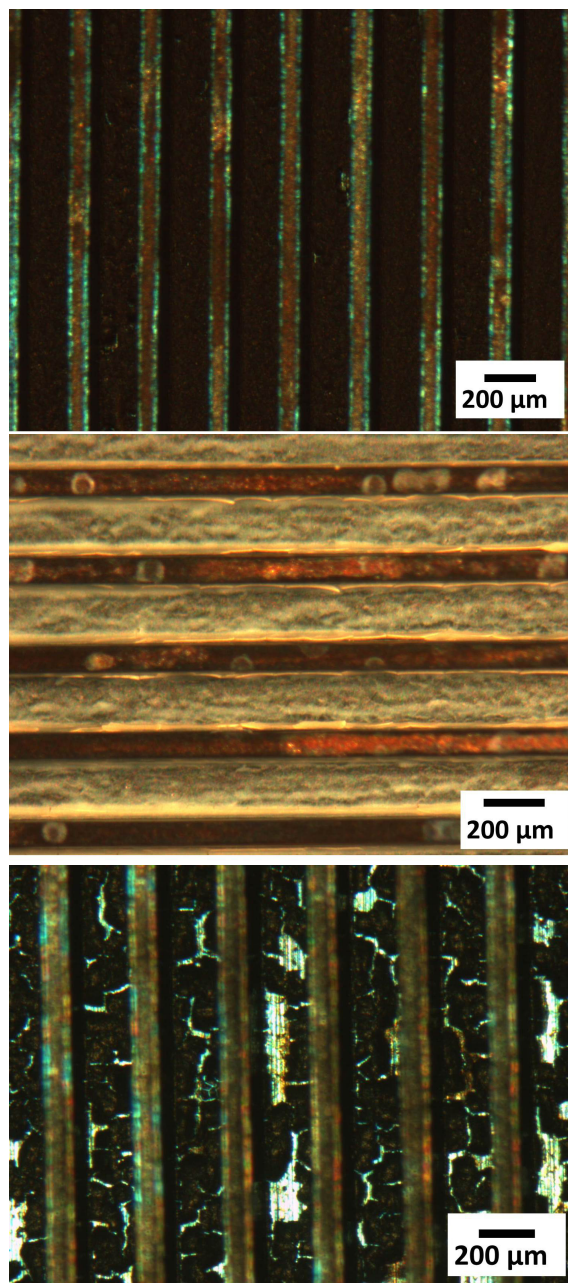


Figure 5.12.: Microscopic images of printed and dried microchannel foils. CZA (top) and H-ZSM-5 (middle) dried at 450 °C for 2 minutes; CZA layer (bottom) dried at 80 °C for 2 hours and calcined at 550 °C for 5 hours.

The drying time affected the adhesion of the coating on the microchannel surface. When the printed CZA layer was dried at 450 °C for 2 minutes, the coating showed good adhesion (Figure 5.12). However, the coating treated at 550 °C for 5 hours was easily peeled off. This may be due to the difference of thermal expansion coefficient between the catalyst layer (ceramics) and

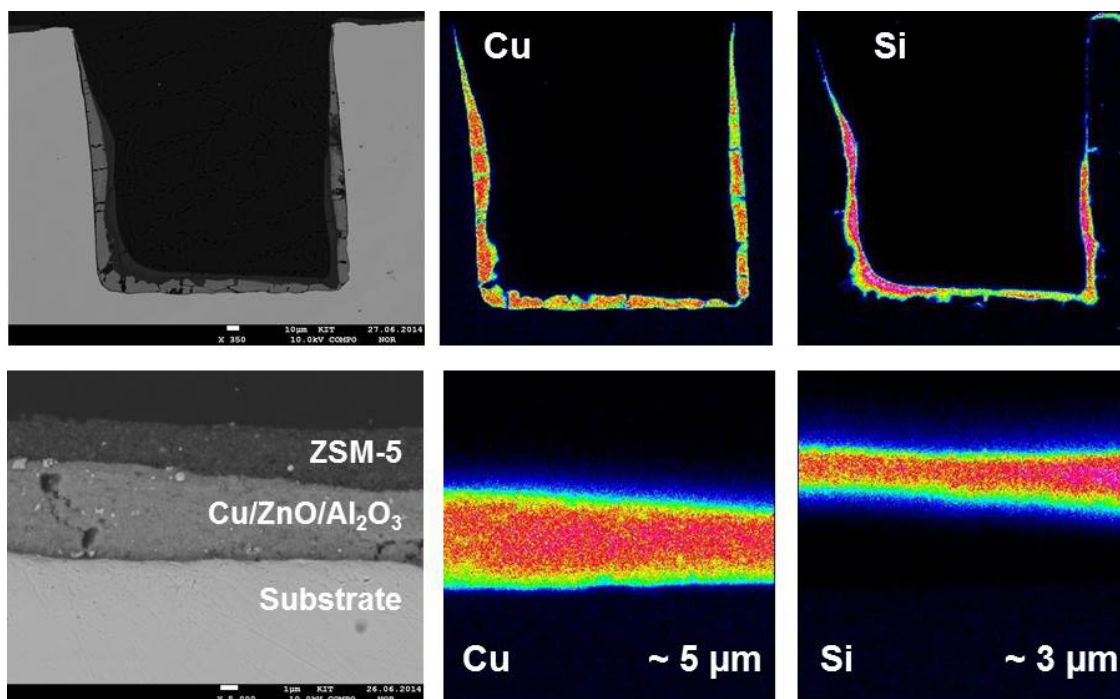


Figure 5.13.: Cross-sectional images and elemental mapping of a double-layer (DL3) coating in one microchannel. Intensity of elemental level: red (high) to blue (low).

microchannel (stainless steel).

Figures 5.13 and A.7 show cross-sectional images of the printed double-layer (DL3). Two catalyst layers were formed well sequentially in the microchannel. The bottom layer (CZA) was thick and contained cracks. The top layer (H-ZSM-5) was thinner and, as shown in the elemental analysis image (Figure 5.13 right), well covering the bottom with almost no cracks. This is a remarkable achievement since perfect covering of CZA can reduce the out-diffusion - without dehydration at the H-ZSM-5 layer - of methanol that is produced in the bottom layer. Nevertheless, the top of the side walls could not be coated sufficiently due to the gravity effect. Undesirable coating on microchannel fins was also observed sometimes, thus more careful printer operation should be carried out. The average layer thicknesses in the microchannel bottom region were 5 and 3 μm for CZA and H-ZSM-5, respectively. The layer thickness can be controlled by the operation of the printer. Although the printed double-layer needs to be improved still, the inkjet printing represents a considerable improvement of catalyst layer formation compared to a conventional micro pipette coating. Figure 5.14 shows the double-layer coating by a micro pipette.

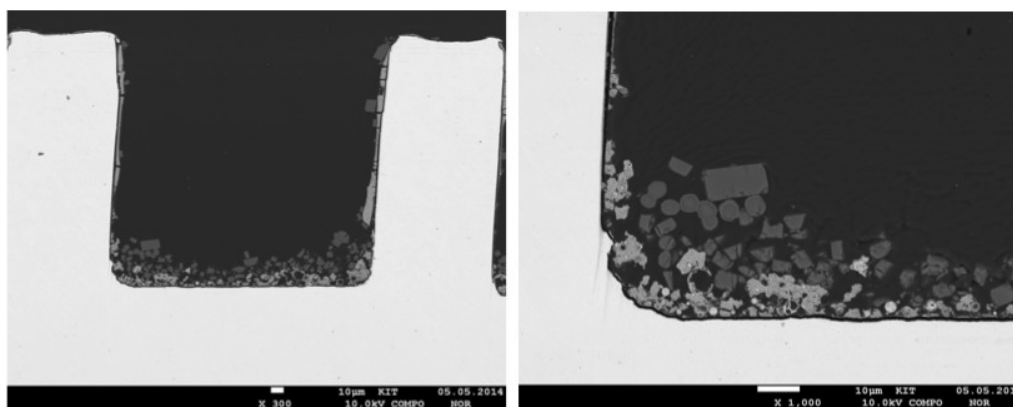


Figure 5.14.: Cross-sectional images of the micro pipette-coated double-layer (DLP) in one microchannel. Dark grey particles are H-ZSM-5, light grey particles represent CZA.

Even if the same catalyst inks and drying procedures were applied, the double-layer was not formed properly. A dense H-ZSM-5 top layer could not be established and the coating adhesion was poor. Therefore, it is demonstrated that inkjet printing is able to carry out complex catalyst coatings in confined space.

5.2. Direct DME synthesis in microchannel reactors

5.2.1. Activity of the double-layer catalyst

The established double-layer catalysts were applied for direct DME synthesis. As mentioned in the above section, three different double-layer catalysts were tested. While the mass and the nominal thickness of the CZA layer were maintained, the thickness of the H-ZSM-5 layer was varied between 3 μm (DL3) and 1 μm (DL1) by inkjet printing (Figure 5.15). DL1 had a 1 μm thin H-ZSM-5 layer at the bottom of the microchannel, but the H-ZSM-5 layer at its side walls was a little thicker. The mass of H-ZSM-5 for DL1 was one third of that for DL3. This shows that inkjet printing can well control the catalyst amount and layer thickness with rather homogeneous distribution. In case of the double-layer catalyst prepared by the micro

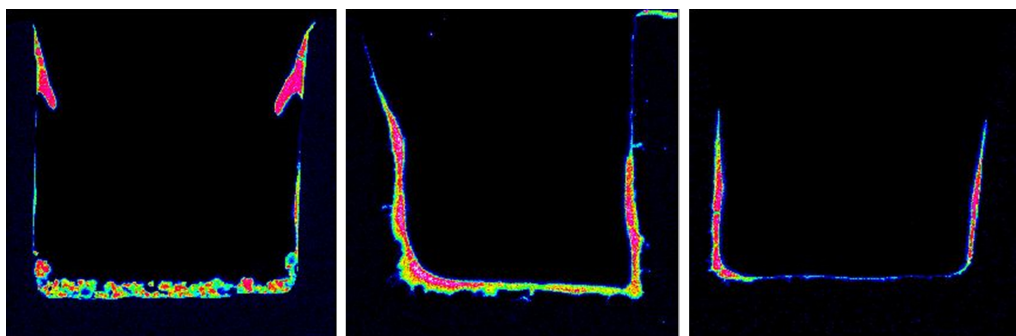


Figure 5.15.: Elemental level map of Si in cross-sectional images of the different double-layer catalysts. DLP (left); DL3 (middle); DL1 (right). Intensity of elemental level: red (high) to blue (low).

Table 5.5.: Comparison of double-layer catalysts.

| | Pipette coating* (DLP) | Printed ~ 3 μm top layer (DL3) | Printed ~ 1 μm top layer (DL1) |
|--|---------------------------|---|---|
| Total mass of double-layer in reactor (mg) | 485.1 - | 557.5 (± 4.1) | 390.1 (± 3.1) |
| Total mass of H-ZSM-5 in reactor (mg) | 90.6 - | 161.4 (± 2.0) | 59.4 (± 0.4) |
| Mass ratio (CZA/H-ZSM-5) | 7.3 | 2.5 | 5.6 |

*The mass of DLP may contain large error due to the low adhesion.

pipette coating (DLP), the same amounts of CZA and H-ZSM-5 ink as those for DL3 were used, and the same drying method was applied. However, the measured mass of the catalysts differed from DL3. The adhesion of the layers for DLP was poor so that much of the catalysts was lost after the drying. The comparison of catalyst amounts after weighing is shown in Table 5.5. The coating shape was also different. The ZSM-5 layers for DLP was characterized by many defects in a rather thick layer. Protruded catalyst particles were visible at the top of the side wall. Due to the low reliability of DLP catalyst in terms of the catalyst mass, activity comparison was not performed in this thesis.

Figure 5.16 shows the direct DME synthesis reaction results of DL3 and

DL1. The CO conversion trend as a function of reaction temperature was as expected; conversion increased with increasing temperature. However, DME was not the main product. Its selectivity was remained below 5 %. Instead, aliphatic hydrocarbons were observed, especially saturated hydrocarbons and methane (these compounds are lumped here to "hydrocarbons"). Both DL3 and DL1 showed high hydrocarbon selectivity. In both cases, the methanol selectivity was about 25 % at 215 °C being reduced down to 5 % upon increasing the reaction temperature. CO₂ was also observed here. In case of DL3 CO₂ and hydrocarbon selectivities at 215 °C were out of the trend. Due to low conversion at this temperature the relative error was large. The CO₂ selectivity increased along the temperature with DL3, but DL1 showed a more or less constant value.

In order to compare the activity of catalyst, the CO reaction rate was calculated (Figure 5.17). With temperature increasing the reaction rate increased. DL1 showed higher reaction rate than DL3. Since the first CO conversion takes place at the bottom layer, a diffusion limitation through the H-ZSM-5 layer could be considered.

Figure 5.18 shows selectivities of hydrocarbons. DL3 and DL1 showed different selectivity trend as a function of reaction temperature. All hydrocarbon selectivities with DL3 gradually decreased when the temperature increased except for 215 °C. However, DL1 showed that most hydrocarbon selectivities increased with temperature increasing. DL3 and DL1 showed a little difference in the major hydrocarbon products. Methane was the major product with DL3, but propane was the major production with DL1 below 290 °C. The product order was mostly the same at all temperatures for both catalysts. Both catalysts commonly produced only saturated hydrocarbons.

5.2.2. Investigation of hydrocarbon formation in the double-layer catalyst

Due to the undesired result, an additional investigation was carried out to better know the hydrocarbon formation. With a view to catalyst

material, H-ZSM-5 is more related to hydrocarbon formation. Therefore, a microchannel reactor with H-ZSM-5 catalyst (from the H-ZSM-5 ink prepared) was used to examine the methanol conversion. The same amount of H-ZSM-5 as for DL3 was coated into the microchannel by the pipette coating method. Methanol was fed as the only reactant. Figure 5.19 shows the reaction result as a function of reaction temperature. Methanol was well converted to DME at temperatures below 230 °C, typical methanol dehydration conditions. By increasing the temperature, the DME selectivity was dramatically reduced and hydrocarbon production was initiated. When the temperature reached over 270 °C, hydrocarbons became the main products. The temperature was increased above 300 °C and nearly no DME was observed. This demonstrated the typical methanol to hydrocarbon reaction over H-ZSM-5. Olefin production from methanol by H-ZSM-5 catalyst is quite common (350 - 600 °C and 1 - 6 bar; UOP/Hydro MTO process) [199].

Figure 5.20 shows the distribution of hydrocarbons at each reaction temperature. At 245 °C most of the products were light olefins. As the temperature increased, higher carbon number products were observed. When the temperature was 300 °C, saturated hydrocarbons appeared and the selectivity toward ethylene and propylene was decreased. From this observation, the effect of temperature on product selection can be known.

The actual circumstance in the direct DME synthesis from syngas with double-layer catalysts is syngas-rich condition, which means that the partial pressure of hydrogen is high. The presence of hydrogen can probably accelerate the production of saturated hydrocarbons. With this reason, hydrogen was fed together with methanol. As shown in Figure 5.21, the trend regarding conversion and selectivity was similar to Figure 5.19. Above 260 °C hydrocarbons were produced instead of DME. Unlike for pure methanol feeding, the DME selectivity remained about 15 % even at 350 °C. Further investigations were performed with CO and CO₂ in addition to the above condition. However, the trend was not changed much (Figure A.8 and A.9).

Figure 5.22 shows the hydrocarbon distribution at 350 °C for three different feed compositions. Each condition showed a different product distribution. When methanol was the only reactant (Figure 5.22 (black)), a high amount of C₄ hydrocarbons was found. Methane and olefins were also shown. When hydrogen was fed together with methanol (Figure 5.22 (red)),

saturated hydrocarbons were increased and olefins were diminished. On the other hand, when CO and CO₂ were fed together with hydrogen (the syngas mixture), the selectivity for olefins was increased again (Figure 5.22 (blue)).

From the above experiments it was revealed that the reaction temperature and gas composition can influence the methanol conversion. The conversion to hydrocarbons takes place at high temperature. Moreover, a hydrogen-rich environment induces saturation of olefins.

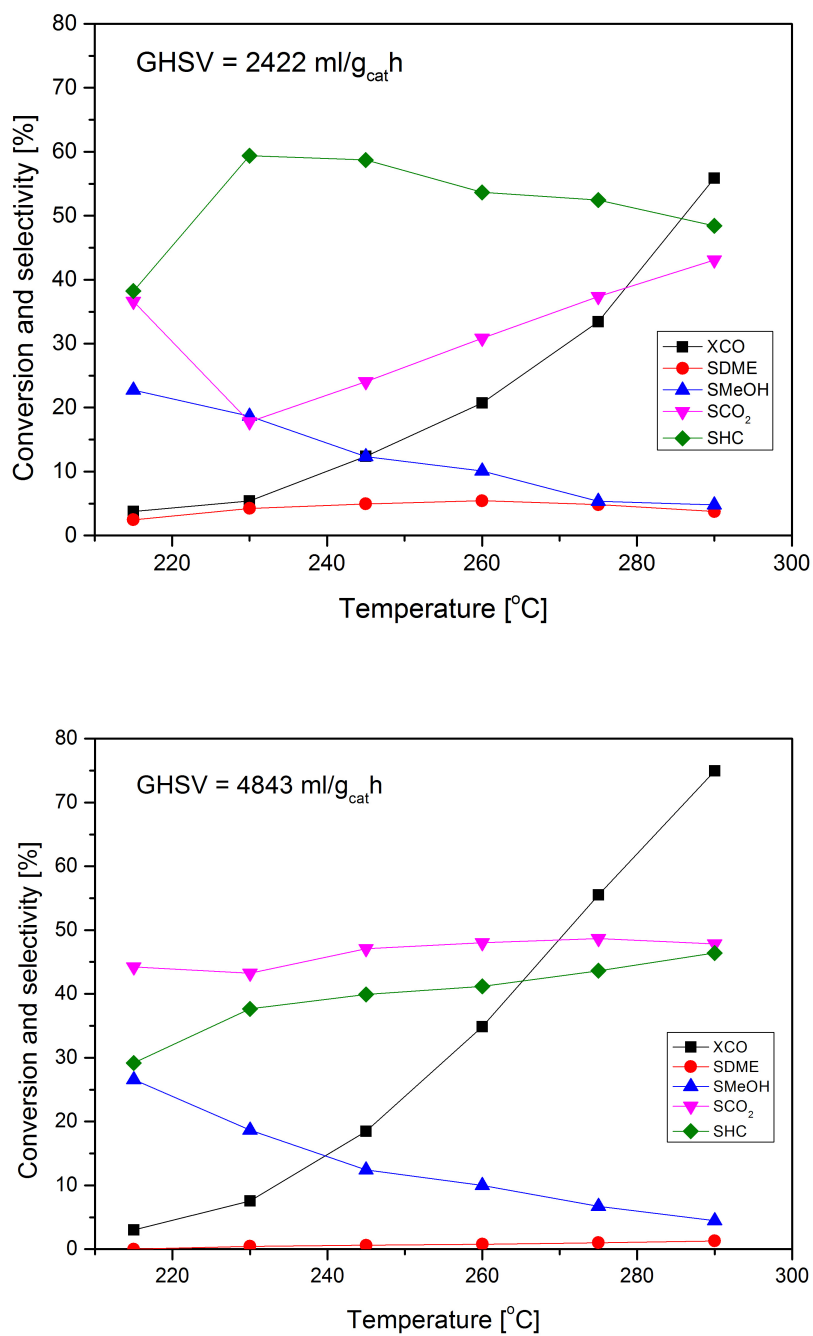


Figure 5.16.: Conversion and selectivity of the DME synthesis reaction over DL3 (top) and DL1 (bottom) in the microchannel reactor as a function of reaction temperature. $p = 40$ bar.

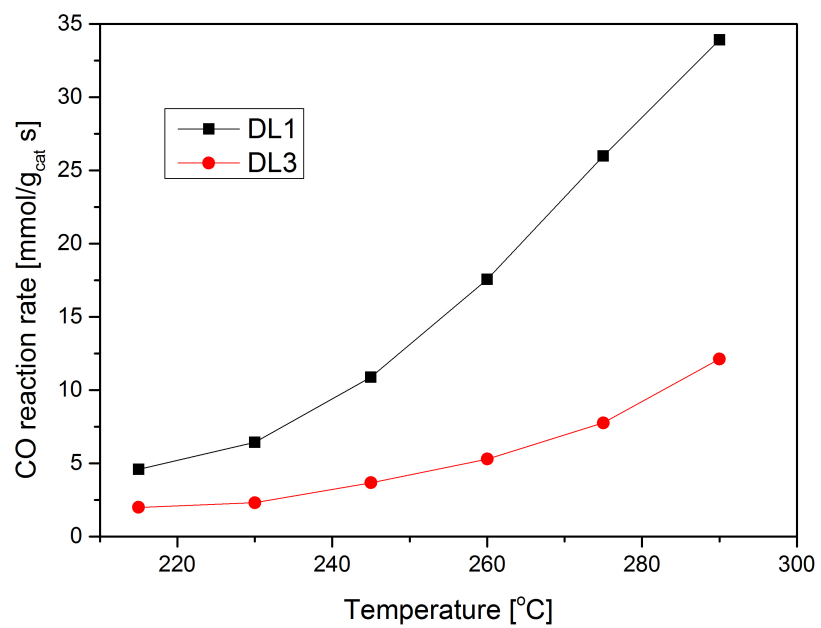


Figure 5.17.: CO reaction rate as a function of reaction temperature. $p = 40$ bar.

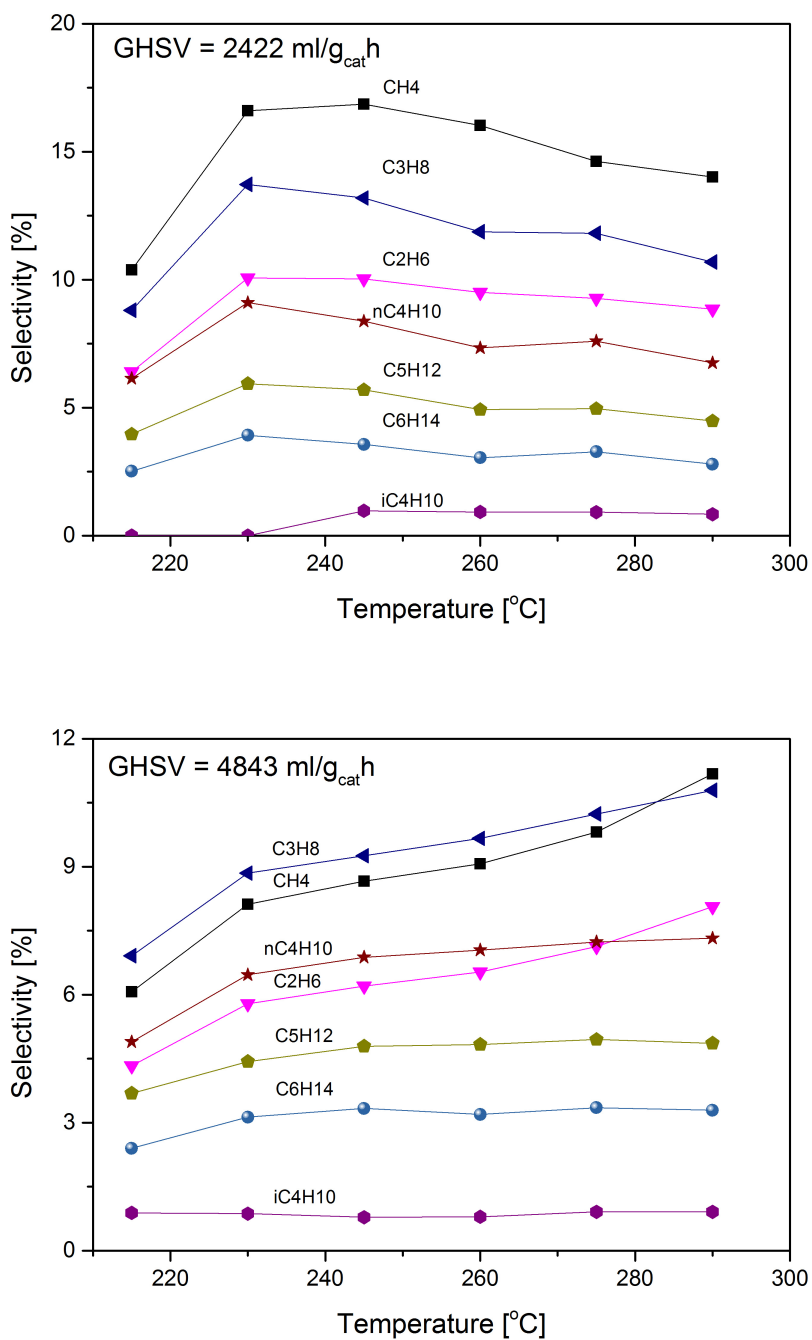


Figure 5.18.: Selectivity of hydrocarbons as a function of reaction temperature. DL3 (top) and DL1 (bottom) p = 40 bar.

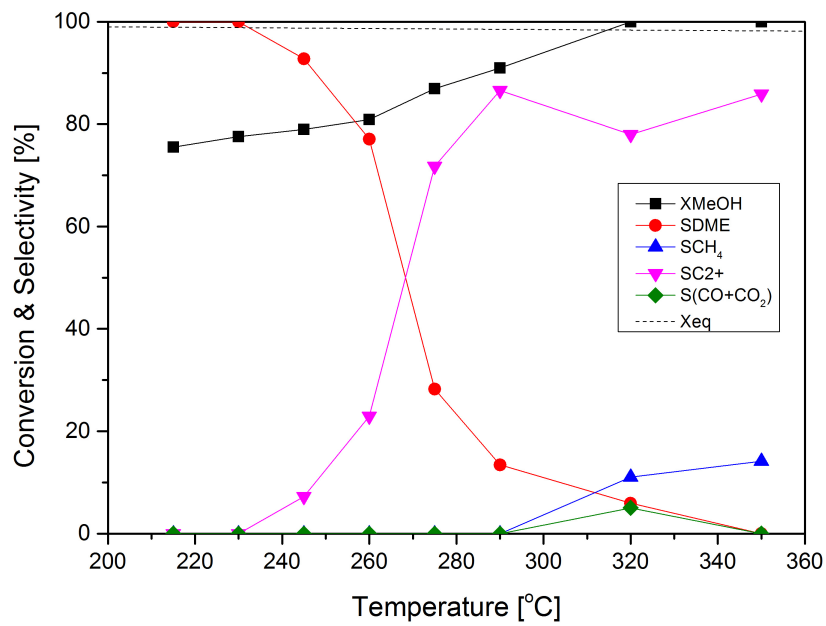


Figure 5.19.: Conversion and selectivity of methanol dehydration over H-ZSM-5 layer in the microchannel reactor. $p = 40$ bar; $N_2:MeOH = 50:0.3$. The equilibrium conversion values (X_{eq}) were calculated with the HSC[®] Software.

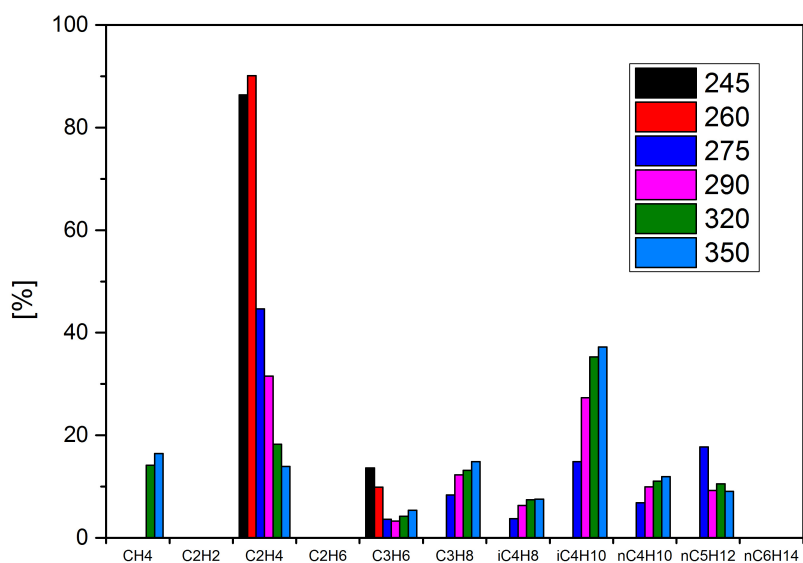


Figure 5.20.: Hydrocarbon distribution in methanol dehydration over H-ZSM-5 layer in the microchannel reactor with different reaction temperature. $p = 40$ bar; $N_2:MeOH = 50:0.3$.

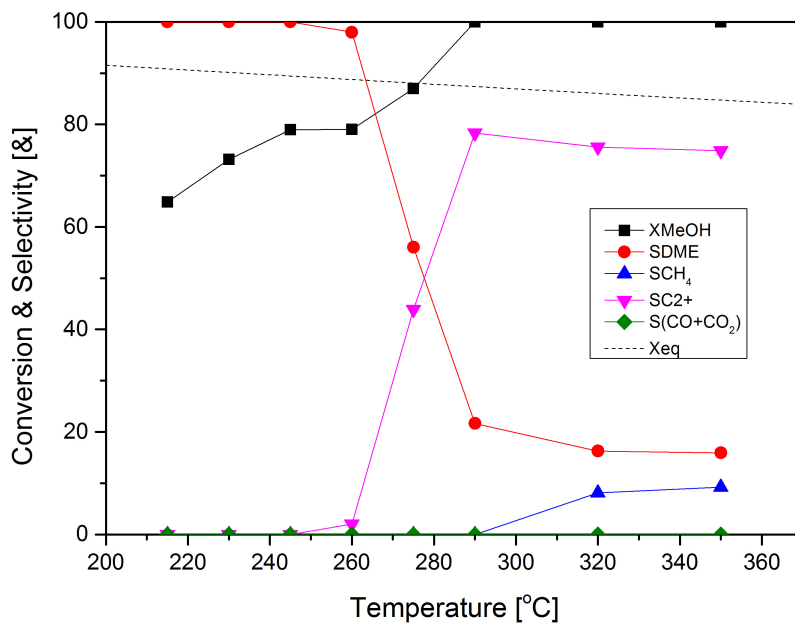


Figure 5.21.: Conversion and selectivity of methanol dehydration over H-ZSM-5 layer in the microchannel reactor as a function of reaction temperature. $p = 40$ bar; $N_2:MeOH:H_2 = 50:0.3:20$. The equilibrium conversion values (X_{eq}) were calculated with the HSC[®] Software.

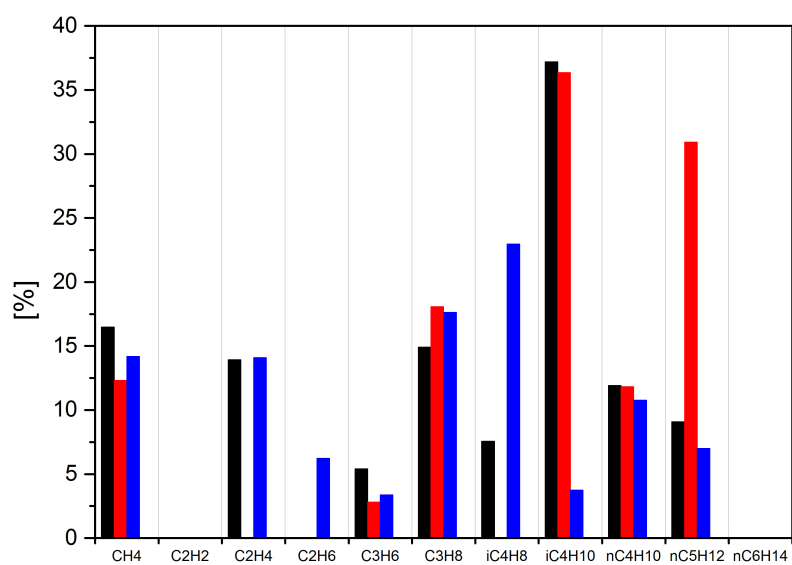


Figure 5.22.: Comparison of hydrocarbon distribution with different feeding composition. $p = 40$ bar; $T = 350$ °C, Black: $N_2:MeOH = 50:0.3$. Red: $N_2:MeOH:H_2 = 50:0.3:20$, Blue: $N_2:MeOH:H_2:CO:CO_2 = 50:0.3:5:5:2$

6. Conclusion and outlook

In order to take advantage of a microstructured reactor for DME synthesis, a bifunctional catalyst of CZA and ZSM-5 in microchannel reactor has been studied. This idea aims at an efficient DME synthesis process. With high heat exchange rate, the life of catalysts is able to be prolonged as well as safe operation and enhancement of reaction efficiency are expected. The combination of CZA and ZSM-5 catalysts to form a bifunctional catalyst has been already reported in former research reports. Nevertheless, proper introduction of bifunctional catalysts in microchannel reactors was still a challenging task, and in this thesis well ordered bifunctional formation of two catalysts in double-layer shape was shown.

Overall, this study can be divided into three parts; CZA catalyst production, catalyst coating for double-layer formation and direct DME synthesis in microchannel reactor with double-layer catalyst. Accordingly, the conclusion for each part will be described.

– CZA synthesis via flame spray pyrolysis

FSP enabling fast and simple nanoparticle synthesis was applied for the synthesis of CZA nanocatalyst to be used in inkjet printing. Since the selection of metal precursor is one of the most influential parameter in FSP, two types, nitrate and organometallic precursors, have been employed and compared. The nitrate metal precursor gave a CZA catalyst having a higher copper surface area. This result was carried over into direct DME synthesis with H-ZSM-5. The CZA catalyst from the nitrate metal precursor showed better catalytic activity than for the organometallic precursor. In our observation of CZA synthesis via FSP, the organometallic precursor have been favored to obtain high BET surface area as the previous reports have mentioned. However, the nitrate precursor is preferred to obtain the CZA catalyst with high surface area of active sites. This study confirmed that the

selection of precursors influences the number of active sites that is linked to the catalytic activity.

Among the CZA catalyst from the nitrate precursor, A631 showed the best activity and at high temperature. Its catalytic performance almost reached that of a commercial catalyst. On the other hand, the final DME selectivity showed less correlation with the activity of CZA. All catalysts presented a similar DME selectivity although the CO conversion was different. In addition, it was demonstrated that a Cu/Zn ratio of 2 is close to optimum. The FSP study supports the usage of FSP in CZA catalyst production as an alternative method beside conventional synthesis methods such as co-precipitation. There are a few research articles about FSP for CZA catalyst synthesis. CZA is still a controversial catalyst in terms of intrinsic active sites. Therefore, following points can be suggested for further development of FSP synthesized CZAs.

✓ Co-relation between copper surface area and metal precursor should be clarified.

✓ Thorough comparison between FSP and conventional methods for CZA catalyst can give a hint for the improvement of the FSP process in order to obtain high activity.

✓ Direct catalyst coating into microchannel during FSP process could provide a reduction of the preparation time.

– Inkjet printing for double-layer coating in microchannel reactor

The inkjet printing was studied for precise and fine-controlled catalyst coating in microchannels. Here it has been successfully applied for this purpose. Since the generated drops are small ($\leq 100 \mu\text{m}$ diameter) and adjustable, catalyst inks can be precisely deposited in the confined microchannels.

Beside the printing of inks, some preparation steps must be optimized such as ink formulation and operation parameters. In this study, the proper formulation of CZA and H-ZSM-5 ink was proposed. Selection of solvent, particle size regulation, usage of additives for particle stabilization and the Z number were investigated. The results can be relevant also to other catalyst systems.

The printing in microchannels with an alumina colloidal ink was

investigated as a preliminary study. Semicircular and rectangular shape microchannels showed different coating behavior. On semicircular microchannels, layers with uniform thickness could be obtained. However, rectangular microchannels showed a difficulty in uniform thickness at the bottom and side walls. When the prepared ink is not optimized, the coffee ring phenomenon was shown. The coffee ring cannot be neglected in film deposition in confined geometries like open microchannels. It was also found that the coffee ring effect is also relying on the drying process.

The introduction of inkjet printing has elevated fabrication of catalyst layers in microchannels with high variability. Even if this thesis has only demonstrated a straight line printing, multiple patterning can be established. Thus, inkjet printing can be applied to any shape of microchannel. Current printing technology is not limited to 2D surfaces. Three dimensional catalyst structures in microchannels are feasible as well. Printing industry and technology are rapidly developing and it can be grafted on chemical reactions.

- Direct DME synthesis in microchannel reactors with double-layer catalysts

The pre-studied catalyst printing was well exploited for the coating of double-layer catalysts in microchannels. The thickness control has been feasible by inkjet printing. The comparison of DL3 and DL1 showed the effect of the top layer (H-ZSM-5) thickness. In the studied reaction condition, the reaction rate was influenced by the top layer thickness. However, selectivity toward DME was not successfully achieved in both catalysts. Hydrocarbons were produced instead of DME. Hence, investigations about the hydrocarbon formation were required. As an experimental approach, methanol dehydration was carried out with the sole H-ZSM-5 layer in a microchannel reactor to understand the effect of H-ZSM-5 on the hydrocarbon formation. Through this study, heat and environment, i.e., gas composition around the catalyst were identified to affect hydrocarbon formation from methanol. One hypothesis can be raised regarding the heat. The methanol synthesis and methanol dehydration are exothermic reactions. The reaction rates of both reactions are high at the catalyst surface where the reactants are rich. This place is the interface of the CZA and ZSM-5 layer that is the middle of the double-layer catalyst. The reaction heat generated there will be transferred not only

to the microchannel wall but also to the gas flow through the ZSM-5 layer. Therefore, the ZSM-5 can have higher temperature and induce the conversion of DME to hydrocarbon.

An alteration of catalysts can also be considered, since many treatments have been done for the double-layer coating. Although the blank test of the microchannel reactor did not show any conversion, iron from the reactor with CZA can be a new catalyst. It is reported that copper can be a promoter of iron catalysts to enhance the activity and selectivity for Fischer-Tropsch and syngas to olefin production. [200, 201].

When Lewis acid sites in zeolite are strong, hydrocarbon formation can be enhanced [76]. Therefore, a thorough investigation of the ZSM-5 ink regarding Lewis acidity should be carried out.

The double-layer concept did not give proper DME production from syngas. However, we may look into this result with another point of view. For example, other products could be a desired goal. The double-layer catalyst produced relatively high amounts of C3 and C4 hydrocarbons. These are compounds of liquefied petroleum gas (LPG) and a lot of research has been reported on its synthesis from syngas [202–205]. The bi-functional catalyst of CZA and zeolite plays an important role in this process [204]. Therefore, with some modification such as reaction condition and zeolite promotion, the double-layer can be used for this reaction.

Bibliography

- [1] J. Kopyscinski, T. J. Schildhauser, and S. M. A. Biollaz. Production of synthetic natural gas (SNG) from coal and dry biomass - A technology review from 1950 to 2009. *Fuel*, 89:1763–1783, 2010.
- [2] S. Czernik and A. V. Bridgwater. Overview of applications of biomass fast pyrolysis oil. *Energy & Fuels*, 18:590–598, 2004.
- [3] S. Amin. Review on biofuel oil and gas production processes from micro algae. *Energy Conversion and Management*, 50:1834–1840, 2009.
- [4] D. A. Bulushev and J. R. H. Ross. Catalysis for conversion of biomass to fuels via pyrolysis and gasification: A review. *Catalysis Today*, 171:1–13, 2011.
- [5] M. E. Dry. The Fischer-Tropsch process: 1950-2000. *Catalysis Today*, 71:227–241, 2002.
- [6] M. Higo and K. Dowaki. A life cycle analysis on a Bio-DME production system considering the species of biomass feedstock in Japan and Papua New Guinea. *Applied Energy*, 87:58–67, 2010.
- [7] Regulation (EC) No 715/2007 of the european parliament and of the council of 20 June 2007. *Official Journal of the European Union*, 2007.
- [8] BP Statistical review 2014 workbook. <http://www.bp.com/en/global/corporate/about-bp/energy-economics/statistical-review-of-world-energy/statistical-review-downloads.html>, 2014. Accessed: 2015-03-04.
- [9] World Health Organization. Exposure to particulate matter with an aerodynamic diameter of 10 μm or less (PM10) in urban areas 2008-2013, 2014.

- [10] P. Pfeifer. Application of catalysts to metal microreactor systems. In V. Patel, editor, *Chemical Kinetics*, book section 15. INTECH, 2012.
- [11] F. Hayer. *Direct synthesis of dimethyl ether in microstructured reactors*. Thesis, Norwegian University of Science and Technology, 2011.
- [12] G. H. Yang, N. Tsubaki, J. Shamoto, Y. Yoneyama, and Y. Zhang. Confinement effect and synergistic function of H-ZSM-5/Cu-ZnO-Al₂O₃ capsule catalyst for one-step controlled synthesis. *Journal of the American Chemical Society*, 132(23):8129–8136, 2010.
- [13] H. Jiang, H. Bongard, W. Schmidt, and F. Schüth. One-pot synthesis of mesoporous Cu- γ -Al₂O₃ as bifunctional catalyst for direct dimethyl ether synthesis. *Microporous and Mesoporous Materials*, 164:3–8, 2012.
- [14] G. Bonura, M. Cordaro, C. Cannilla, A. Mezzapica, L. Spadaro, F. Arena, and F. Frusteri. Catalytic behavior of a bifunctional system for the one step synthesis of DME by CO₂ hydrogenation. *Catalysis Today*, 228:51–57, 2014.
- [15] J. Sun, G. H. Yang, Q. X. Ma, I. Ooki, A. Taguchi, T. Abe, Q. Xie, Y. Yoneyama, and N. Tsubaki. Fabrication of active Cu-Zn nanoalloys on H-ZSM5 zeolite for enhanced dimethyl ether synthesis via syngas. *Journal of Materials Chemistry A*, 2(23):8637–8643, 2014.
- [16] P. Pfeifer, A. Wenka, K. Schubert, M. A. Liauw, and G. Emig. Characterization of flow distribution in microchannel reactors. *Aiche Journal*, 50(2):418–425, 2004.
- [17] Dymel® A propellant toxicity summary - Technical information ATS-1. http://www2.dupont.com/Dymel_Propellants/en_US/assets/downloads/h04236_Dymel_A_toxicity_summary.pdf. Accessed: 2015-03-04.
- [18] D. Lee, J. S. Lee, H. Y. Kim, C. K. Chun, S. C. James, and S. S. Yoon. Experimental study on the combustion and NO_x emission characteristics of DME/LPG blended fuel using counterflow burner. *Combustion Science and Technology*, 184(1):97–113, 2012.

- [19] Toshiyuki Mii and Masayuki Uchida. Fuel DME plant in East Asia. *15th Saudi-Japan Joint Symposium*, November 27-28, 2005.
- [20] M. C. Lee, S. Bin Seo, J. H. Chung, Y. J. Joo, and D. H. Ahn. Industrial gas turbine combustion performance test of DME to use as an alternative fuel for power generation. *Fuel*, 88(4):657–662, 2009.
- [21] C. Arcoumanis, C. Bae, R. Crookes, and E. Kinoshita. The potential of di-methyl ether (DME) as an alternative fuel for compression-ignition engines: A review. *Fuel*, 87(7):1014–1030, 2008.
- [22] J. B. Hansen and S.-E. Mikkelsen. DME as a transportation fuel. Report, Haldor Topsøe A/S, July 2001 2001.
- [23] L. Plass, H. J. Wernicke, and F. Schmidt. Synthesis gas generation - general aspects. In M. Bertau, F. Schmidt, H. Offermanns, H.-J. Wernicke, and L. Plass, editors, *Methanol: the basic chemical and energy feedstock of the future*, book section 4.2, page 72. Springer-Verlag Berlin Heidelberg, 2014.
- [24] T. Wurzel. Lurgi MegaMethanol Technology - Delivering the building blocks for future fuel and monomer demand. *The DGMK conference "Synthesis Gas Chemistry"*, 2006.
- [25] J. Richard and Rostrup-Nielsen. Steam reforming. In G. Ertl, H. Knözinger, F. Schüth, and J. Weitkamp, editors, *Handbook of heterogeneous catalysis*, pages 2248–2264. Wiley-VCH Verlag GmbH & Co. KGaA., 2008.
- [26] G. Olah, A. Goepfert, and G. K. Surya Prakash. *Beyond oil and gas: The methanol economy*. Wiley-VCH Verlag GmbH & Co. KGaA., Germany, 2009.
- [27] Hydrogen production by steam reforming. <https://chemeng-processing.blogspot.de/2010/05/hydrogen-production-by-steam-reforming.html>, 2010. Accessed: 2015-09-11.
- [28] H. Offermanns, L. Plass, and R. Heyde. Methanol in industrial chemistry (General). In Martin Bertau, Friedrich Schmidt, Heribert Offermanns, Hans-Jürgen Wernicke, and Ludolf Plass, editors,

Methanol: the basic chemical and energy feedstock of the future, book section 1.4, page 14. Springer-Verlag Berlin Heidelberg, 2014.

- [29] K. Aasberg-Petersen, I. Dybkjær, C. V. Ovesen, N. C. Schjødt, J. Sehested, and S. G. Thomsen. Natural gas to synthesis gas - Catalysts and catalytic processes. *Journal of Natural Gas Science and Engineering*, 3:423–459, 2011.
- [30] P. K. Bakkerud. Update on synthesis gas production for GTL. *Catalysis Today*, 106:30–33, 2005.
- [31] T. V. Choudhary and V. R. Choudhary. Energy-Efficient syngas production through catalytic ox-methane reforming reactions. *Angewandte Chemie International Edition*, 47:1828–1847, 2008.
- [32] A. G. Peres, B. H. Lunellia, and R. M. Filhoa. Application of biomass to hydrogen and syngas production. *Chemical Engineering Transactions*, 32:589–594, 2013.
- [33] D. Johnson. Global methanol market review. Technical report, IHS Inc. 2012.
- [34] M. Berggren. Global methanol outlook: Capacity calling. *16th IMPCA Asian Methanol Conference - Singapore*, October 30 - November 1, 2013.
- [35] J. Hansen and P. E. H. Nielsen. Methanol synthesis. In G. Ertl, H. Knözinger, F. Schüth, and J. Weitkamp, editors, *Handbook of heterogeneous catalysis*, pages 2920–2949. Wiley-VCH Verlag GmbH & Co. KGaA., 2008.
- [36] Methanex investor presentation. [https://www.methanex.com/sites/default/files/investor/IR-Presentation-Aug\\$\%202014_v1.pdf](https://www.methanex.com/sites/default/files/investor/IR-Presentation-Aug$\%202014_v1.pdf), 2014. Accessed: 2015-09-14.
- [37] H. Holm-Lasen. Synthesis and new applications of DME - a review of alternatives. *8th Natural Gas Conversion Symposium - Natal, Brazil*, May 27 - 31, 2007.
- [38] Indirect DME production technology. <https://www.toyo-eng.com/jp/en/products/energy/dme/>. Accessed: 5 July 2015.

- [39] A. A. Kiss, D. J-P. C. Suszwalak, and R. M. Ignat. Process intensification alternatives in the DME production. *Chemical Engineering Transactions*, 35:91–96, 2013.
- [40] Production process DME. https://www.akzonobel.com/ic/products/dimethyl_ether/production_process/. Accessed: 4 May 2015.
- [41] K. L. Ng, D. Chadwick, and B. A. Toseland. Kinetics and modelling of dimethyl ether synthesis from synthesis gas. *Chemical Engineering Science*, 54:3587–3592, 1999.
- [42] W.-Z. Lu, L.-H. Teng, and W.-D. Xiao. Simulation and experiment study of dimethyl ether synthesis from syngas in a fluidized-bed reactor. *Chemical Engineering Science*, 59:5455–5464, 2004.
- [43] I. Iliuta, F. Larachi, and P. Fongarland. Dimethyl ether synthesis with in situ H₂O removal in fixe-bed membrane reactor: model and simulation. *Chemical Engineering Science*, 54:3587–3592, 1999.
- [44] G. Moradi, J. Ahmadpour, M. Nazari, and F. Yaripour. Effects of feed composition and space velocity on direct synthesis of dimethyl ether from syngas. *Industrial & Engineering Chemistry Research*, 47(20):7672–7679, 2008.
- [45] S. Tauro. *One-step synthesis of dimethyl ether using microreactors*. Thesis, Karlsruhe Institute of Technology, 2014.
- [46] W. Cho and S.-S. Kim. Current status and technical development for di-methyl ether as a new and renewable energy. *Journal of the Korean Industrial and Engineering Chemistry*, 20(4):355–362, 2009.
- [47] Y. Ohno, H. Yagi, N. Inoue, K. Okuyama, and S.i Aoki. Slurry phase DME direct synthesis technology -100 tons/day demonstration plant operation and scale up study. *Studies in Surface Science and Catalysis*, 167:403–408, 2007.
- [48] Y. Baek, W. Cho, and H. C. Lee. The status of DME development and utilization as a fuel. *Korean Industrial Chemistry News*, 13(2):1–11, 2010.
- [49] W. Cho. KOGAS DME activities for commercialization. In *7th Asian DME conference*, 2011.

- [50] J. Yoshihara, S. C. Parker, A. Schafer, and C. T. Campbell. Methanol synthesis and reverse water-gas shift kinetics over clean polycrystalline copper. *Catalysis Letters*, 31(4):313–324, 1995.
- [51] I. A. Fisher, H. C. Woo, and A. T. Bell. Effects of zirconia promotion on the activity of Cu/SiO₂ for methanol synthesis from CO/H₂ and CO₂/H₂. *Catalysis Letters*, 44(1-2):11–17, 1997.
- [52] M. Behrens, F. Studt, I. Kasatkin, S. Kuhl, M. Havecker, F. Abild-Pedersen, S. Zander, F. Girgsdies, P. Kurr, B. L. Kniep, M. Tovar, R. W. Fischer, J. K. Nørskov, and R. Schlögl. The active site of methanol synthesis over Cu/ZnO/Al₂O₃ industrial catalysts. *Science*, 336(6083):893–897, 2012.
- [53] M. W. E. van den Berg, S. Polarz, O. P. Tkachenko, K. V. Klementiev, M. Bandyopadhyay, L. Khodeir, H. Gies, M. Muhler, and W. Grünert. Cu/ZnO aggregates in siliceous mesoporous matrices: Development of a new model methanol synthesis catalyst. *Journal of Catalysis*, 241:446–455, 2006.
- [54] J.-D. Grunwaldt, A. M. Molenbroek, N.-Y. Topsøe, H. Topsøe, and B. S. Clausen. In situ investigations of structural changes in Cu/ZnO catalysts. *Journal of Catalysis*, 194:452–460, 2000.
- [55] G.C. Chinchin, P.J. Denny, D.G. Parker, M.S. Spencer, and D.A. Whan. Mechanism of methanol synthesis from CO₂/CO/H₂ mixtures over copper/zinc oxide/alumina catalysts: use of ¹⁴C-labelled reactants. *Applied Catalysis*, 30(2):333–338, 1987.
- [56] K.G. Chanchlani, R.R. Hudgins, and P.L. Silveston. Methanol synthesis from H₂, CO, and CO₂ over Cu/ZnO catalysts. *Journal of Catalysis*, 136(1):59–75, 1992.
- [57] P. Nowak, M. Lachowska, and J. Skrzypek. Influence of water vapour on methanol synthesis over CuO/ZnO/Al₂O₃ catalyst. *Chemical Engineering Science*, 46:3324–3325, 1991.
- [58] J.S. Lee, K.H. Lee, S.Y. Lee, and Y.G. Kim. A comparative study of methanol synthesis from CO₂/H₂ and CO/H₂ over a Cu/ZnO/Al₂O₃ catalyst. *Journal of Catalysis*, 144:414–424, 1993.

- [59] F. Studt, I. Sharafutdinov, F. Abild-Peerse, Elkjær C. F., Hummelshøj J. S., S. Dahl, I. Chorkendorf, and J. K. Nørskov. Discovery of a Ni-Ga catalyst for carbon dioxide reduction to methanol. *Nature Chemistry*, 6:320–324, 2014.
- [60] P. Gao, F. Li, H. Zhan, N. Zhao, F. Xiao, W. Wei, L. Zhong, H. Wang, and Y. Sun. Influence of Zr on the performance of Cu/Zn/Al/Zr catalysts via hydrotalcite-like precursors for CO₂ hydrogenation to methanol. *Journal of Catalysis*, 298:51–60, 2013.
- [61] J. Graciani, K. Mudiyansele, F. Xu, A. E. Baber, J. Evans, S. D. Senanayake, D. J. Stacchiola, P. Liu, J. Hrbek, J. F. Sanz, and J. A. Rodriguez. Highly active copper-curia and copper-curia-titania catalysts for methanol synthesis from CO₂. *Science*, 345:546–550, 2014.
- [62] T. Wurzel. MegaMethanol[®] Technology-Delivering the building blocks for the future. Fuel and Monomer demand. *Oil Gas European Magazine*, 2:92–96, 2007.
- [63] V. Gronemann, L. Plass, and F. Schmidt. Commercial methanol synthesis from syngas. In Martin Bertau, Friedrich Schmidt, Heribert Offermanns, Hans-Jürgen Wernicke, and Ludolf Plass, editors, *Methanol: the basic chemical and energy feedstock of the future*, book section 1.4, pages 234–266. Springer-Verlag Berlin Heidelberg, 2014.
- [64] E. C. Heydorn, V. E. Stein, P. J. A. Tijm, B. T. Street, and R. M. Kornosky. Liquid phase methanol (LPMeOH[™]) project operational experience. *the Gasification Technology Council Meeting in San Francisco*, 4-7 October, 1998.
- [65] M. Trueba and S. P. Trasatti. γ -Alumina as a support for catalysts: A review of fundamental aspects. *European Journal of Inorganic Chemistry*, 17:3393–3403, 2005.
- [66] K. W. Jun, H. S. Lee, H. S. Roh, and S. E. Park. Catalytic dehydration of methanol to dimethyl ether (DME) over solid-acid catalysts. *Bulletin of the Korean Chemical Society*, 23(6):803–806, 2002.

- [67] Y. C. Fu, T. Hong, J. P. Chen, A. Auroux, and J. Y. Shen. Surface acidity and the dehydration of methanol to dimethyl ether. *Thermochimica Acta*, 434(1-2):22–26, 2005.
- [68] L. G. Wang, Y. Qi, Y. X. Wei, D. R. Fang, S. H. Meng, and Z. M. Liu. Research on the acidity of the double-function catalyst for DME synthesis from syngas. *Catalysis Letters*, 106(1-2):61–66, 2006.
- [69] D. S. Mao, W. M. Yang, J. C. Xia, B. Zhang, Q. Y. Song, and Q. L. Chen. Highly effective hybrid catalyst for the direct synthesis of dimethyl ether from syngas with magnesium oxide-modified HZSM-5 as a dehydration component. *Journal of Catalysis*, 230(1):140–149, 2005.
- [70] J. Abu-Dahrieh, D. Rooney, A. Goguet, and Y. Saih. Activity and deactivation studies for direct dimethyl ether synthesis using CuOnO₂O₃ with NH₄ZSM-5, HZSM-5 or γ -Al₂O₃. *Chemical Engineering Journal*, 203:201–211, 2012.
- [71] M. Xu, J. H. Lunsford, D. W. Goodman, and A. Bhattacharyya. Synthesis of dimethyl ether (DME) from methanol over solid-acid catalysts. *Applied Catalysis A: General*, 149:289–301, 1997.
- [72] T. Takeguchi, K. Yanagisawa, T. Inui, and M. Inoue. Effect of the property of solid acid upon syngas-to-dimethyl ether conversion on the hybrid catalysts composed of Cuna and solid acids. *Applied Catalysis A: General*, 192:201–209, 2000.
- [73] V. Vishwanathan, K.-W. Jun, J.-W. Kim, and H.-S. Roh. Vapour phase dehydration of crude methanol to dimethyl ether over Na-modified H-ZSM-5 catalysts. *Applied Catalysis A: General*, 276:251–255, 2004.
- [74] A. Garcia-Trenco and A. Martinez. Direct synthesis of DME from syngas on hybrid CuZnAl/ZSM-5 catalysts: New insights into the role of zeolite acidity. *Applied Catalysis A: General*, 411:170–179, 2012.
- [75] E. Sarkadi-Priboczki, N. Kumar, T. Salmi, Z. Kovacs, and D. Y. Murzin. A novel radioisotope method for studying catalytic transformations over alumina, H-ZSM-5 and H-beta zeolite catalysts: investigation of conversion of C-11-labeled methanol to C-11-labeled dimethyl ether and hydrocarbons. *Catalysis Letters*, 93(1-2):101–107, 2004.

- [76] J. C. Xia, D. S. Mao, W. C. Tao, Q. L. Chen, Y. H. Zhang, and Y. Tang. Dealumination of HMCM-22 by various methods and its application in one-step synthesis of dimethyl ether from syngas. *Microporous and Mesoporous Materials*, 91(1-3):33–39, 2006.
- [77] J. W. Bae, H. S. Potdar, S. H. Kang, and K. W. Jun. Coproduction of methanol and dimethyl ether from biomass-derived syngas on a Cu-ZnO-Al₂O₃/gamma-Al₂O₃ hybrid catalyst. *Energy & Fuels*, 22(1):223–230, 2008.
- [78] K. Fujimoto, K. Asami, T. Shikada, and H. Tominaga. Selective synthesis of dimethyl ether from synthesis gas. *Chemistry Letters*, 12:2051–2054, 1984.
- [79] J. Hu, Y. Wang, C. Cao, D. C. Elliott, D. J. Stevens, and J. F. White. Conversion of biomass syngas to DME using a microchannel reactor. *Industrial & Engineering Chemistry Research*, 44:1722–1727, 2005.
- [80] Y. Zhang, Y. Yoneyama, and N. Tsubaki. Simultaneous introduction of chemical and spatial effects via a new bimodal catalyst support preparation method. *Chemical Communication*, pages 1216–1217, 2002.
- [81] J. Bao, J. He, Y. Zhang, Y. Yoneyama, and N. Tsubaki. A core/shell catalyst produces a spatially confined effect and shape selectivity in a consecutive reaction. *Angewandte Chemie International Edition*, 47:353–356, 2008.
- [82] R. Nie, H. Lei, S. Pan, L. Wang, J. Fei, and Z. Hou. Core-shell structured CuO-ZnO-HZSM-5 catalysts for CO hydrogenation to dimethyl ether. *Fuel*, 96:419–425, 2012.
- [83] R. Ahmad, D. Schrempp, S. Behrens, J. Sauer, M. Döring, and U. Arnold. Zeolite-based bifunctional catalysts for the single step synthesis of dimethyl ether from CO-rich synthesis gas. *Fuel Processing Technology*, 121:38–46, 2014.
- [84] Q. Li, C. Xin, and P. Lian. The synthesis and application of CuO-ZnO/HZSM-5 catalyst with core-shell structure. *Petroleum Science and Technology*, 30:2187–2195, 2012.

- [85] K. Schuber, J. Brandner, M. Fichtner, G. Linder, U. Schygulla, and A. Wenka. Microstructure devices for application in thermal and chemical process engineering. *Microscale Thermophysical Engineering*, 5:17–39, 2001.
- [86] L. Kiwi-Minsker and A. Renken. Microstructured reactors. In G. Ertl, H. Knözinger, F. Schüth, and J. Weitkamp, editors, *Handbook of heterogeneous catalysis*, pages 2248–2264. Wiley-VCH Verlag GmbH & Co. KGaA., 2008.
- [87] A. Gavriilidis, P. Angeli, E. Cao, K. K. Yeong, and Y. S. S. Wan. Technology and applications of micro engineered reactors. *Chemical Engineering Research and Design*, 80:3–30, 2002.
- [88] G. Kolb and V. Hessel. Micro-structured reactors for gas phase reactions. *chemical Engineering Journal*, 98(1-2):1–38, 2004.
- [89] K. Jähnisch, V. Hessel, H. Löwe, and M. Baerns. Chemistry in microstructured reactors. *Angewandte Chemie International Edition*, 43:406–446, 2004.
- [90] G. Markowz, S. Schirrmeister, J. Albrecht, F. Becker, R. Schütte, K. J. Caspary, and E. Klemm. Microstructured reactors for heterogeneously catalyzed gas-phase reactions on an industrial scale. *Chemical Engineering & Technology*, 28:459–464, 2005.
- [91] J. M. Commenge, L. Falk, J. P. Corriou, and M. Maltose. Optimal design for flow uniformity in microchannel reactors. *AIChE Journal*, 48:345–358, 2004.
- [92] G. Germani, A. Stefanescu, Y. Schuurman, and A. A. C. van Veen. Preparation and characterization of porous alumina-based catalyst coatings in microchannels. *Chemical Engineering Science*, 62:5084–5091, 2007.
- [93] R. Zapf, C. Becker-Willinger, K. Berresheim, H. Bolz, H. Gnaser, V. Hessel, G. Kolb, P. Löb, A.-K. Pannwitt, and A. Ziogas. Detailed characterization of various porous alumina-based catalyst coatings within microchannels and their testing for methanol steam reforming. *Chemical Engineering Research and Design*, 81:721–729, 2003.

- [94] R. Wunsch, M. Fichtner, O. Görke, K. Haas-Santo, and K. Schubert. Process of applying Al_2O_3 coating in microchannels of completely manufactured microstructured reactors. *Chemical engineering & Technology*, 25:700–703, 2002.
- [95] K. Haas-Santo, O. Görke, P. Pfeifer, and K. Schubert. Catalytic coatings for microstructure reactors. *Chimia*, 56:605–610, 2002.
- [96] Y. Suzuki, J. Saito, and N. Ksagi. Development of micro catalytic combustion with Pt/ Al_2O_3 thin films. *JSME International Journal Series B - Fluid and Thermal Engineering*, 47:522–527, 2005.
- [97] U. Ciesla and F. Schüth. Ordered mesoporous materials. *Microporous and Mesoporous Materials*, 427:131–149, 1999.
- [98] O. de la Iglesia, V. Sebastian, R. Mallada, G. Nikolaidis, J. Coronas, G. Kolb, R. Zapf, V. Hessel, and J. Santamaria. Preparation of Pt/ZSM-5 films on stainless steel microreactors. *Catalysis Today*, 125:2–10, 2007.
- [99] J. Bravo, A. Karim, T. Conant, G. P. Lopez, and A. Datye. Wall coating of CuO/ZnO/ Al_2O_3 methanol steam reforming catalyst for micro-channel reformers. *Chemical Engineering Journal*, 101:113–121, 2004.
- [100] Y. Men, H. Gnaser, R. Zapf, V. Hessel, and C. Ziegler. Parallel screening of Cu/ $\text{CeO}_2/\gamma\text{Al}_2\text{O}_3$ catalysts for steam reforming of methanol in a 10-channel micro-structured reactor. *Catalysis Communication*, 5:671–675, 2004.
- [101] Z. S. Rak and H. J. Veringa. Ceramic honeycombs coated with zeolite Co-ZSM-5 for NO_x abatement. *Reaction Kinetics and Catalysis Letters*, 60:303–312, 1997.
- [102] C. Ayrault, J. Barrault, N. Blin-Simiand, F. Jorand, S. Pasquiers, A. Rousseau, and J. M. Tatibouët. Oxidation of 2-heptanone in air by a DBD-type plasma generated within a honeycomb monolith supported Pt-based catalyst. *Catalysis Today*, 89:75–81, 2004.
- [103] R. J.-H., K.-Y. Lee, H. La, H.-J. Kim, J.-I. Yang, and H. Jung. Ni catalyst wash-coated on metal monolith with enhanced heat-transfer

- capability for steam reforming. *Journal of Power Sources*, 171:499–505, 2007.
- [104] P. Pfeifer, O. Görke, and K. Schubert. Washcoats and electrophoresis with coated and uncoated nanoparticles on microstructured metal foils and microstructured reactors. *Proceedings of the 6th International Conference on Microreaction Technology*, pages 281–285, 2002.
- [105] M. T. Janicke, H. Kestenbaum, U. Hagendorf, F. Schüth, M. Fichtner, and K. Schubert. The controlled oxidation of hydrogen from an explosive mixture of gases using a microstructured reactor/heat exchanger and Pt/Al₂O₃ catalyst. *Journal of Catalysis*, 191:282–293, 2000.
- [106] C. Cao, G. Xia, J. Holladay, E. Jones, and Y. Wang. Kinetic studies of methanol steam reforming over Pd/ZnO catalyst using a microchannel reactor. *Applied Catalysis A: General*, 262:19–29, 2004.
- [107] F. Hayer, H. Bakhtiary-Davijany, R. Myrstad, A. Holmen, P. Pfeifer, and H. J. Venvik. Synthesis of dimethyl ether from syngas in a microchannel reactor - Simulation and experimental study. *Applied Catalysis A: General*, 262:19–29, 2004.
- [108] G. D. Ulrich. Flame synthesis of fine particles. *Chemical & Engineering News*, 62:22–29, 1984.
- [109] W. J. Stark, K. Wegner, S. E. Pratsinis, and A. Baiker. Flame aerosol synthesis of vanadia-titania nanoparticles: Structural and catalytic properties in the selective catalytic reduction of NO by NH₃. *Journal of Catalysis*, 197:182–191, 2001.
- [110] T. Johannessen and S. Koutsopoulos. One-step flame synthesis of an active Pt/TiO₂ catalyst for SO₂ oxidation - A possible alternative to traditional methods for parallel screening. *Journal of Catalysis*, 205:404–408, 2002.
- [111] W. J. Stark, S. E. Pratsinis, and A. Baiker. Heterogeneous catalysis by flame-made nanoparticles. *CHIMIA*, 56:485–489, 2002.

- [112] W. Y. Teoh, R. Amal, and L. Mädler. Flame spray pyrolysis: An enabling technology for nanoparticles design and fabrication. *Nanoscale*, 2(8):1324–1347, 2010.
- [113] L. Mädler, H. K. Kammler, R. Mueller, and S. E. Pratsinis. Controlled synthesis of nanostructured particles by flame spray pyrolysis. *Journal of Aerosol Science*, 33(2):369–389, 2002.
- [114] L. Mädler, W. J. Stark, and S. E. Pratsinis. Flame-made cherry nanoparticles. *Journal of Materials Research*, 17:1356–1362, 2002.
- [115] R. Mueller, L. Mädler, and S. E. Pratsinis. Nanoparticle synthesis at high production rates by flame spray pyrolysis. *Chemical Engineering Science*, 58:1969–1976, 2003.
- [116] G. C. Chinchin, C. M. Hay, H. D. Vandervell, and K. C. Waugh. The measurement of copper surface-areas by reactive frontal chromatography. *Journal of Catalysis*, 103(1):79–86, 1987.
- [117] Micro-Berty catalyst testing reactor. http://www.autoclaveengineers.com/products/catalytic_reactors/micro_berty/index.html, 2015. Accessed: 2015-04-04.
- [118] B. C. Enger, J. Walmsley, E. Bjorgum, R. Lodeng, P. Pfeifer, K. Schubert, A. Holmen, and H. J. Venvik. Performance and SEM characterization of Rh impregnated microchannel reactors in the catalytic partial oxidation of methane and propane. *Chemical Engineering Journal*, 144(3):489–501, 2008.
- [119] V. Joshi, J.-P. Choi, J. Darsell, A. Meier, and K. Scott Weil. Reactive air aluminizing of Nicrofer-6025HT for use in advanced coal-based power plants. *Metallurgical and Materials Transactions A*, 44:1–5, 2012.
- [120] J. D. Morse, D. A. Sopchak, R. S. Upadhye, J. G. Reynolds, J. H. Satcher, and A. E. Gash. Catalyst for microelectromechanical systems microreactors, US 8057988 B2, 2011.
- [121] N. R. Peela and Deepak Kunzru. Oxidative steam reforming of ethanol over Rh based catalysts in a micro-channel reactor. *International Journal of Hydrogen Energy*, 36:3384–3396, 2011.

- [122] C.-C. Huang, Y.-J. Huang, H.-S. Wang, F.-G. Tseng, and Y.-C. Su. A well-dispersed catalyst on porous silicon micro-reformer for enhancing adhesion in the catalyst-coating process. *International Journal of Hydrogen Energy*, 39:7753–7764, 2014.
- [123] N.-K. Park, Y. B. Seong, M. J. Kim, Y. S. Kim, and T. J. Lee. Synthesis of meso- and macro- porous aluminosilicate over micro-channel plate as support material for production of hydrogen by water-gas shift (WGS). *International Journal of Precision Engineering and Manufacturing*, 16:1239–1244, 2015.
- [124] H. K. Kammler, L. Mädler, and S. E. Pratsinis. Flame synthesis of nanoparticles. *Chemical Engineering & Technology*, 24(6):583–596, 2001.
- [125] B. Thiébaud. Final analysis: Flame spray pyrolysis: A unique facility for the production of nanopowders. *Platinum Metals Review*, 55:149–151, 2011.
- [126] J. R. Jensen, T. Johannessen, S. Wedel, and H. Livbjerg. A study of Cu/ZnO/Al₂O₃ methanol catalysts prepared by flame combustion synthesis. *Journal of Catalysis*, 218(1):67–77, 2003.
- [127] F. Huber, H. Meland, M. Ronning, H. Venvik, and A. Holmen. Comparison of Cu-Ce-Zr and Cu-Zn-Al mixed oxide catalysts for water-gas shift. *Topics in Catalysis*, 45(1-4):101–104, 2007.
- [128] R. Ahmad, M. Hellinger, M. Buchholz, H. Sezen, L. Gharnati, C. Wöll, J. Sauer, M. Döring, J. Grunwaldt, and U. Arnold. Flame-made Cu/ZnO/Al₂O₃ catalyst for dimethyl ether production. *Catalysis Communication*, 43:52–56, 2014.
- [129] R. Kam, C. Selomulya, R. Amal, and J. Scott. The influence of La-doping on the activity and stability of Cu/ZnO catalyst for the low-temperature water-gas shift reaction. *Journal of Catalysis*, 273(1):73–81, 2010.
- [130] Z. Y. Fei, P. Lu, X. Z. Feng, B. Sun, and W. J. Ji. Geometrical effect of CuO nanostructures on catalytic benzene combustion. *Catalysis Science & Technology*, 2(8):1705–1710, 2012.

- [131] M. Behrens, S. Zander, P. Kurr, N. Jacobsen, J. Senker, G. Koch, T. Ressler, R. W. Fischer, and R. Schlögl. Performance improvement of nanocatalysts by promoter-induced defects in the support material: methanol synthesis over Cu/ZnO:Al. *Journal of the American Chemical Society*, 135(16):6061–6068, 2013.
- [132] W. P. Dow, Y. P. Wang, and T. J. Huang. TPR and XRD studies of yttria-doped ceria/ γ -alumina-supported copper oxide catalyst. *Applied Catalysis A: General*, 190(1-2):25–34, 2000.
- [133] I. Kasatkin, P. Kurr, B. Kniep, and R. Trunschke, A. Schlögl. Role of lattice strain and defects in copper particles on the activity of Cu/ZnO/Al₂O₃ catalysts for methanol synthesis. *Angewandte Chemie*, 119:7465–7468, 2007.
- [134] M. Stiefel, R. Ahmad, U. Arnold, and M. Doring. Direct synthesis of dimethyl ether from carbon-monoxide-rich synthesis gas: Influence of dehydration catalysts and operating conditions. *Fuel Processing Technology*, 92(8):1466–1474, 2011.
- [135] S. Jiang, J. S. Hwang, T. H. Jin, T. X. Cai, W. Cho, Y. S. Baek, and S. E. Park. Dehydration of methanol to dimethyl ether over ZSM-5 zeolite. *Bulletin of the Korean Chemical Society*, 25(2):185–189, 2004.
- [136] S. Zander, E. L. Kunkes, M. E. Schuster, J. Schumann, G. Weinberg, D. Teschner, N. Jacobsen, R. Schlogl, and M. Behrens. The role of the oxide component in the development of copper composite catalysts for methanol synthesis. *Angewandte Chemie-International Edition*, 52(25):6536–6540, 2013.
- [137] J. Korvink, P. Smith, D. Shin, O. Brand, G Fedder, C. Hierold, and O. Tabata. Inkjet-based micromanufacturing. In *Advanced micro and nanosystems*. Wiley, Weinheim, 2012.
- [138] A. D. Taylor, E. Y. Kim, V. P. Humes, J. Kizuka, and L. T. Thompson. Inkjet printing of carbon supported platinum 3-D catalyst layers for use in fuel cells. *Journal of Power Sources*, 171(1):101–106, 2007.
- [139] S. H. Eom, S. Senthilarasu, P. Uthirakumar, S. C. Yoon, J. Lim, C. Lee, H. S. Lim, J. Lee, and S. H. Lee. Polymer solar cells based on

- inkjet-printed PEDOT: PSS layer. *Organic Electronics*, 10(3):536–542, 2009.
- [140] L. Jacot-Descombes, M. R. Gullo, V. J. Cadarso, and J. Brugger. Fabrication of epoxy spherical microstructures by controlled drop-on-demand inkjet printing. *Journal of Micromechanics and Microengineering*, 22(7), 2012.
- [141] C. C. Ho, K. Murata, D. A. Steingart, J. W. Evans, and P. K. Wright. A super ink jet printed zinc-silver 3D microbattery. *Journal of Micromechanics and Microengineering*, 19(9), 2009.
- [142] M. Lejeune, T. Chartier, C. Dossou-Yovo, and R. Noguera. Ink-jet printing of ceramic micro-pillar arrays. *Journal of the European Ceramic Society*, 29(5):905–911, 2009.
- [143] K. Woo, D. Kim, J. S. Kim, S. Lim, and J. Moon. Ink-jet printing of Cu-Ag-based highly conductive tracks on a transparent substrate. *Langmuir*, 25(1):429–433, 2009.
- [144] E. Tekin, P. J. Smith, and U. S. Schubert. Inkjet printing as a deposition and patterning tool for polymers and inorganic particles. *Soft Matter*, 4(4):703–713, 2008.
- [145] T. Xu, J. Jin, C. Gregory, J. J. Hickman, and T. Boland. Inkjet printing of viable mammalian cells. *Biomaterials*, 26(1):93–99, 2005.
- [146] B. Derby and N. Reis. Inkjet printing of highly loaded particulate suspensions. *Mrs Bulletin*, 28(11):815–818, 2003.
- [147] B. J. de Gans, P. C. Duineveld, and U. S. Schubert. Inkjet printing of polymers: State of the art and future developments. *Advanced Materials*, 16(3):203–213, 2004.
- [148] B. Derby. Inkjet printing of functional and structural materials: Fluid property requirements, feature stability, and resolution. *Annual Review of Materials Research*, Vol 40, 40:395–414, 2010.
- [149] B. Derby. Inkjet printing ceramics: From drops to solid. *Journal of the European Ceramic Society*, 31(14):2543–2550, 2011.

- [150] D. Jang, D. Kim, and J. Moon. Influence of fluid physical properties on ink-jet printability. *Langmuir*, 25(5):2629–2635, 2009.
- [151] D. Kuscer, G. Stavber, G. Trefalt, and M. Kosec. Formulation of an aqueous titania suspension and its patterning with ink-jet printing technology. *Journal of the American Ceramic Society*, 95(2):487–493, 2012.
- [152] J. Perelaer, P. J. Smith, M. M. P. Wijnen, E. van den Bosch, R. Eckardt, P. H. J. M. Ketelaars, and U. S. Schubert. Droplet tailoring using evaporative inkjet printing. *Macromolecular Chemistry and Physics*, 210(5):387–393, 2009.
- [153] N. Reis, C. Ainsley, and B. Derby. Viscosity and acoustic behavior of ceramic suspensions optimized for phase-change ink-jet printing. *Journal of the American Ceramic Society*, 88(4):802–808, 2005.
- [154] D. B. Bogy and F. E. Talke. Experimental and theoretical study of wave propagation phenomena in drop-on-demand ink jet devices. *IBM Journal of Research and Development*, 28(3):314–321, 1984.
- [155] H. J. Lin, H. C. Wu, T. R. Shan, and W. S. Hwang. The effects of operating parameters on micro-droplet formation in a piezoelectric inkjet printhead using a double pulse voltage pattern. *Materials Transactions*, 47(2):375–382, 2006.
- [156] P. Calvert. Inkjet printing for materials and devices. *Chemistry of Materials*, 13(10):3299–3305, 2001.
- [157] E. R. Lee. *Microdrop generation*. Nano- and Microscience, Engineering, Technology and Medicine. CRC Press, London, 2002.
- [158] Y. Oh, J. Kim, Y. J. Yoon, H. Kim, H. G. Yoon, S.-N. Lee, and J. Kim. Inkjet printing of Al₂O₃ dots, lines, and films: From uniform dots to uniform films. *Current Applied Physics*, 11(3):S359–S363, 2011.
- [159] N. Marjanovic, J. Hammerschmidt, J. Perelaer, S. Farnsworth, I. Rawson, M. Kus, E. Yenel, S. Tilki, U. S. Schubert, and R. R. Baumann. Inkjet printing and low temperature sintering of CuO and CdS as functional electronic layers and Schottky diodes. *Journal of Materials Chemistry*, 21(35):13634–13639, 2011.

- [160] C. C. Tseng, C. P. Chang, Y. Sung, Y. C. Chen, and M. D. Ger. A novel method to produce Pd nanoparticle ink for ink-jet printing technology. *Colloids and Surfaces a-Physicochemical and Engineering Aspects*, 339(1-3):206–210, 2009.
- [161] M. Arin, P. Lommens, N. Avci, S. C. Hopkins, K. De Buysser, I. M. Arabatzis, I. Fasaki, D. Poelman, and I. Van Driessche. Inkjet printing of photocatalytically active TiO₂ thin films from water based precursor solutions. *Journal of the European Ceramic Society*, 31(6):1067–1074, 2011.
- [162] R. Gallage, A. Matsuo, T. Fujiwara, T. Watanabe, N. Matsushita, and M. Yoshimura. Direct patterning of dense cerium oxide thin film by developed ink-jet deposition method at moderate temperatures. *Thin Solid Films*, 517(16):4515–4519, 2009.
- [163] B. Fousseret, M. Mougenot, F. Rossignol, J. F. Baumard, B. Soulestin, C. Boissiere, F. Ribot, D. Jalabert, C. Carrion, C. Sanchez, and M. Lejeune. Inkjet-printing-engineered functional microdot arrays made of mesoporous hybrid organosilicas. *Chemistry of Materials*, 22(13):3875–3883, 2010.
- [164] T. M. Liou, C. Y. Chan, and K. C. Shih. Study of the characteristics of polymer droplet deposition in fabricated rectangular microcavities. *Journal of Micromechanics and Microengineering*, 19(6), 2009.
- [165] C. T. Chen, C. L. Chiu, C. Y. Hsu, Z. F. Tseng, and C. T. Chuang. Inkjet-printed polymeric microstructures in n-sided regular polygonal cavities. *Journal of Microelectromechanical Systems*, 20(4):1001–1009, 2011.
- [166] U. Loffelmann, J. G. Korvink, C. E. Hendriks, U. S. Schubert, and P. J. Smith. Ink jet printed silver lines formed in microchannels exhibit lower resistance than their unstructured counterparts. *Journal of Imaging Science and Technology*, 55(4), 2011.
- [167] K. J. Wallenstein and W. B. Russel. The theory of delamination during drying of confined colloidal suspensions. *Journal of Physics-Condensed Matter*, 23(19), 2011.

- [168] K. Y. Shin, S. H. Lee, and J. H. Oh. Solvent and substrate effects on inkjet-printed dots and lines of silver nanoparticle colloids. *Journal of Micromechanics and Microengineering*, 21(4), 2011.
- [169] A. Lee, K. Sudau, K. H. Ahn, S. J. Lee, and N. Willenbacher. Optimization of experimental parameters to suppress nozzle clogging in inkjet printing. *Industrial & Engineering Chemistry Research*, 51(40):13195–13204, 2012.
- [170] S. D. Hoath, I. M. Hutchings, G. D. Martin, T. R. Tuladhar, M. R. Mackley, and D. Vadillo. Links between ink rheology, drop-on-demand jet formation, and printability. *Journal of Imaging Science and Technology*, 53(4), 2009.
- [171] S. Güttler and A. Gier. *The chemistry of inkjet inks*. World Scientific Publishing, Singapore, 2010.
- [172] J. De Jong, H. Reinten, H. Wijshoff, M. van den Berg, K. Delescen, R. van Dongen, F. Mugele, M. Versluis, and D. Lohse. Marangoni flow on an inkjet nozzle plate. *Applied Physics Letters*, 91(20), 2007.
- [173] K. S. Kwon. Experimental analysis of waveform effects on satellite and ligament behavior via in situ measurement of the drop-on-demand drop formation curve and the instantaneous jetting speed curve. *Journal of Micromechanics and Microengineering*, 20(11), 2010.
- [174] B. W. Jo, A. Lee, K. H. Ahn, and S. J. Lee. Evaluation of jet performance in drop-on-demand (DOD) inkjet printing. *Korean Journal of Chemical Engineering*, 26(2):339–348, 2009.
- [175] S. D. Hoath, W. K. Hsiao, S. Jung, G. D. Martin, I. Hutchings, N. F. Morrison, and O. G. Harlen. Drop speeds from drop-on-demand ink-jet print heads. *Journal of Imaging Science and Technology*, 57:10503–1 – 10503–11, 2013.
- [176] J. H. Kim, Y. J. Yoon, J. H. Kim, H. T. Kim, and E. H. Koo. Ceramic ink for manufacturing ceramic thick film by inkjet printing, 2011.
- [177] L. Cui, J. Zhang, X. Zhang, L. Huang, Z. Wang, Y. Li, H. Gao, S. Zhu, T. Wang, and B. Yang. Suppression of the coffee ring effect by

- hydrosoluble polymer additives. *ACS Applied Materials & Interfaces*, 4:2775–2780, 2012.
- [178] T. Böltken. *Microstructured reactors with integrated metallic membranes for on-site production of pure hydrogen*. Thesis, Karlsruhe Institute of Technology, 2015.
- [179] J. Leng. Drying of a colloidal suspension in confined geometry. *Physical Review E*, 82(2), 2010.
- [180] I. I. M. Tjburg, H. De Bruin, P. A. Elberse, and J. W. Geus. Sintering of pseudo-boehmite and γ -Al₂O₃. *Journal of Material Science*, 26:5945–5949, 1991.
- [181] O. Görke, P. Pfeifer, and K. Schubert. Kinetic study of ethanol reforming in a microreactor. *Applied Catalysis A: General*, 360(2):232–241, 2009.
- [182] J. G. Jakobsen, M. Jakobse, I. Chorkendorff, and J. Sehested. Methane steam reforming kinetics for a rhodium-based catalyst. *Catalysis Letteres*, 140:90–97, 2010.
- [183] J. H. Tong and Y. Matsumura. Effect of catalytic activity on methane steam reforming in hydrogen-permeable membrane reactor. *Applied Catalysis A: General*, 286(2):226–231, 2005.
- [184] R. Dittmeyer and G. Emig. Simultaneous heat and mass transfer and chemical reaction. In G. Ertl, H. Knözinger, F. Schüth, and J. Weitkamp, editors, *Handbook of heterogeneous catalysis*, pages 1727–1784. Wiley-VCH Verlag GmbH & Co. KGaA., 2008.
- [185] K. D. Kim and H. T. Kim. Formation of silica nanoparticles by hydrolysis of TEOS using a mixed semi-batch/batch method. *Journal of Sol-Gel Science and Technology*, 25:183–189, 2002.
- [186] S. Gangly and S. Chakraborty. Sedimentation of nanoparticles in nanoscale colloidal suspensions. *Physics Letter A*, 375:2394–2399, 2011.
- [187] A. Qiang, L. Zhao, C. Xu, and M. Zhou. Effect of dispersant on the colloidal stability of nano-sized CuO suspension. *Journal of Dispersion Science and Technology*, 28:1004–1007, 2007.

- [188] J. B. Lindén, M. Larsson, B. R. Coad, W. M. Skinner, and M. Nydén. Methane steam reforming kinetics for a rhodium-based catalyst. *RSC Advances*, 4:25063–25066, 2014.
- [189] L. Huang, G. J. Kramer, W. Wieldraaijer, D. S. Brands, E. K. Poels, H. L. Castricum, and H. Bakker. Methanol synthesis over Cu/ZnO catalysts prepared by ball milling. *Catalysis Letters*, 48:55–59, 1997.
- [190] T. Rojac and M. Kosec. Mechanochemical synthesis of complex ceramic oxides. In Malgorzata Sopicka-Lizer, editor, *High-energy ball milling: Mechanochemical processing of nanopowders*, book section 6, pages 113–148. Elsevier, 2010.
- [191] J. C. Slaa, G. J. M. Weierink, J. G. Vanommen, and J. R. H. Ross. TPR and infrared measurements with Cu/ZnO/Al₂O₃ based catalysts for the synthesis of methanol and higher alcohols from CO + H₂. *Catalysis Today*, 12(4):481–490, 1992.
- [192] S. Gopalakrishnan, S. Yada, J. Muench, T. Selvam, W. Schwieger, M. Sommer, and W. Peukert. Wet milling of H-ZSM-5 zeolite and its effects on direct oxidation of benzene to phenol. *Applied Catalysis A: General*, 327:132–138, 2007.
- [193] J. H. Xie and S. Kaliaguine. Zeolite ball milling as a means of enhancing the selectivity for base catalyzed reactions. *Applied Catalysis A: General*, 148(2):415–423, 1997.
- [194] A. S. Kharitonov, V. B. Fenelonov, T. P. Voskresenskaya, N. A. Rudina, V. V. Molchanov, L. M. Plyasova, and G. I. Panov. Mechanism of FeZSM-5 milling and its effect on the catalytic performance in benzene to phenol oxidation. *Zeolites*, 15(3):253–258, 1995.
- [195] C. D. Chang. Hydrocarbons from methanol. *Catalysis Reviews-Science and Engineering*, 25(1):1–118, 1983.
- [196] D. Soltman and V. Subramanian. Inkjet-printed line morphologies and temperature control of the coffee ring effect. *Langmuir*, 24(5):2224–2231, 2008.

- [197] F. Girard and M. Antoni. Influence of substrate heating on the evaporation dynamics of pinned water droplets. *Langmuir*, 24(20):11342–11345, 2008.
- [198] R. D. Deegan, O. Bakajin, T. F. Dupont, G. Huber, S. R. Nagel, and T. A. Witten. Capillary flow as the cause of ring stains from dried liquid drops. *Nature*, 389(6653):827–829, 1997.
- [199] S. Kvisle, T. Fuglerud, S. Kolboe, U. Olsbye, K. P. Lillerud, and B. V. Vora. Methanol-to-hydrocarbons. In G. Ertl, H. Knözinger, F. Schüth, and J. Weitkamp, editors, *Handbook of heterogeneous catalysis*, pages 2950–2965. Wiley-VCH Verlag GmbH & Co. KGaA., 2008.
- [200] K. Pansanga, N. Lohitharn, A. C. Y. Chien, E. Lotero, J. Panpranot, P. Praserthdam, and J. G. Goodwin Jr. Copper-modified alumina as a support for iron Fischer-Tropsch synthesis catalysts. *Applied Catalysis A: General*, 332:130–137, 2007.
- [201] J. Steiner, K. Bay, V. Werner, J. Amann, S. Bunzel, C. Moßbacher, J. Müller, E. Schwab, and M. Weber. Iron- and copper-comprising heterogeneous catalyst and process for preparing olefins by reacting carbon monoxide with hydrogen, US 8614164 B2, 2013.
- [202] X. Ma, Q. Ge, J. Ma, and H. Xu. Synthesis of LPG via DME from syngas in two-stage reaction system. *Fuel Processing Technology*, 109:1–6, 2013.
- [203] C. Li and K. Fujimoto. Synthesis gas conversion to isobutane-rich hydrocarbons over hybrid catalyst containing Beta zeolite - role of doped palladium and influence of $\text{SiO}_2/\text{Al}_2\text{O}_3$ ratio. *Catalysis Science & Technology*, 5:4501–4510, 2015.
- [204] Q. Zhang, X. Li, K. Asami, S. Asaoka, and K. Fujimoto. Synthesis of LPG synthesis gas. *Fuel Processing Technology*, 85:1139–1150, 2004.
- [205] K. Fujimoto, H. Saima, and H. Tominaga. Selective synthesis of LPG from synthesis gas. *Bulletin of the Chemical Society of Japan*, 58:3059–3060, 1985.

List of acronyms

| | |
|----------------|--|
| ATR | Autothermal reforming |
| BET | Brunauer-Emmet-Teller |
| BJH | Barret-Joyner-Halenda |
| CRT | Institute of Chemical Reaction Engineering |
| CVD | Chemical vapor deposition |
| CZA | Cu/ZnO/Al ₂ O ₃ |
| DME | Dimethylether |
| DMF | Dimethylformamide |
| DOD | Drop-on-demand |
| EDX | Energy dispersive X-ray analysis |
| EISA | Evaporation-induced self-assembly |
| EPD | Electrophoretic deposition |
| EPMA | Field emission electron probe microanalyzer |
| FAU | Friedrich-Alexander Universität Erlangen-Nürnberg |
| FID | Flame ionization detector |
| FSP | Flame spray pyrolysis |
| FSP-CZA | Cu/ZnO/Al ₂ O ₃ synthesized by flame spray pyrolysis |
| GC | Gas chromatography |
| GCR | Gas-cooled reactor |
| GHSV | GAs hourly space velocity |
| HDMSO | Hexamethyldisiloxane |
| IMVT | Institute for Micro Process Engineering |
| IKFT | Institute of Catalysis Research and Technology |
| KIT | Karlsruhe Institute of Technology |
| KOGAS | Korea Gas Corporation |
| LFC | Liquid mass flow controller |
| LPG | Liquefied petroleum gas |
| MFC | Mass flow controller |
| MPG | Multi purpose gasification |

| | |
|--------------|--|
| MTBE | Methyl tert-butyl ether |
| MTO | Methanol-to-olefin |
| PM10 | Particulate matter up to 10 μm size |
| POX | Partial oxidation of methane |
| PSA | Pressure swing adsorption |
| SEM | Scanning electron microscope |
| SMR | Steam methane reforming |
| TCD | Thermal conductivity detector |
| TEM | Transmission electron microscope |
| TEOS | Tetraethyl orthosilicate |
| TPAOH | Tetrapropylammonium hydroxide |
| TPD | Temperature programmed desorption |
| TPR | Temperature programmed reduction |
| WCR | Water-cooled reactor |
| WDS | Wavelength dispersive spectroscopy |
| XRD | X-ray diffraction |
| YSZ | Yttria-stabilized zirconia |

List of symbols

| | |
|------------|---|
| α | nozzle diameter (m) |
| γ | surface tension (N/m) |
| ν_i | number of carbon atoms of component i (-) |
| η | dynamic viscosity (mPas) |
| ρ | density (kg/m ³) |
| c_i | volume concentration (%) |
| D | diffusion coefficient (m ² /s) |
| ΔH | reaction enthalpy (J/mol) |
| L | radius of ink droplet (m) |
| \dot{N} | molar flow (mol/s) |
| P | productivity (mg/g _{cat} min) |
| p | pressure (bar) |
| S | selectivity (%) |
| T | temperature (°C) |
| \dot{V} | volume flow (m ³ /s) |
| X | conversion (%) |
| y_i | molar fraction (-) |

List of subscripts

| | |
|------|---------------|
| cat | Catalyst |
| i | Component |
| MeOH | Methanol |
| 0 | Initial state |
| prod | Product |

Appendix

A. Appendix

A.1. Methane steam reforming experiments

SMR was carried out with constant inlet concentrations of 10 vol. % CH₄, 40 vol. % H₂O, and 50 vol. % N₂, which corresponds to a steam-to-carbon ratio of 4. The catalyst was reduced prior to the experiments at 750 °C in 50 vol. % H₂/N₂ for 2 hours. The test rig contained a dosing system for the gases and a micromixer for dosage of water. The pressure drop of the microreactor was negligible, and the reactor was considered isothermal based on prior experience [181]. The W/F ratio was calculated by the total mass of catalyst divided by the mole flow of methane at STP conditions.

A.2. Inkjet printing of a ZSM-5 precursor ink.

A ZSM-5 synthesis mixture was prepared at CRT. The molar ratio of the components was 1.00 SiO₂: 40 H₂O: 0.30 TPAOH: 0.01 Al₂O₃: 4 EtOH. In order to remove large particles to prevent the possible clogging of the printhead nozzle, the mixture was centrifugated for 5 minutes at 2000 rpm and the supernatant was used for ink formulation. A final ink was prepared by mixing the supernatant with ethylene glycol (50:50 wt. ratio). The printing was performed on the rectangular stainless steel microchannels (MF-1). After the printing it was dried overnight at room temperature, and the steam assisted crystallization was carried out following calcination at 550 °C.

A.3. Supplementary figures and tables

Table A.1.: Details of the Micro Berty Reactor [117].

| | |
|-----------------------|--|
| Reactants | Gas, Vapor |
| Basket screen | 50 x 50 mesh, 0.23 mm wire and a nominal opening size of 0.28 mm |
| Inside diameter | 25.4 mm |
| Basket volume | 3.6 cm ³ |
| Max. working pressure | 345 bar |
| Max. blower speed | 5000 rpm |
| Max. temperature | 343 °C |
| Material | HASRELLOY [®] |

Table A.2.: GC analysis program. Oven temperature change and valve operation.

| Time (min) | Temperature (°C) | Valve 1 position | Temperature ramp (°C/min) | Performance |
|------------|------------------|------------------|---------------------------|---------------------------------|
| 0 | 60 | off | 0 | start analysis |
| 3 | 60 | on | 20 | oven heating valve operation |
| 10 | 200 | on | 0 | keeping temperature |
| 16 | 200 | on | -100 | oven cooling |
| 17.4 | 60 | on | 0 | keeping temperature |
| 18 | 60 | off | 0 | valve operation |
| 23 | 60 | off | 0 | end analysis |

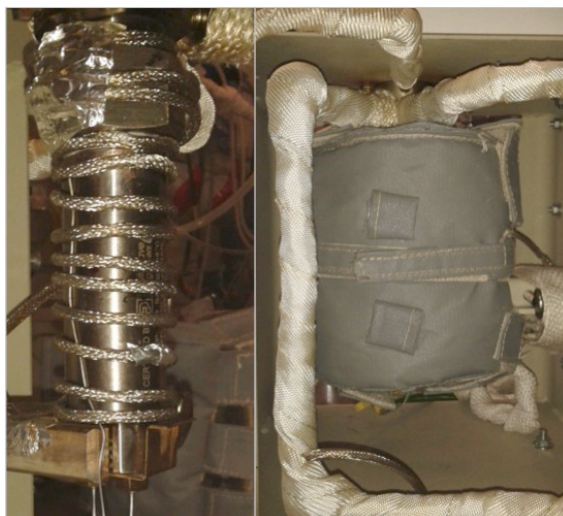


Figure A.1.: The Micro Bertly Reactor with heating band (left) and insulation jacket (right).

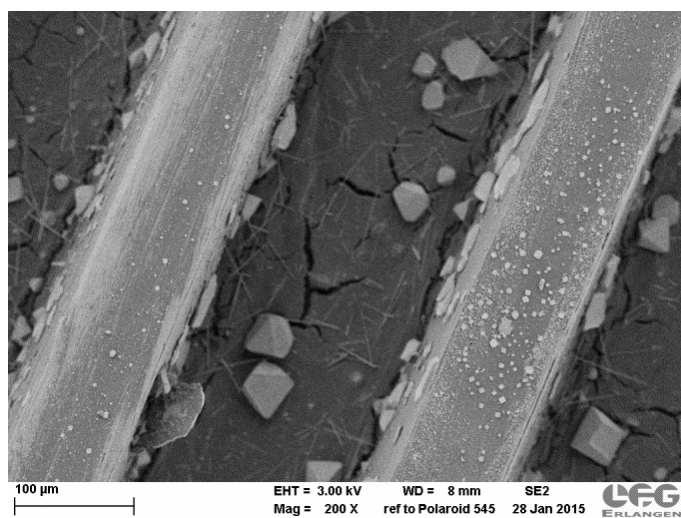


Figure A.2.: A SEM image of microchannels with CZA coating and ZSM-5 precursor printing above it.

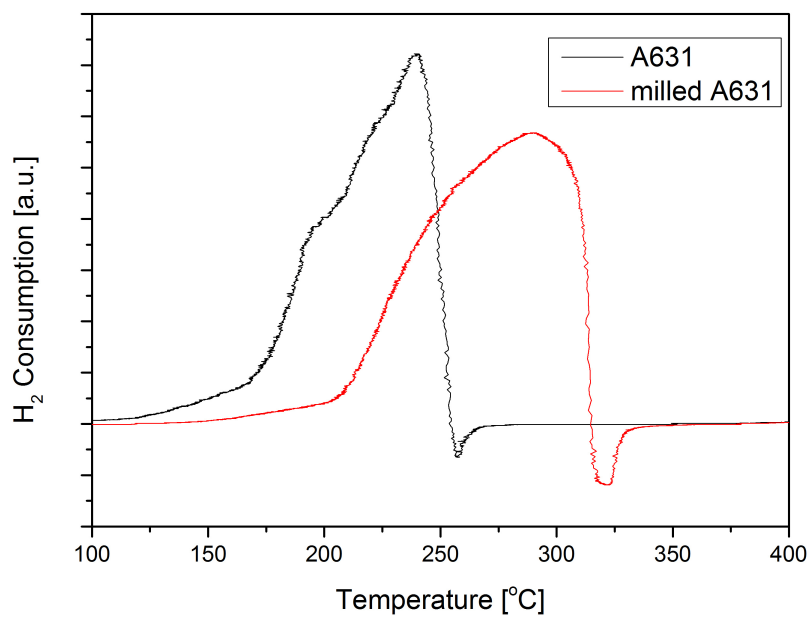


Figure A.3.: TPR spectrum of CZA (black) and 10 minutes ball-milled CZA (red).

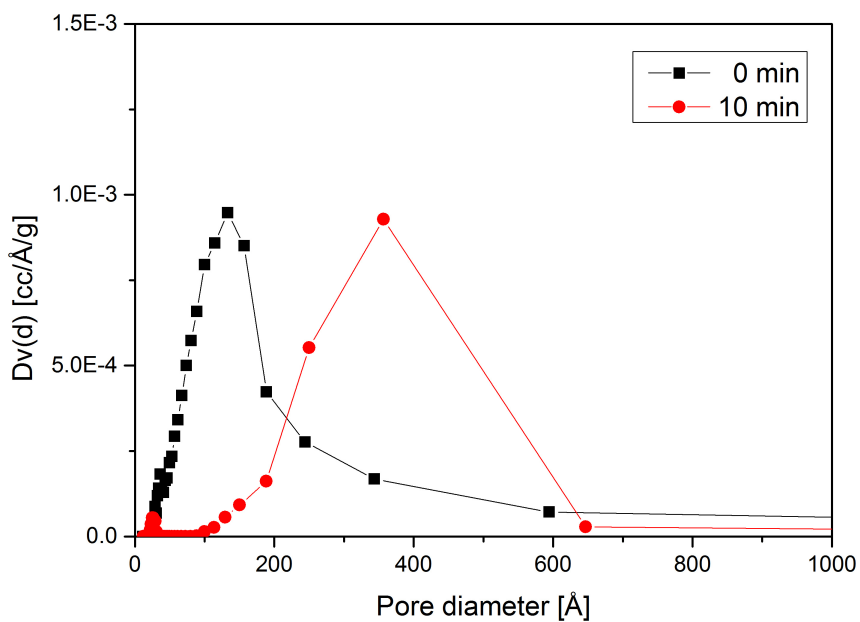


Figure A.4.: Pore size distribution of CZA (black) and 10 minutes ball-milled CZA (red).

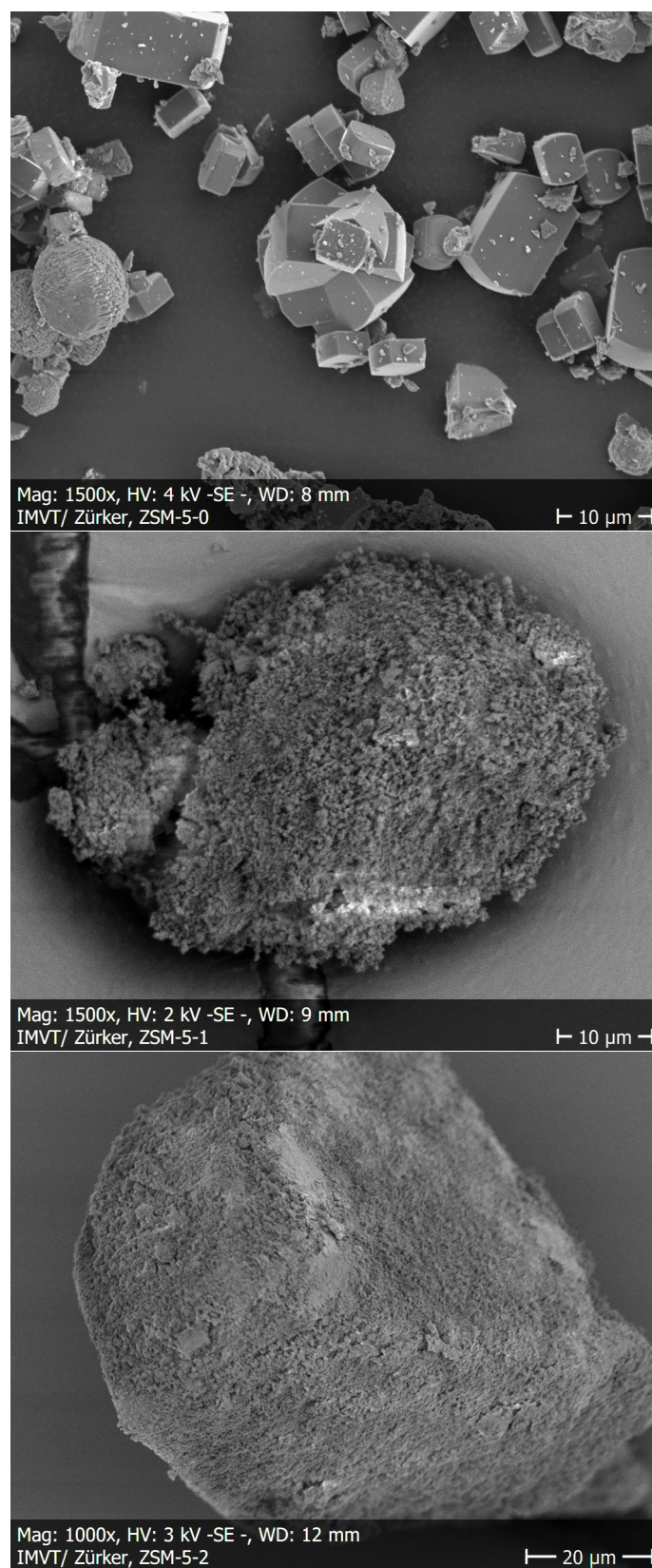


Figure A.5.: SEM images of ZSM-5 catalyst. (a) fresh ZSM-5 (b) 1hour ball-milled ZSM-5 (c) 2 hours ball-milled ZSM-5.

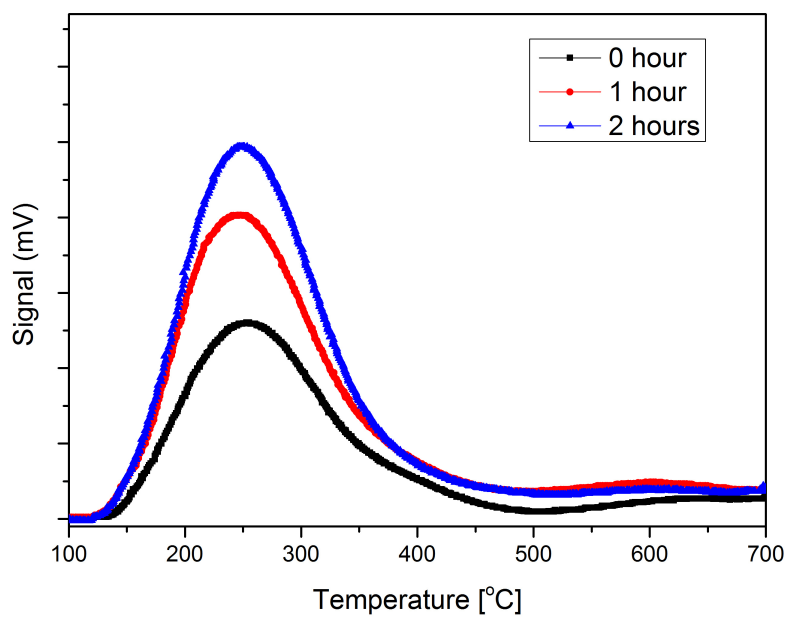


Figure A.6.: Change of the NH₃-TPD spectrum of ZSM-5 by ball-milling.

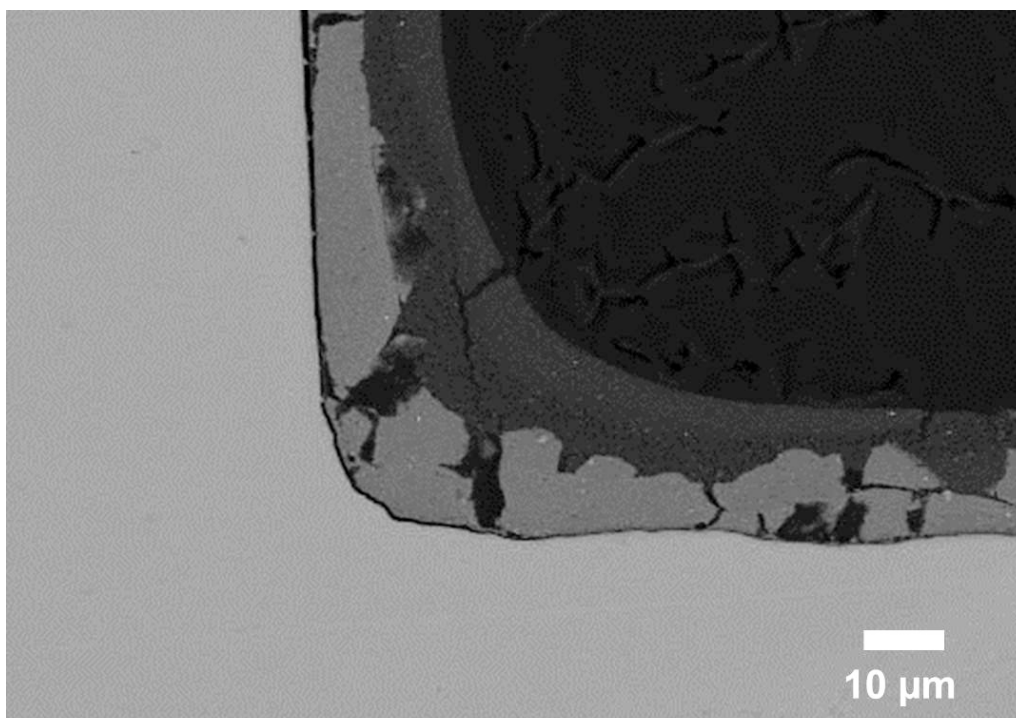


Figure A.7.: Cross-sectional image of microchannel corner of DL3.

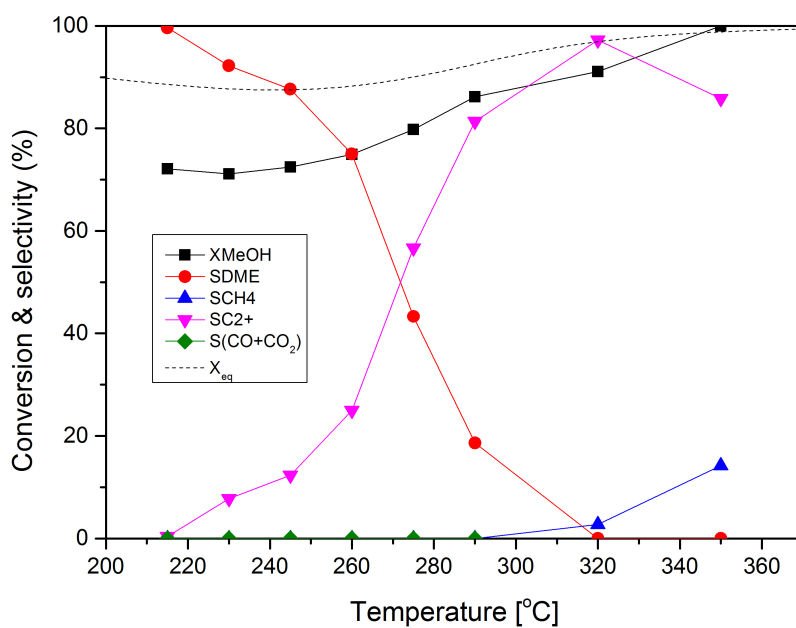


Figure A.8.: Conversion and selectivity of methanol dehydration over H-ZSM-5 layer in the microchannel reactor as a function of reaction temperature. $p = 40$ bar; $N_2:MeOH:H_2:CO:CO_2 = 50:0.3:5:5:2$. The equilibrium conversion values (X_{eq}) were calculated with the HSC[®] Software.

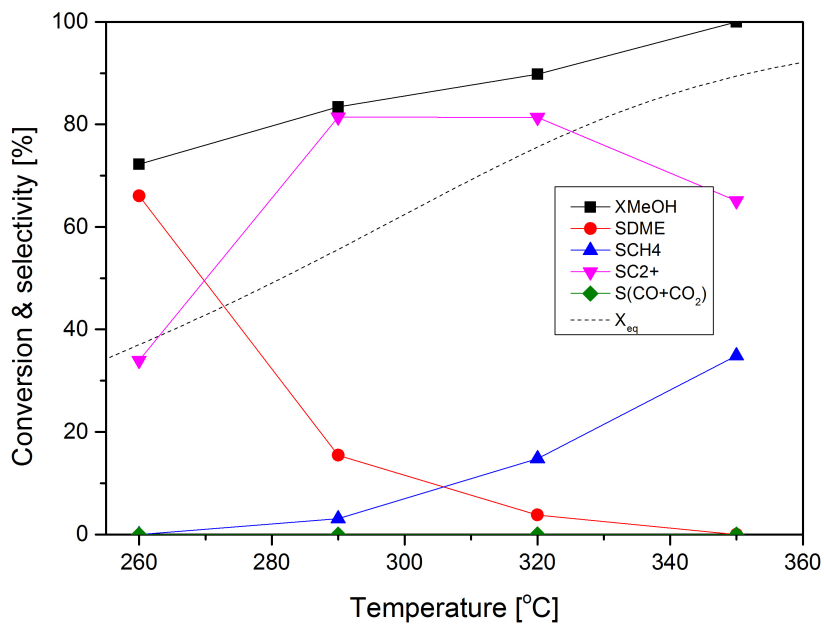


Figure A.9.: Conversion and selectivity of methanol dehydration over H-ZSM-5 layer in the microchannel reactor as a function of reaction temperature. $p = 40$ bar; $N_2:MeOH:H_2:CO:CO_2 = 50:0.3:20:5:2$. The equilibrium conversion values (X_{eq}) were calculated with the HSC[®] Software.